Department of Civil and Environmental Engineering
University of Strathclyde

INVESTIGATION OF SUB-CORE SCALE FLUID FLOW BEHAVIOUR WITHIN HETEROGENEOUS SANDSTONES: THE ROLE OF DEFORMATION BANDS

A Thesis presented for the Degree of Doctor of Philosophy
by

CARLA ROMANO

December 2019

This thesis is the result of the author's original research. It has been composed by the author and has not been previously submitted for examination which has led to the award of a degree.

Signed:

Date:

Acknowledgements

I would like to thank my supervisors, Prof. Rebecca Lunn and Prof. Zoe Shipton, for their support, mentorship and encouragement throughout this PhD.

My sincere gratitude goes to Dr James Minto, for the precious and meaningful advices.

I would also like to thank the research group of Benson Lab, Stanford University. You all have provided a valuable help for carrying out my experiments.

I would like to thank the rest of my thesis committee for offering their time for reviewing this work.

Thank you to my friends, Anna T., Rita, Valerio and Andrea and all the lovely people I met here; you all made my life away from home easier. Thank you to my family, who always stand by my side, no matter where I am. Thank you Chris, for your love, encouragement and the good science time.

Abstract

Small-scale heterogeneities influence fluid flow at sub-core and reservoir scale. However, the influence of deformation bands, commonly found in high porosity sandstones, is poorly understood.

Internal structure of small-scale heterogeneities is investigated with X-ray computed tomography (CT). To this aim, high-resolution, artefacts-free CT images are needed. Beam hardening artefact, in cylindrical-shaped samples, increases the X-ray attenuation values with increasing distance from the centre. A new beam hardening correction technique was developed using a post-processing linearization procedure on the beam hardening curve. The technique is implemented in an automated open-source ImageJ plug-in, and successfully applied on X-ray CT images of homogeneous and heterogeneous samples containing deformation bands.

Petrophysical and multiphase properties of heterogeneous sandstones were investigated by performing core flooding experiments with positron emission tomography (PET) and/or X-ray CT imaging. Experiments were conducted on a Navajo sandstone core characterized by diagonal deformation bands and fine-grained laminae. PET images were used to derive the single phase hydrodynamic properties of the core. A drainage experiment (CO_2/water) was conducted in the water-saturated core and imaged with a medical X-ray CT scanner. Experimental results and numerical simulations indicate that deformation bands form stronger capillary barriers than laminae.

A drainage core flooding experiment (N_2/water) was performed on a Navajo sandstone core containing conjugate deformation band clusters. Results show a high N_2 saturation in the host rock compartments upstream of a thick cluster of deformation bands, identified as an extreme capillary barrier. At the end of the experiment, host rock compartments show variable N_2 saturation. Simulation models demonstrate that the capillary end effect and discontinuities in bands impact fluid saturation.

Clusters and individual cataclastic bands strongly affect fluid flow, minimizing crossflow between compartments and promoting fluid compartmentalization. Detailed

characterization of deformation bands is necessary for accurate reservoir prediction, both for carbon storage and for enhanced oil recovery.

Contents

Chapter 1

INTRODUCTION

1.1. Rationale

Spatial variation of petrophysical and multiphase flow properties influence fluid flow behaviour at small and reservoir scale (Corey & Rathjens, 1956; Krevor, et al., 2011; Krevor, et al., 2015; Li & Benson, 2015; Lunn, et al., 2008; Perrin & Benson, 2010; Pini, et al., 2012; Saadatpoor, et al., 2010; Shipton, et al., 2002). Whilst small scale heterogeneities, such as fractures, bedding planes and laminae have been extensively studied at sub-core scale, the role of deformation bands on fluid flow is still unclear. Cataclastic bands are mm thick strain localization features, characterized by low porosity and permeability and high capillary pressure compared to the surrounding rock (Aydin, 1978; Aydin & Johnson , 1978; Deng, et al., 2015; Shipton, et al., 2002). Individual deformation bands are only able to accommodate small (less than few cm) displacement; as strain increases, clusters of deformation bands may coalesce, with further reduction of porosity and permeability (Aydin & Johnson , 1978; Shipton & Cowie, 2003). Deformation bands develop in highly porous sandstones particularly in proximity to both sub-seismically visible and large displacement faults (Shipton & Cowie, 2001; Fossen, et al., 2018).

Sandstones represent the highest-quality and highest storage volume reservoirs (Benson & Cook, 2005; Bjørlykke & Jahren, 2010). Accurate site characterization and understanding the impact of geological features on fluid flow is essential for estimating storage capacity and assess injection strategies of many subsurface engineering technologies, such as carbon dioxide storage, hydrogen storage and enhanced oil recovery.

Several studies have highlighted that deformation bands have the potential to negatively affect fluid flow, leading to decreasing reservoir permeability, high degree of fluid tortuosity and fluid bypass (Ogilvie, et al., 2001; Qu & Tveranger, 2016;

Rotevatn & Fossen, 2011; Rotevatn, et al., 2017; Schultz & Siddharthan, 2005; Shipton, et al., 2002; Shipton, et al., 2005; Wilkins, et al., 2019). However, discussion is still ongoing whether deformation bands are responsible or not for reservoir compartmentalization.

Until now, fluid behaviour due to the presence of deformation bands has been mostly investigated through field observations and reservoir modelling. *In situ* and sub-core visualization and quantification of single and multiphase fluid flow in sandstones with individual and clusters deformation bands have never been performed.

1.2. Scope of the thesis

The aim of this PhD is to better understand the role of individual deformation bands and clusters of bands on fluid flow at the sub-core scale. The studies in this dissertation are aimed not only to derive petrophysical and multiphase properties of deformation bands, but also to understand how geometry, thickness, and orientation of bands influence fluid flow.

Detailed characterization of deformation band structure is performed by acquiring X-ray micro computed tomography images. With this imaging technique high-resolution images are obtained without compromising the integrity of the samples. However, image quality and the resulting estimation of petrophysical properties depend on removal of image artefacts produced during the reconstruction process. From this consideration follows the first research question: how can we improve micro-CT image quality for a better visualization of small-scale heterogeneity and prediction of petrophysical properties?

Core flooding experiments are conducted on two Navajo sandstone core samples, taken from vertical boreholes drilled through a sub-seismic normal fault in Utah (Big Hole Fault) (Shipton, et al., 2002). The first sample is characterized by individual cataclastic bands diagonally oriented to the flow and two main fine-grained laminae perpendicular to the axis of the core. The deformation bands do not isolate any portion of the rock within this core sample. Combining experimental and numerical simulations results addresses the following questions: how do individual

deformation bands affect single and multiphase fluid flow? Do laminae contribute more or less than deformation bands on fluid flow?

Multiphase core flooding experiments are performed on the second sample, characterized by single conjugate clusters of deformation bands cutting laminae. The research questions addressed with this experiment are: in what way do clusters of deformation bands influence fluid flow? How significantly different are the petrophysical and multiphase properties compared to individual bands? Can deformation bands be responsible for fluid compartmentalization?

1.3. Outline of the thesis

Chapter 2 is a literature review of deformation bands, imaging techniques, core flooding experiments and the influence of small-scale heterogeneity on fluid flow.

Chapter 3 presents a novel and automatic methodology developed for correction of beam hardening artefact. Beam hardening is common artefact shown in X-ray micro computed tomography, which increases attenuation values at the edge of the images. In this Chapter the correction technique is developed and applied to several scan images of homogeneous and heterogeneous samples. The correction improves images quality and the resulting estimation of petrophysical properties such as porosity and permeability. The correction was applied to all subsequent X-ray micro-CT scans presented in this thesis.

The work includes a plug in, which automatically run in the open source software ImageJ. It has been published in *Computers and Geosciences* Journal as "Automated high accuracy, rapid beam hardening correction in X-Ray Computed Tomography of multi-mineral, heterogeneous core samples" by Carla Romano, Dr James M. Minto, Prof. Zoe K. Shipton and Prof. Rebecca J. Lunn. This study was conceived by all authors. I acquired micro-CT data, and created the code. James M. Minto acquired micro-CT data and carried out the simulation for determination of sub-core scale permeability. All authors contributed in the analysis of the results and in editing the manuscript prior to submission.

Chapter 4 focuses on the understanding of single and multiphase flow behaviour in sandstone characterized by cataclastic deformation bands. Micro-CT X-ray images were obtained to better define the geometry of the deformation bands. The Chapter includes results of single phase radiotracer experiments and multiphase core flooding experiments. Positron Emission Tomography (PET) and medical X-ray CT were used for single and multiphase experiments, respectively. Core flooding experiments were conducted in collaboration with Benson Lab research group, at Stanford University. Numerical simulations of the core were performed to support the experimental evidence.

This work has been submitted to *Water Resources Research* journal as "Sub-core scale fluid flow behavior in a sandstone with cataclastic deformation bands" by Carla R. Romano, Dr Christopher Zahasky, Dr Charlotte Garing, Dr James M. Minto, Prof. Sally M. Benson, Prof. Zoe K. Shipton and Prof. Rebecca J. Lunn. I conducted the single phase flow experiments with assistance from Christopher Zahasky. I conducted multiphase flow experiments with assistance from Charlotte Garing. Time arrival and fluid velocity maps were developed in collaboration with Christopher Zahasky. I carried out analysis of the data, image processing, and numerical simulations. All the authors provided feedback on data analysis and edited the manuscript before submission to the journal.

Chapter 5 presents multiphase fluid flow behaviour in sandstone with clusters of deformation bands. Micro-CT images were taken to better understand the complicated geometry of clusters of bands. A multiphase core flooding experiment was conducted at Stanford University while medical X-ray CT images were taken in both unsteady and steady state conditions. Simulations of a simplified case were designed for understanding the role of boundary conditions and discontinuities in bands on fluid saturation.

This study has been submitted to a peer-reviewed journal as "Extreme capillary heterogeneities and *in situ* fluid compartmentalization due to clusters of deformation bands in sandstones" by Carla R. Romano, Dr Charlotte Garing, Dr James Minto, Prof. Sally M. Benson, Prof. Zoe K. Shipton, Prof. Rebecca J. Lunn. Core flooding experiments were conducted by me, with intellectual contribution of Charlotte Garing.

I acquired micro-CT data, analysed the scan images and carried out numerical simulations. All authors contributed in providing feedbacks on analysis of data and editing manuscript before submission.

Chapter 6 highlights and discusses the main findings of the research and brings out potential future work.

Chapter 2

LITERATURE REVIEW

2.1. Rationale

In highly porous sandstone, displacement is accommodated by forming deformation bands (Aydin, 1978). Deformation bands can be classified based on their kinematic and deformation mechanism (Fossen, et al., 2007). Cataclastic deformation bands form due to grain rolling, reorganisation and fracturing; this leads to a reduced porosity and permeability compared to the host rock (Antonellini & Aydin, 1994; Aydin & Johnson , 1978; Ballas, et al., 2015; Deng, et al., 2015; Shipton, et al., 2002; Taylor & Polland, 2000). Cataclastic bands are mainly found in the damage and process zone of normal faults (Fossen, et al., 2007). The frequency of deformation bands increases towards the fault core, but no relationship has been found between the frequency of bands and the fault displacement (Schueller, et al., 2013). Therefore, clusters of bands characterize both small displacement, sub-seismic faults and large seismically resolvable structures. Several researchers, based on field observation and numerical simulations, have shown that deformation bands negatively affect fluid flow (Rotevatn & Fossen, 2011; Wilkins, et al., 2019).

Micro computed tomography is nowadays widely used for the characterization of rock features and the geometry of small-scale heterogeneities. The acquisition process can take several hours, however, the obtained scan images have an unparalleled spatial resolution of several micrometres. The quality of these images is strongly affected by previous processing of micro-CT images, aimed at removing common images artefacts, such as the beam hardening artefact.

Core flooding experiments are valuable tools for understanding fluid flow behaviour at reservoir conditions. Integration of these experiments with increasingly advanced imaging techniques allows visualization *in situ* of the effect on fluid flow of sub core scale features and the measurement of porosity, permeability, capillary pressure and relative permeability. Multiple studies have shown how small-scale

heterogeneities influence fluid flow. The impact of fractures, laminae and bedding planes on single and multiphase flow has been widely investigated at sub-core scale through core flooding experiments (Alemu, et al., 2013; Hingerl, et al., 2016; Huo & Benson, 2016; Krevor, et al., 2012; Pini & Benson, 2017; Tueckmantel, et al., 2012; Zahasky & Benson, 2018).

2.2. Deformation bands

In highly porous sandstones (porosity > 0.15) strain localization results in the development of deformation bands rather than fractures (Aydin, 1978; Schultz & Siddharthan, 2005; Fossen, et al., 2007). Deformation bands are sub-seismic scale, millimetres to centimetres thick deformation structures (Aydin, 1978; Aydin & Johnson , 1978) formed during fault initiation and damage-zone development (Aydin, 1978; Shipton & Cowie, 2001).

2.2.1. Classification of deformation bands and their petrophysical properties

Deformation bands can be classified based on their kinematics (Fossen, et al., 2018). Three main kinematic classes can be distinguished: simple shear band, pure compaction band and pure dilation band. These can be placed as end members of a triangle shape diagram where at the middle points, classes of bands resulting from the combination of shear and dilation, or shear and compaction can be identified (Figure 2-1).

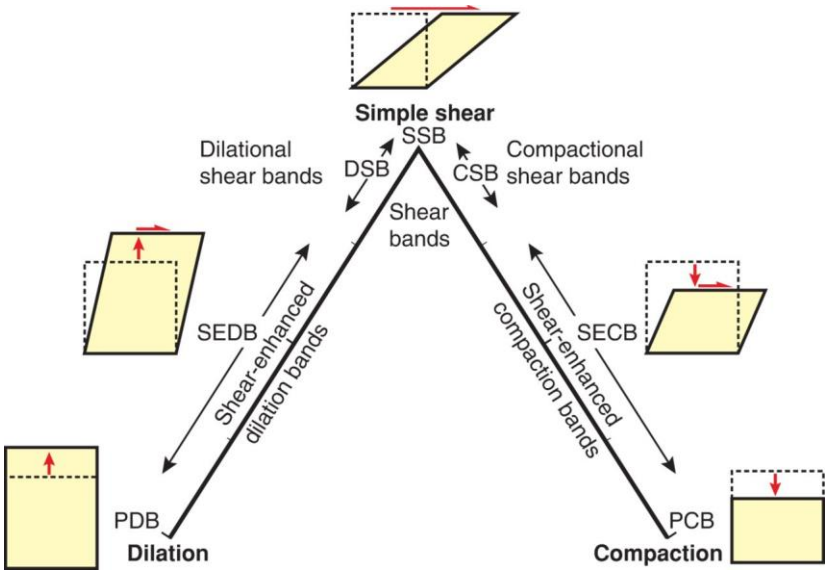

Figure 2-1. Kinematic classes of deformation bands. Simple shear, pure dilation and compaction bands are the end members. Shear-enhanced dilation bands form due to the combination of shear and dilation. Compactional shear form when shear and compaction combine and when the shear component is higher than the compaction one. When compaction and shear have a similar magnitude, instead, shear-enhanced compaction bands form (Fossen, et al., 2018).

Pure dilation bands develop in poorly consolidated sandstones at shallow depth, low overburden pressure conditions. The deformation mechanism consists of grain rotation and translation. Dilation is accommodated in very thin (1-5 mm) tabular layers. Dilation bands are not very common. They have been reported by Du Bernard, et al., (2002) in the Savage Creek marine terrace, northern California, where they accommodate slip along associated shear bands. Dilation band orientation has been found to be parallel to the bisector of the acute angle of conjugate shear bands. Along dilation bands a host rock porosity increase of 7% was observed by Du Bernard, et al., (2002).

Shear dilation bands also occur when confining pressure conditions are low. Antonellini et al. (1994) found shear dilation bands together with shear compaction bands in the Moab Member of Entrada Formation, Utah. The different deformation mechanisms are representative of different sandstone porosity and confining pressure conditions. In the study of Antonellini et al. (1994), along shear dilation bands a host rock porosity increase (image segmentation of thin sections) of 8% has been observed. However later diagenetic processes promoted the filling of these shear dilation bands with iron, calcite or other diagenetic minerals. This is why an overall permeability decrease has been observed along these shear dilation bands.

Simple shear bands show no variation in volume, neither positive dilatancy as dilation bands or reduction of volume as shear compaction bands. Simple shear bands form due to combinations of minor episodes of both compaction and dilation (Fossen, et al., 2018). No change in porosity and permeability is observed along simple shear bands (Fossen, 2010).

Dilation bands, shear dilation bands and simple shear bands can be also defined as disaggregation bands, following the classification of deformation bands based on deformation mechanism (Figure 2-2a). Disaggregation bands refers to all the bands

that form due to grain rolling, translation and breaking of thin film of cement around grains (Fossen, et al., 2007).

Disaggregation bands characterized by high content (0.1-0.15) of platy minerals, such as muscovite, biotite, chlorite, kaolinite) are called phyllosilicate bands (Figure 2-2b) (Knipe, et al., 1997; Fossen, et al., 2007). In this case, the abundance of clay minerals promotes grain sliding. A host rock porosity decrease of 13% and a permeability reduction up to three orders of magnitude is observed along phyllosilicate bands in Torabi and Fossen (2009).

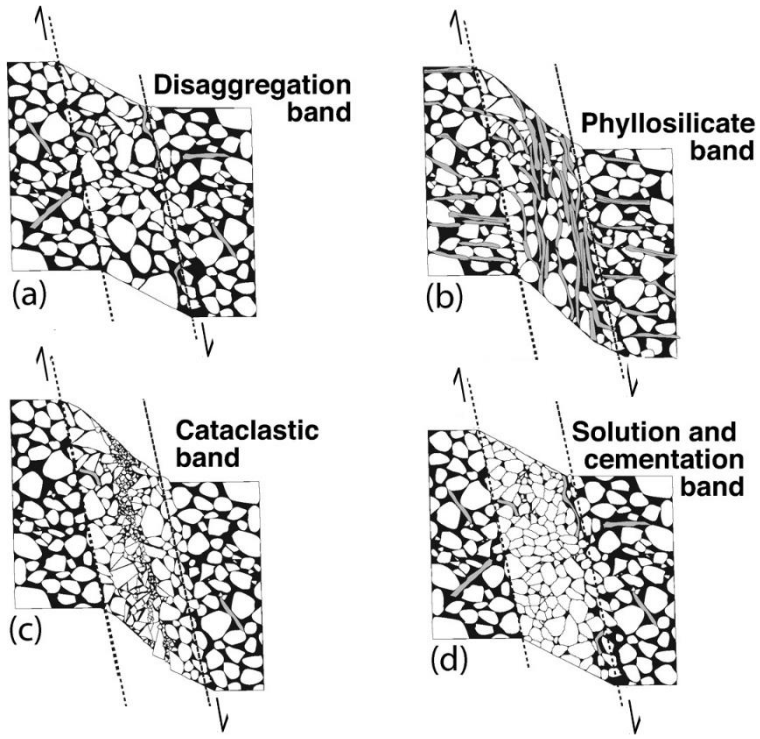

Figure 2-2 a) Disaggregation band due grain rolling and sliding. b) Phyllosilicate band where the sliding and rolling of the grain is favored by phyllosilicate minerals. c) Cataclastic band form due to grain rolling and fracturing. In this case simple shear is combined with compaction. d) Solution and cementation band form due to quartz dissolution and cementation, usually post-deformation. (Fossen, et al., 2007)

Compaction shear bands are mm-thick structures characterized by cataclasis (Figure 2-2c). Cataclasis is the dominant mechanism by which deformation bands form in porous material (Aydin, et al., 2006): here grain sliding and rolling is combined with grain crushing and fracturing. The pore throat dimension along cataclastic bands is extremely reduced compared to the host rock. Compactional shear or cataclastic bands

usually form at depths higher than 1 km, but there has also been evidence of cataclastic bands at shallower depth, i.e. with low overburden pressure, in unconsolidated sandstones (Cashman & Cashman, 2000; Rawling & Goodwin, 2003). In this latter case the cataclasis process is less intense, and the mechanism of grain fracturing is strongly related to the mineralogic content of the host rock. Deformation of felspar minerals leads to intergranular fracturing along cleavage planes; deformation of quartz minerals, instead, creates small fractures at the edge of the single grains and flakes (Rawling & Goodwin, 2003). The cataclastic deformation mechanism promotes decreases in host rock porosity of about one order of magnitude and a consequent decrease in host rock permeability up to six orders of magnitude (Antonellini & Aydin, 1994; Aydin & Johnson , 1978; Ballas, et al., 2015; Deng, et al., 2015; Fossen, et al., 2007; Shipton, et al., 2002; Taylor & Polland, 2000).

Post-deformation grain-contact quartz dissolution and cementation can also occur along cataclastic deformation bands (solution and cementation band), (Figure 2-2d). Intergranular quartz dissolves in water, and is transported by advection-diffusion processes, such as chemical and pressure gradients (Worden, 2004). The dissolved quartz “precipitates on another part of a grain or in some free pore space” (Bright, 2006) (Figure 2-3). Quartz dissolution is usually enhanced at temperatures above 90°C (Walderhaug, 1996). Despite temperature being the most controlling factor on silica solubility (Worden & Morad, 2000), cementation can happen at shallower depths and hence also along disaggregation bands. Cementation is enhanced by highly reactive microcrystalline quartz grains produced by cataclasis (Fossen, et al., 2007). The presence of grain coating clay minerals inhibits cementation in the host rock (Fisher & Knipe, 2001), but enhances it along the deformation bands where the coating is broken due to grain fracturing and crushing (Hesthammer, et al., 2002; Leveille, et al., 1997; Fossen, et al., 2007). In pressure solution or cemented bands, the porosity and permeability are significantly decreased compared to host rock values. Ogilve et and Glover (2001) estimated for southern North Sea sandstones, a host rock porosity reduction of 25%, 50% and 75 % along cataclastic, cemented cataclastic bands and cemented disaggregation bands, respectively. Permeability is up to two and up to five orders of magnitude less than host rock permeability long cataclastic and cemented bands, respectively.

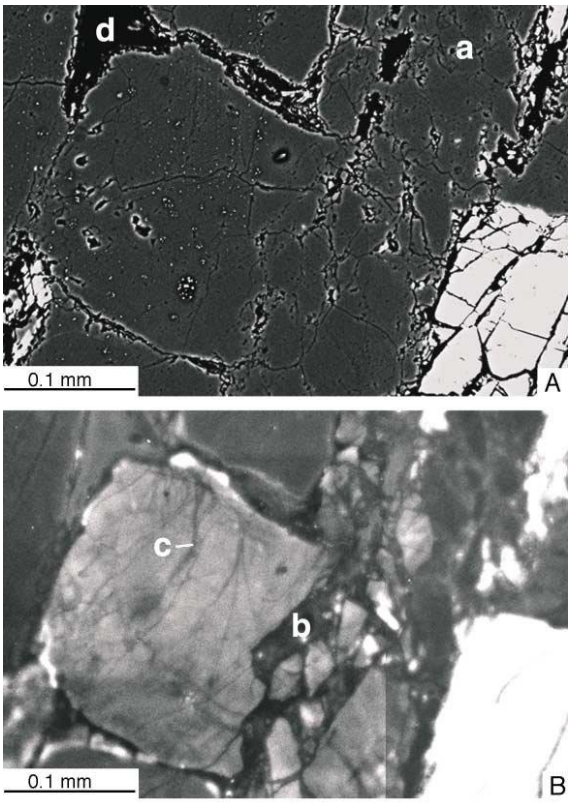

Figure 2-3.A) Backscattered SEM image of a solution and cementation band. Quartz is grey, feldspar is white, voids are in black. a denotes the area where quartz precipitated in the cataclastic deformation band; d is the preserved porosity not affected by quartz cementation. B) Cathodoluminescence SEM image of a solution and cementation band. Quartz cement (in black) precipitated at grain contact (b) and in intergranular fractures (c) (Labaume, et al., 2001).

If compactional shear bands form when the shear component exceeds the compactional one, shear-enhanced compaction bands form when the two kinematic processes have a similar magnitude (Eichhubl, et al., 2010). Shear-enhanced bands are cm thick structures (Figure 2-4a), characterized by less cataclasis and less porosity and permeability reduction when compared to cataclastic bands (Fossen, et al., 2018). Eichhbul et al., (2010) observed a maximum host rock porosity reduction of about 40% along shear enhanced compaction bands. Ballas et al. (2013) reported a porosity reduction of 25% and a permeability reduction from 0 to 1.2 order or magnitude along shear enhanced compaction bands.

Pure compaction bands form in high porosity (> 0.3) and permeability (7-10 Darcy) sandstones (Fossen, et al., 2011). They develop wavy and chevron shapes

(Figure 2-4b) perpendicular to the maximum principal stress (Schultz, et al., 2010). As opposed to pure dilation bands, pure compaction band orientation is parallel to the bisector of the obtuse angle between associated shear or compaction bands (Fossen, et al., 2018). Along pure compaction bands the estimated reduction in host rock porosity (Eichhubl, et al., 2010) is about 50%; the pure compaction bands permeability can be up to four orders of magnitude lower than host rock permeability (Ballas, et al., 2015). Pure compaction bands are rarely found in nature, because they form in uncommon conditions, i.e. shallow depth and high principal stress (Fossen, et al., 2018).

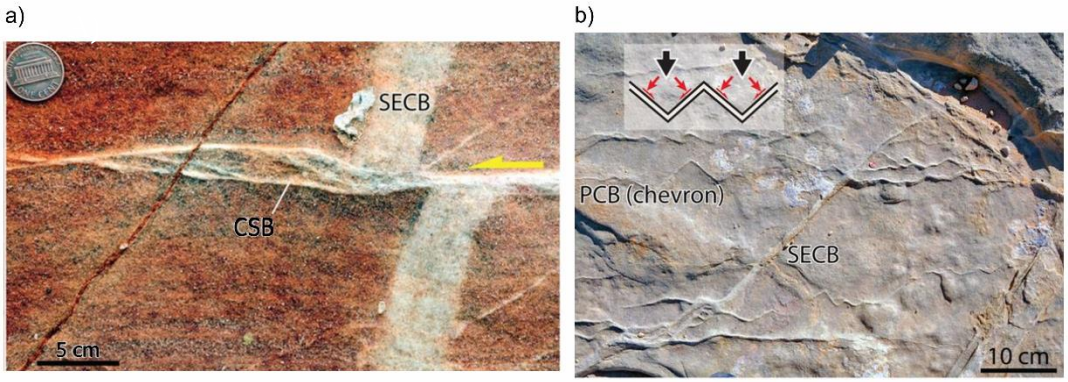

Figure 2-4. a) Shear-enhanced deformation band (SECB) and compactional shear bands (CSB). b) Wavy and chevron pure compaction bands (PCB) and shear-enhanced compaction band (Fossen, et al., 2018).

2.2.2. Distribution

A single deformation band is only able to accommodate small, mm and cm-long, displacements. Once formed, rather than accommodating additional strain, the single deformation band becomes inactive and a new one forms. This process, known as strain hardening, repeats itself and leads to the formation of conjugate sets or up to decimetre thick clusters of deformation bands (Aydin & Johnson , 1978; Shipton & Cowie, 2003). A combination of single bands and clusters of deformation bands is commonly found in the field, as shown in the Figure 2-5.

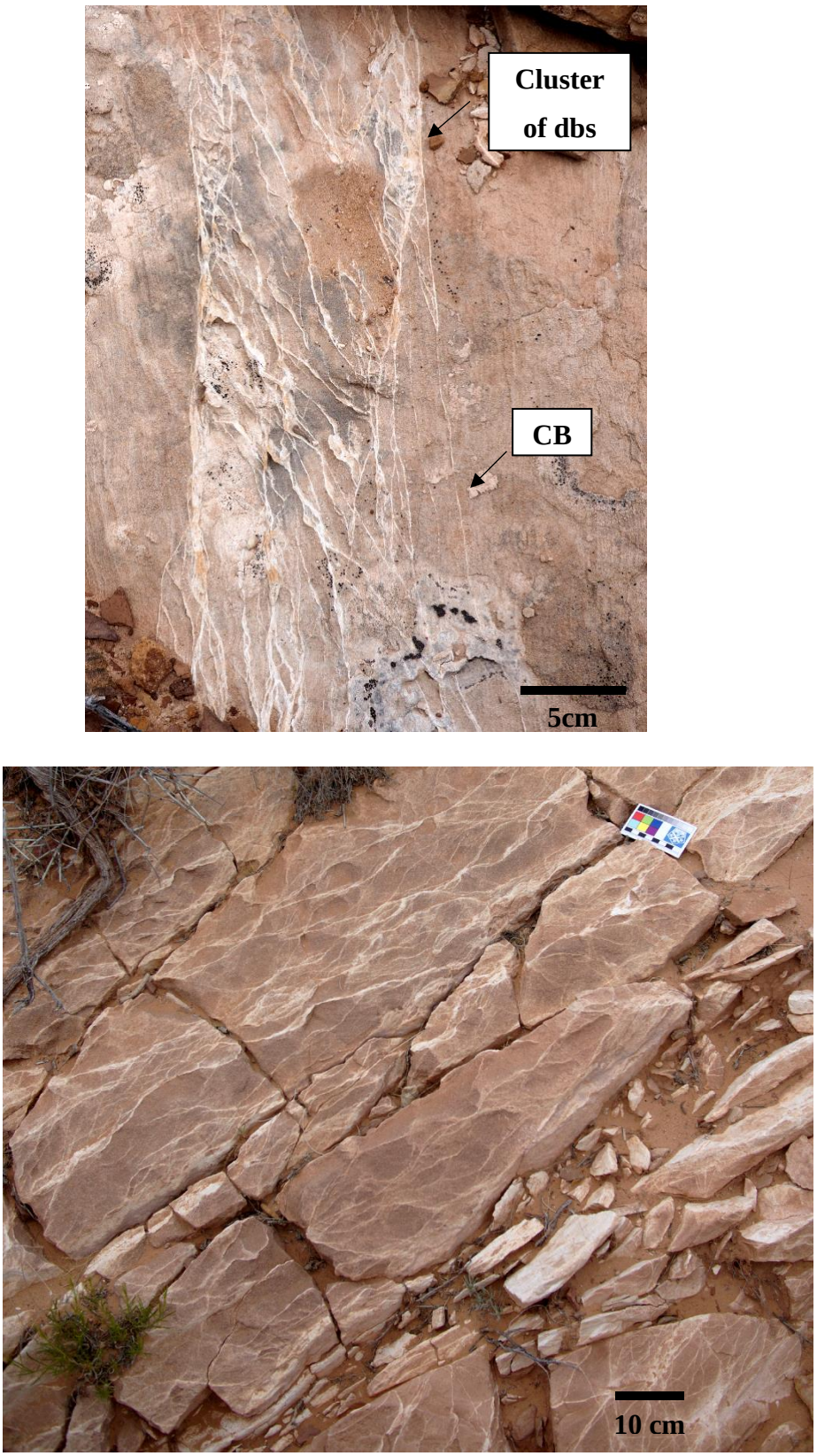

Figure 2-5.(top) Cluster of deformation bands (dbs) and single cataclastic band (CB) in Navajo Sandstone, Utah. (bottom) Anastomosing clusters of bands in Navajo Sandstone, Utah.

Most deformation bands are associated to a specific tectonic origin with the exceptions of disaggregation bands, that can also form in soft-sediment deformations, such as diapirism, syndepositional loading and gravitational instability (Fossen, 2010). Extensional tectonic regimes promote the formation of both disaggregation and cataclastic bands. The reduced minimum horizontal stress at shallow depth favours grain rolling and sliding rather than grain fracturing, and hence the formation of disaggregation bands. Cataclastic bands form in all tectonic regimes, from extensional to strike slip to contractional (Fossen, et al., 2018) while shear-enhanced compaction bands and pure compaction bands occur only in contractional regimes (Soliva, et al., 2013).

Cataclastic bands are mainly found around normal faults, in the so called damage zone, which is the volume of rock that accommodates deformations during initiation and propagation of slip along the fault (McGrath & Davison, 1995; Rotevatn & Fossen, 2011; Shipton & Cowie, 2003). The width of the damage zone increase as the fault grows (Figure 2-6a) (Schueller, et al., 2013). However, damage zone thickness – displacement fault relationship changes if the damage zone is dominated by fractures or deformation bands (Choi, et al., 2016) (Figure 2-6b) and if the displacement is over 100 m (Torabi, et al., 2019) (Figure 2-6c).

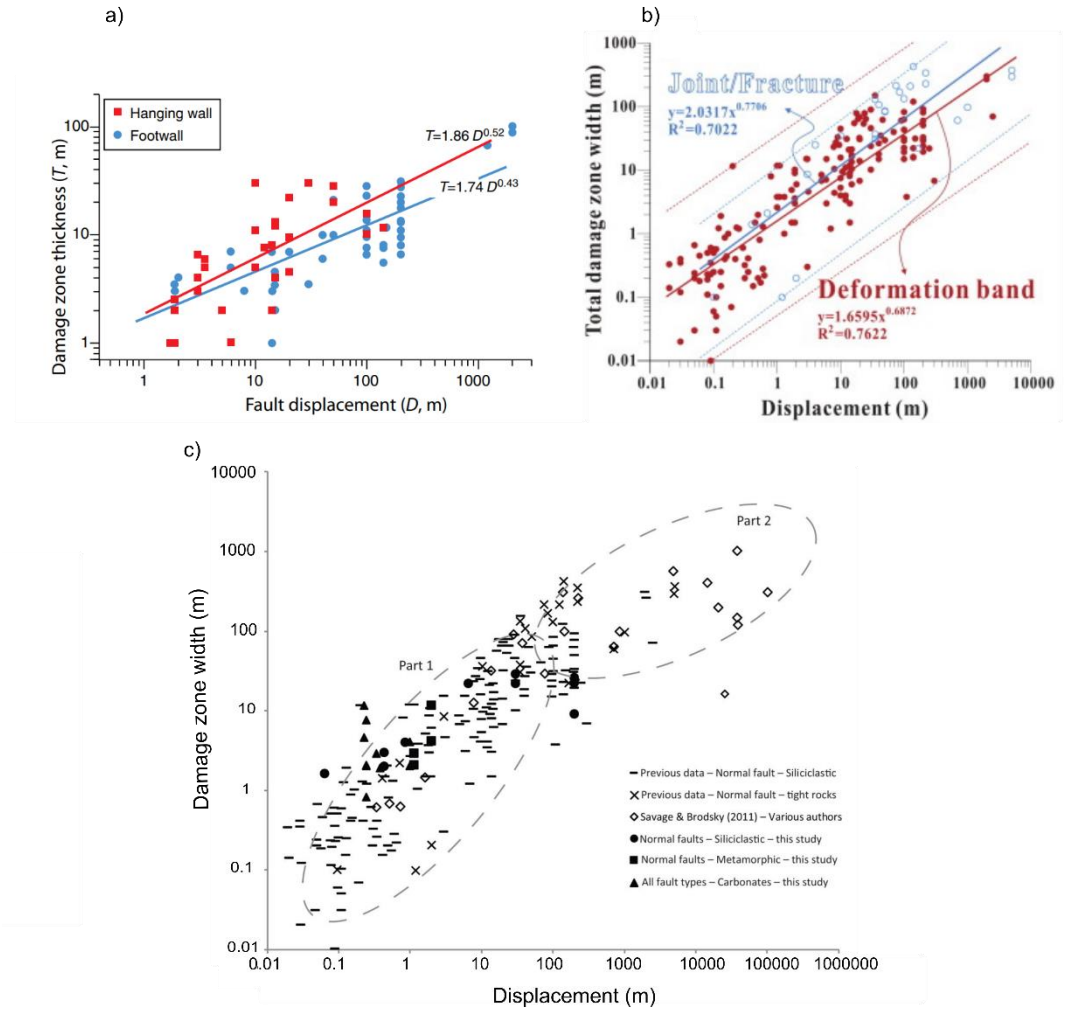

Figure 2-6. a) Damage zone thickness increases exponentially with fault displacement. A wider damage zone is found in the hanging wall. Several damage zones are considered in these statistics (see Schueller, et al., 2013), (Fossen, et al., 2018). b) Damage zone thickness and displacement relationship is different if the damage zone is fracture- or deformation band-dominated (Choi, et al., 2016). c) Damage zone thickness and displacement relationship changes if displacement is higher than 100 m (Torabi, et al., 2019).

There is no known relationship between fault displacement and the frequency of deformation bands (Schueller, et al., 2013). This means that it is not possible to distinguish small and large faults based on the density of their associated deformation bands. Regardless of fault displacement (and hence size of structure) the frequency of deformation bands logarithmically decreases with distance from the fault (Figure 2-7) (Schueller, et al., 2013). A higher permeability reduction, induced by clusters of bands, is found closer to the fault core (Shipton, et al., 2002)

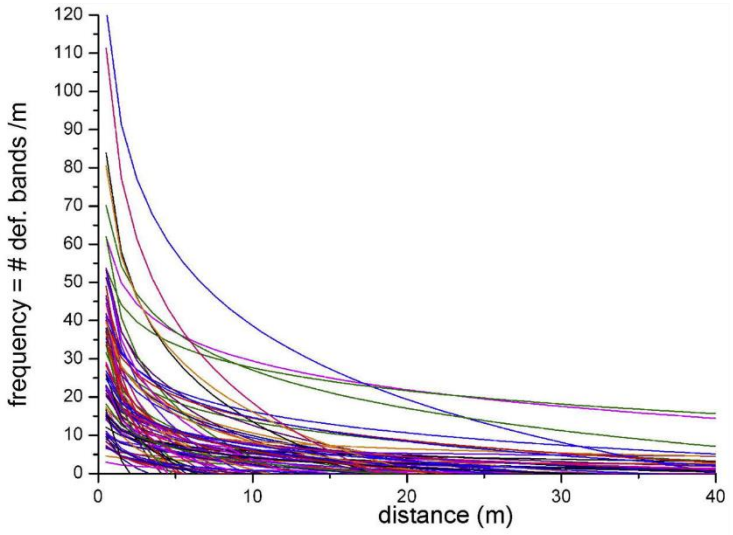

Figure 2-7. Frequency of deformation bands decreases with increase of distance from the fault. The logarithm fit model used is Y=A+L ln(X), where Y is the number of deformation bands per meter, X is the distance from the fault core, and A and L are constants. Database includes 106 fault zones scanlines acquired in porous sandstone formations of Sinai, Utah, Corsica, England, Svalbard and Netherland. See Shueller et al. (2013) for details.

Cataclastic bands are also characteristic of the process zone; the portion of deformed rock beyond the fault tip (Shipton & Cowie, 2001). Figure 2-8 shows a schematic model of a normal fault, including damage and process zone (Fossen, et al., 2007). While the length of the fault can be predicted based on several theoretical models of fault displacement gradient (Cowie & Shipton, 1998), the length of the process zone is variable and mostly dependent on the properties of the deformed rock. In the example provided by Rotevatn & Fossen (2011) of the east side of the Cache fault, Utah, the process zone extends for 350 m and includess clusters of deformation bands, each of them characterized by at least 40 bands.

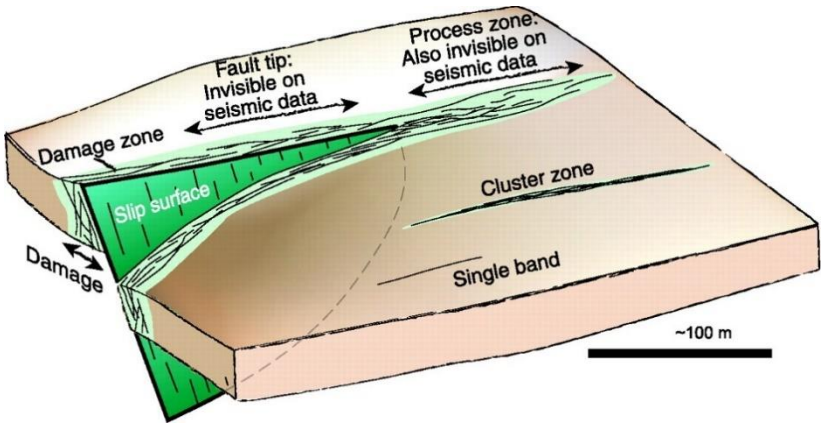

Figure 2-8. Schematic model of slip surface, damage zone and process zone. The last two are characterized by deformation band clusters and single deformation bands. The extension of the process zone can be up to several hundred meters beyond the fault tip (Fossen, et al., 2007).

Finally, the interaction between more than one fault may create more complex overlapping zones with wider damage zones (Shipton & Cowie, 2003), characterized by synthetic and antithetic clusters of deformation bands.

Fault tip process zones are below the seismic resolution and can't be solved by inverting seismic profiles. Moreover, seismic reflection data of complex fault zone geometries are usually noisier (Rotevatn & Fossen, 2011) and interpretation of complex geological structures and their extent is extremely challenging.

2.2.3. Deformation band orientation

Orientation of deformation bands, together with type of deformation bands, is influenced by the applied stress. Ma and Haimson (2016) performed uniform confining and true triaxial stresses experiments for understanding rock failure, type and orientation of deformation bands on a Bentheim sandstone and a Coconino sandstone. The samples are characterized by similar mineralogical content (≥95% of quartz), but their grain geometry and porosity differ. Rounded grains and porosity of about 17% characterize the Coconino samples; subangular grains and a porosity of 24% is observed in the Bentheim samples. A first experiment consisted in applying uniform confining pressure conditions to the sample ($\sigma_2 = \sigma_3$). In both samples, by increasing the value of σ_3 (and σ_2) a decrease in the angle of the failure plane is observed. In the Coconino sample (Figure 2-9a) when σ_3>80 MPa, multiple and conjugate shear bands appear. In the Bentheim sandstone (Figure 2-9b) when σ_3>50

MPa shear enhanced compaction bands form (angle < 45); when σ_3=150 MPa, pure compaction bands (angle = 0°) develop.

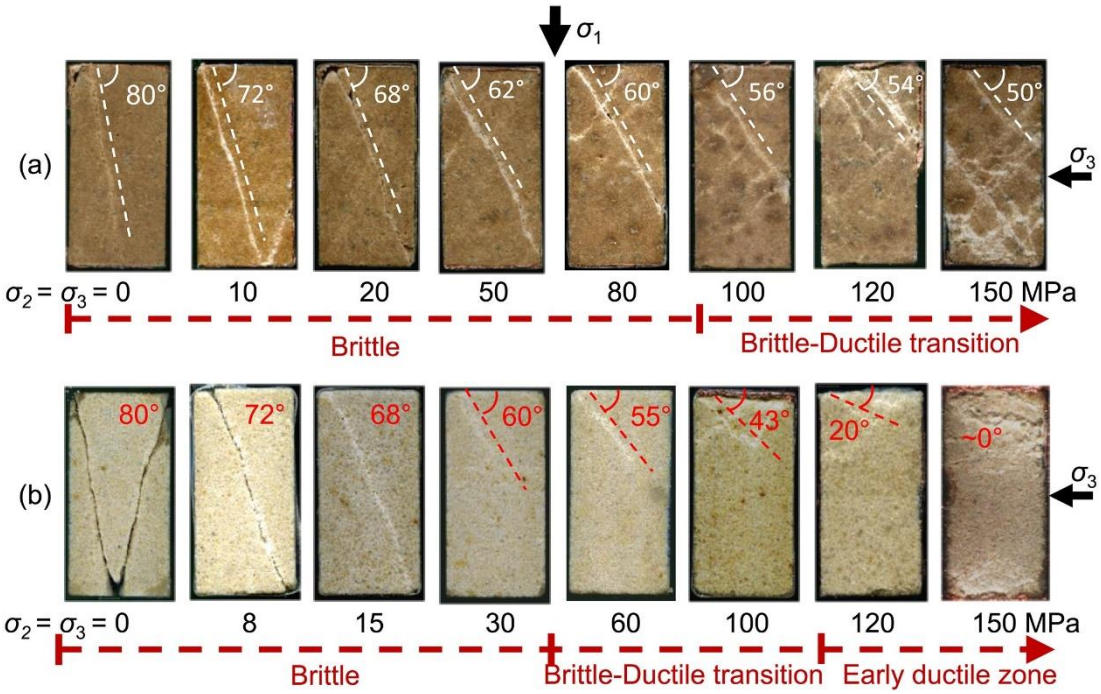

Figure 2-9.a) Failure in Coconino sandstone samples for increasing value of σ_3, when $\sigma_2 = \sigma_3$. b) Failure in Bentheim sandstone samples for increasing value of σ_3, when $\sigma_2 = \sigma_3$ (Ma & Haimson, 2016).

True triaxial experiments were performed by increasing σ_2 for constant σ_3 values. In the Coconino sandstone, deformation bands angle decreases for increasing values of σ_2. When σ_3=100 MPa, no conjugate and parallel bands are shown as in the previous experiment. Also in Bentheim sandstone samples the angle of the failure plane increases when σ_2 increases; however, no influence of σ_2 value is observed when σ_3 = 150 MPa. The more compactive behaviour is to address to the higher porosity of Bentheim sandstone compared to Coconino sandstone.

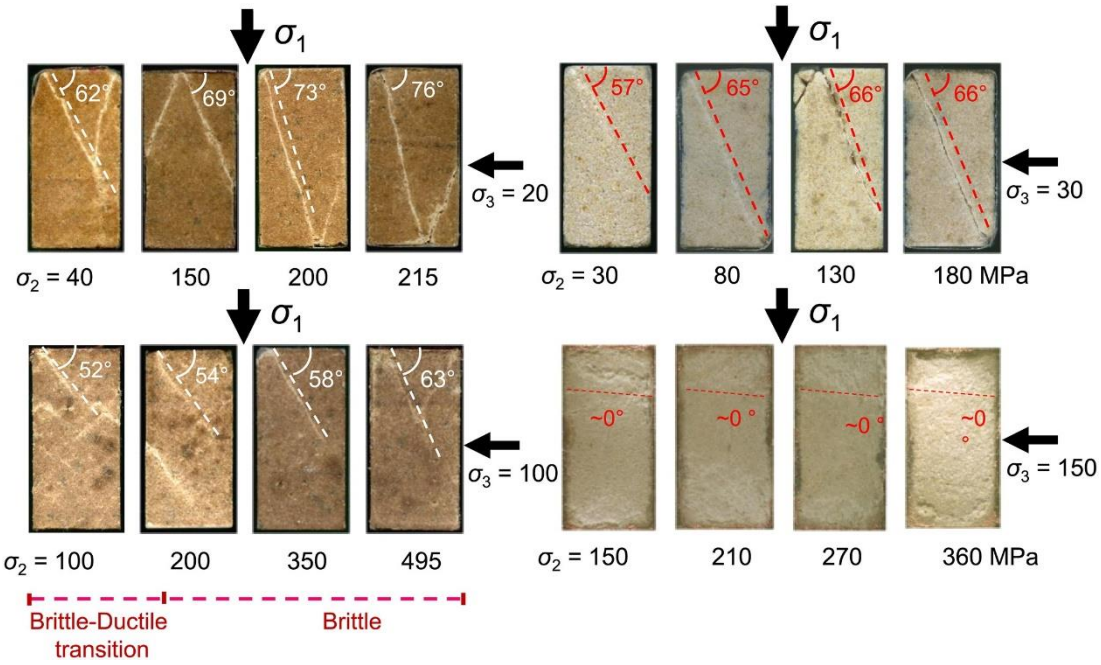

Figure 2-10. Failure of the Coconino sandstone (left) and Benthaim sandstone (right) when increasing σ_2 is applied for constant values of σ_3.

2.2.4. Influence on fluid flow: previous studies

As mentioned in the section 2.2.1, significant porosity and permeability reduction is observed along cataclastic bands, clusters of bands and dissolution and cementation bands. Shear-enhanced compaction bands also present reduced permeability and have higher thickness, but they are less vertically and laterally extensive and less common than cataclastic bands (Ballas, et al., 2015). As a consequence, cataclastic bands and dissolution cementation bands have received more attention since they have a greatpotential to strongly influence fluid migration, acting as barriers to flow.

The reduced pore throat size along cataclastic and cemented deformation bands influences not only petrophysical (porosity, absolute permeability), but also multiphase properties. Capillary entry pressure along cataclastic and cemented bands is higher than capillary entry pressure of the surrounding host rock. More details about capillary pressure and its relationship with pore throat radius are provided in section 2.4.2. Olgive et al. (2016) measured the capillary entry pressure of samples containing host rock or cataclastic and cemented deformation bands with MICP (Mercury Injection Capillary Pressure). The average capillary entry pressure estimated for deformation bands was 1.9 MPa, against the 440 kPa estimated for the host rock. These

values refer to a system where mercury (Hg) is injected into dry sample (filled with air). For calculating the capillary pressure considering another fluid pair ($P_{c\,(12)}$), the following equation can be used

$$P_{C\,(12)} = \frac{(\sigma\, cos\theta)_{12}}{(\sigma\, cos\theta)_{Hg/air}}\; P_{C\,(Hg/air)}, \tag{2-1}$$

where σ is the interfacial tension of the fluid pair, and θ is the contact angle. If the fluid pair consists, for example, of CO_2 and water (considering a σ = 480 mN/m and a θ= 130° for Hg/air and a σ = 35 mN/m and a θ= 40° for CO_2/water), the capillary entry pressure of cataclastic bands and host rock becomes respectively 165 kPa and 38 kPa.

The interfacial tension is dependent on fluid pairs, temperature and pressure conditions. Contact angle value changes depending on fluid pair, solid material in contact with the two fluids, temperature and pressure. A different contact angle value should only be observed along deformation bands if the mineralogical content of deformation bands is changed compared to host rock, such as for clay filled deformation bands or cemented deformation bands. Explanations about interfacial tension and contact angle concepts are provided in section 2.4.2.

Several studies were conducted for understanding the role of deformation bands on fluid flow (Naruk, et al., 2009; Ogilvie, et al., 2001; Qu & Tveranger, 2016; Qu, et al., 2017; Rotevatn & Fossen, 2011; Rotevatn, et al., 2017; Schultz & Siddharthan, 2005; Shipton, et al., 2002; Shipton, et al., 2005; Wilkins, et al., 2019). All the mentioned studies highlight how deformation bands can be responsible for permeability decrease in a reservoir, fluid compartmentalization, a higher degree of tortuosity and fluid bypass. For example, Rotevatn et al. (2017) conducted reservoir simulations to understand the effect of deformation bands on water migration in a saturated oil reservoir. The results show that the presence of deformation bands causes a delay in the arrival time of the water in the production well, a higher degree of tortuosity, and a decrease of the total water saturation at the end of the simulation. These effects are more pronounced in the case of deformation band clusters, which result in a larger permeability reduction.

Another study (Rotevatn & Fossen, 2011) investigated the effect of deformation bands in the process zone. Deformation band geometries derived from field observations were implemented in reservoir simulations. Water was injected into an oil reservoir, through individual vertical injection and production wells. They found that deformation bands reduced permeabilities in the process zone and acted like capillary barriers. This resulted in an increase in the pressure gradient when fluid approached the process zone.

Wilkins et al. (2019) studied the impact of subsurface deformation bands on hydrocarbon production in Holstein Field, Gulf of Mexico. Cataclastic deformation bands were mainly found in the hinge zone of a monoclinal fold in the sandstone reservoir. Well pressure data and core analysis confirmed that the presence of cross-cutting, low and high angle dipping (to the bedding planes) deformation bands were responsible for a reservoir permeability decrease and reservoir compartmentalization.

Some authors have suggested that the segregation of fluid in several pressure/saturation compartments by deformation bands (reservoir compartmentalization) may not really happen. Medeiros et al. (2010) states that damage zones are horizontally and vertically finite volumes, and hence suggests that fluid will simply bypass the deformation band zone. Tindall (2006) observed the presence of equally spaced joints that form later and cut across deformation bands. If present, such joints would act as preferential pathways for fluids and thus connect individual compartments within a reservoir.

2.3. Micro computed tomography

X-ray computed tomography is an imaging technique that allows visualization of three-dimensional objects, without compromising their integrity. Before the 1990s, X-ray imaging was mostly utilized in medical science, however, in the last 30 years it has been shown to be a useful tool within several subdisciplines of Earth Science (Wellington & Vinegar, 1987; Cnudde, et al., 2006; Lager, et al., 2008; Mooney, 2002; Mooney, et al., 2012; Perrin, et al., 2009; Van Geet, et al., 2000). The high-resolution achieved within X-ray micro computed tomography (μCT) allows for detailed

characterization of pore-scale geometry at a core-scale and can be used to determine the petrophysical properties.

2.3.1. Basic principles

All X-ray instruments are characterized by a source-sample-detector system. A point or linear source produces a beam of X-rays (photons) that traverses the sample. The sample acts like a filtering system and the resulting attenuated radiation is measured by a linear or planar detector. The beam shape depends on the source and detector geometry. High-resolution images are usually produced by cone-beam shaped systems (Lechuga & Weidlich, 2016), where the beam is emitted from a single point and detected by a planar detector (Scarfe & Farman, 2008). In this case, both source and detector are fixed and the sample is placed on a rotating table to enable acquisition of images through step-by-step rotation (very small angles) (Figure 2-11); the smaller the acquisition step (angle), the larger the number of projection views (images acquired) and the faster the reconstruction process.

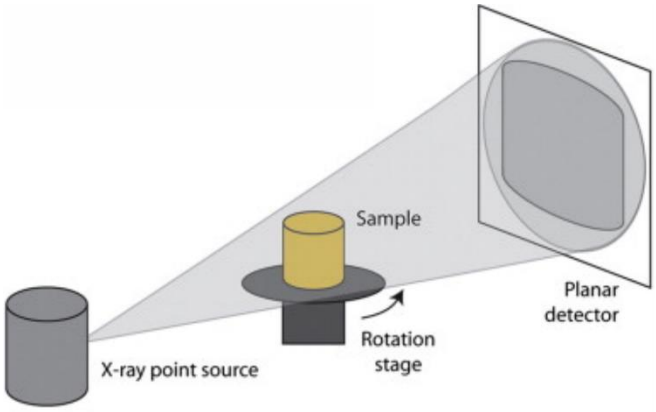

Figure 2-11. Schematic model of cone beam geometry (Kyle & Ketcham, 2015).

Filtered Back Projection (FBP) (Feldkamp, et al., 1984) is the most used algorithm for 3D reconstruction. This is usually preferred because it is computationally less intensive, and thus faster, than iterative methods. The FBP algorithm relies on the assumption of a monochromatic source, i.e. on emitting waves with the same wavelength. For a monoenergetic source, it applies the simplest version of Beer's Law (Eq. 2-2).

$$I = I_0 \, e^{-\int \mu(s) ds} \tag{2-2}$$

Here I and I_0 are final and initial energy, μ is the linear attenuation coefficient (unit: 1/length) for the specific material and s is the ray path (Cnudde & Boone, 2013). Considering this equation, the X-ray is uniformly attenuated when it passes through the sample and the attenuation depends on the X-ray's initial energy, the path length, and the sample's composition. After the reconstruction process, several 2D cross sectional images (slices) are produced; this stack of 2D images enables 3D reconstruction.

2.3.2. Beam hardening artefact

The assumption of a monochromatic source implemented in the FBP reconstruction method leads to several image artefacts. Actual sources have often a polychromatic nature and emit X-rays at different energies. Low energy photons are more easily absorbed by the sample material and the resulting beam is characterized by higher energy photons (Achterhold, et al., 2013). The sample material is less efficient in absorbing the "hardened" beam. This results in short pathways (at the edge of the sample) being more attenuating than long pathways (centre of the sample) (UTCT, 2016). This phenomenon is called beam hardening and, in case of a monochromatic source assumption, it produces a false high attenuation value at edge of the sample in the resulting images (the cupping effect) (Brooks & Di Chiro, 1976). An example of the beam hardening artefact is shown in Figure 2-12.

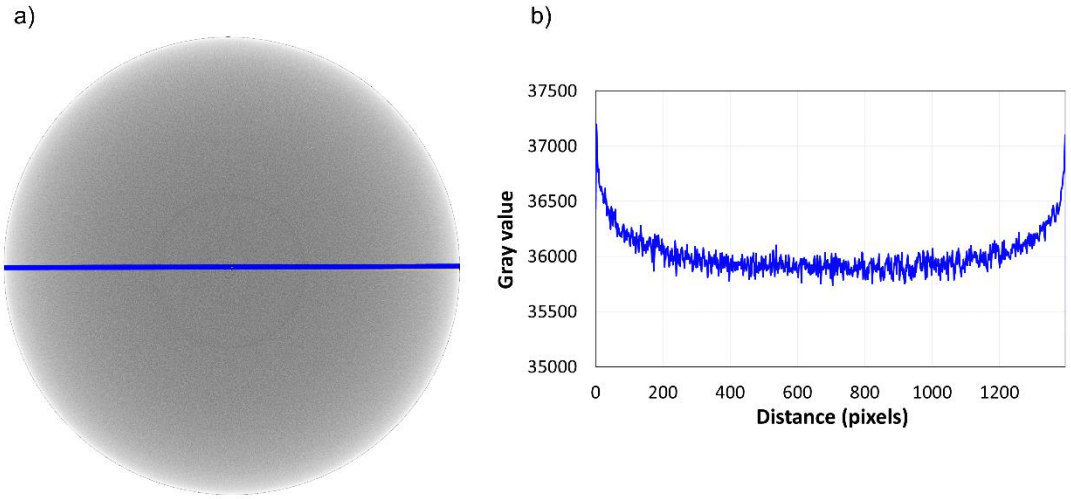

Figure 2-12. a) Slice of a plastic rod scan affected by the beam hardening artefact. b) Plot of attenuation values along the blue profile the Figure 2-12a.

2.3.3. Beam hardening correction: previous methodologies

Until now several corrections have been proposed based on different modalities: pre-filtering correction methods, iterative reconstruction methods, and linearization correction methods.

The pre-filtering approach is widely used and consists of placing a physical filter between the source and object (Jennings, 1988). The filter's function is to minimise the low energy X-rays before they pass through the object, creating a quasi-monochromatic source. This technique often requires a longer exposure, and consequently increases the scan time compared to a scan without filters but with the same X-ray energy and current. Filters can be characterized by different thicknesses and materials (aluminium, copper, tin, silver, etc.). Multiple trials are often needed to choose a filter suitable for removing beam hardening. In some cases, the cupping effect can be reduced but not completely removed.

Iterative reconstruction methods consist of assuming an initial object structure and density, calculating its projections and comparing the calculated projections with the acquired ones. In the case of a misfit between the calculated and measured projections, the initial structure is changed until conversion is reached (Gilbert, 1972). At present, several iterative methods can be used to produce slice images (ART, SART, SIRT, MLEM, etc.). Despite these methods are often integrated into open source toolboxes (Biguri, et al., 2016), there are still limitations related to the amount of data that can be processed. With large datasets the computational load of iterative reconstruction methods means they are not feasible for use on a standard desktop computer.

Linearization methods can be discretized into pre-reconstruction linearization methods and post-reconstruction linearization methods. Pre-reconstruction linearization method consist of applying, to the projection data (raw data), a polynomial or exponential correction function. In pre-reconstruction linearization methods, the relationship between attenuation and path length is defined through a calibration scan made on a phantom object (e.g. an object of known density and geometry) (Herman, 1979; Yan, et al., 2000). These methods are usually suitable for single material precorrections and they do not require *a priori* known shape and size

of the phantom object or a specific distance source-phantom (Kachelrieß, et al., 2006; Ritschl, et al., 2010). They are, however, less effective than iterative methods for correction of the beam hardening effect on multi-material objects. The phantom object is representative of the sample only if where there is a simple spatial variation of physical properties and all the densities of the materials are known.

Linearization can be also determined by pre-determined correction profiles, custom user-specified correction profiles, and custom auto-detected correction profiles, such as those utilized by CT pro 3D, Nikon Metrology. In pre-determined correction profiles, the software proposes fixed coefficients for linearization of the beam hardening curves. The coefficients are not calculated for each sample, and therefore they don't always provide accurate corrections, especially for zoomed-in scans. Although coefficients can be manually changed (user-specified correction profiles), they are still randomly chosen. The only automatic correction provided by the software is the *custom* option, based on the sinogram of the full sample. The sinogram is the product of the stack of the attenuation profiles obtained at different projection angles (Chityala, et al., 2005). This correction often produces additional noise and shading artefacts, especially in the case of multi-material objects.

Another post-reconstruction linearization processes is the method proposed by Jovanović et al. (2013), in which the beam hardening correction conducted is contemporaneously to the local segmentation of the images. The procedure consists of calculating beam hardening curves for each phase identified in the sample. The method can be time consuming and is not suitable for samples where no clear distinction between mineral phases is possible.

Ketcham & Hanna (2014) developed an auto-detected correction profile algorithm for heterogeneous geological samples. The user identifies some regions of interest, each of them including a single material. The method consists of minimizing CT number variation in a single region, or several regions, that are characterized by beam hardening. Whilst effective, this method requires an expert user able not only to identify beam hardening artefacts, but also to discretize different materials. Further, a clear distinction between different materials may not be possible, particularly in case of low-resolution X-ray images or geological features such as graded bedding.

2.4. Core flooding experiments

Characterization of reservoir properties and estimation of reservoir potential are achieved by integrating several data sources, such as laboratory tests, seismic data and field tests (Glover, 2001). Core flooding experiments are a laboratory technique that is commonly conducted for estimating petrophysical and multiphase properties at reservoir pressure and loading conditions.

2.4.1. Methodology

During core flooding, fluid displacement at a specific burial depth and temperature is mimicked by placing the core sample into a core holder, connected to a core flooding setup. The core flooding setup and core holder vary based on the purpose of the study. The core flooding setup is usually characterized by several injection and collecting fluid pumps, confining pressure pumps for applying an overburden pressure, and back pressure pumps (or a regulator) for keeping a constant outlet pressure. Pressure transducers are placed at the inlet and outlet of the core for monitoring differential pressure. Additional components can be included in the core flooding setup, such as a water exchange bath for injecting fluid at certain temperatures and a fluid separator for continuous circulation of fluids. Details of a core flooding experimental setup can be found in section 4.2.4.

Integration of core flooding experiments with more advanced imaging techniques has allowed sub-core scale observation of fluid flow behaviour and measurement of porosity, permeability, capillary pressure and relative permeability (Akbarabadi & Piri, 2013; Akin & Kovscek, 2003; Krause, 2012; Krause, et al., 2013; Krevor, et al., 2012; Perrin, et al., 2009; Pini, et al., 2012; Zahasky & Benson, 2018). The image techniques most used in combination with core flooding experiments are X-ray CT and Positron Emission Tomography (PET).

For capturing fluid behaviour, medical X-ray CT is preferred to most micro-CT imaging systems as the acquisition process is faster. X-ray CT acquisition is performed in a few minutes, but a lower resolution of scan images (mm scale) is achieved. The physical principles of medical X-ray CT are the same as those explained in section 2.3.1, but linear array of detectors is used (Zeng, 2010). In the last generation

of medical CT scanners, both the source and the linear arrays rotate, while the object remains fixed.

PET imaging relies on the coincidental detection of gamma rays oppositely emitted by electron-positron annihilation (Figure 2-13). Firstly, the sample is injected with a solution of water and positron-emitting radionuclides. Due to the neutron-deficiency nature of positron emitters, a single proton is trans-mutated in a single neutron, producing a positron and electron neutrino. The energy of the positron is attenuated by the material in which the solution travels until annihilation happens (Townsend, 2004). PET imaging is extremely valuable for quantifying radiotracer migration through a sample (Pini, et al., 2016; Zahasky & Benson, 2018).

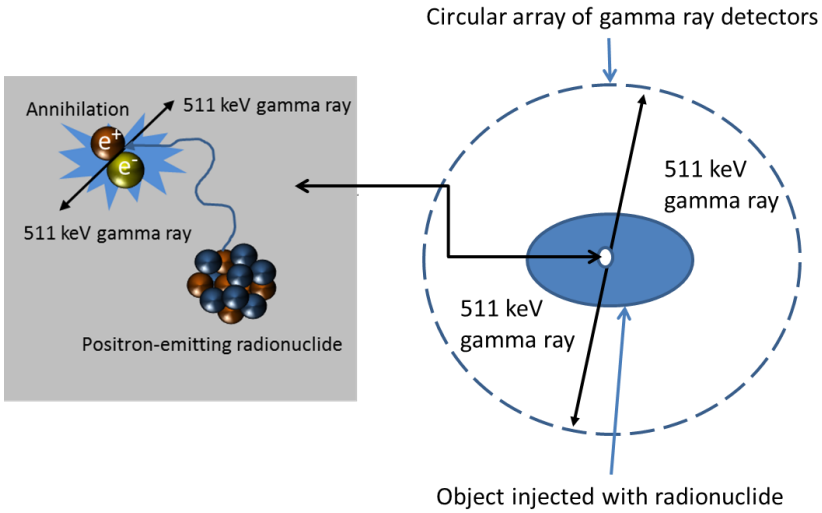

Figure 2-13. Basic principles of positron emission tomography. Annihilation is due to electron-positron collision. This produces two oppositely oriented gamma rays, detected by circular arrays of detectors (Manitoba, 2018).

2.4.2. Petrophysical and multiphase property characterization

Core flooding experiments and acquisition of scan images with a range of experimental conditions can enable measurements of 3D porosity distribution, bulk permeability, and the estimation of capillary pressure and relative permeability curves.

Porosity is defined as the quantity of voids in a material. It is the volume fraction between the void phase and the bulk rock volume. Characterization of sub-core scale porosity can be achieved by acquiring sets of scan images of the core in dry and fully water-saturated conditions (Withjack, 1988; Akin & Kovscek, 2003). It is

important that the location of the samples doesn't change between the two scans. The average porosity in a given representative elementary volume (REV) is then calculated as follows,

$$\Phi = \frac{CT_{wat} - CT_{dry}}{I_{water} - I_{air}} \tag{2-3}$$

where CT_{wat} and CT_{dry} are CT numbers of the fully water-saturated and dry core, respectively. I_{water} and I_{air} are the CT numbers of water and air, expressed in Hounsfield units (HU). It is common to assign a value of -1000 HU to air and 0 HU to water. For reducing error due to CT number variations during the acquisition process, Pini et al. (2012) suggest acquiring at least three sets of images for each condition and averaging them. An example of porosity calculated through wet and dry scans is shown in Figure 2-14.

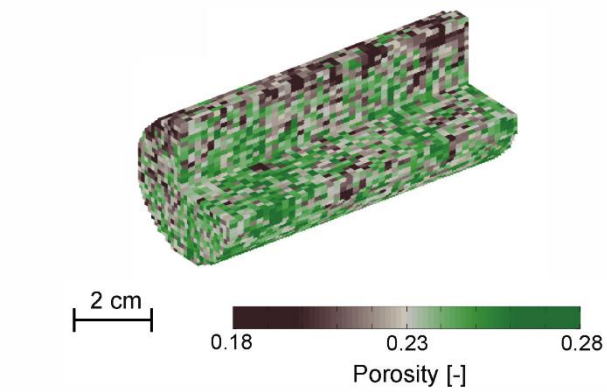

Figure 2-14. Sub-core scale porosity of a Heletz core sandstone (Hingerl, et al., 2016). Voxel dimension is 1.17×1.17×1 mm.

Bulk absolute permeability is the ability of the porous media to transmit fluid. It can be measured by injecting water at several flow rates in the fully water-saturated sample and measuring the pressure drop across the core using two pressure transducers placed at the inlet and outlet of the core. Darcy's Law for a single fluid therefore applies,

$$k = \frac{q\mu}{A}\frac{L}{\Delta P} \tag{2-4}$$

Here k is the bulk permeability (m^2), q is the volumetric flow rate (m^3/s), μ is the dynamic viscosity (Pa·s) at temperature and pressure conditions of the experiment, L

is the length of the sample (m), A is the cross sectional area of the sample (m^2) and ΔP is the differential pressure (Pa).

In situ single phase fluid behaviour in core flooding experiments can be captured by radiotracer-pulse injection, with PET images being taken prior to radiotracer breakthrough (Pini, et al., 2016; Zahasky & Benson, 2018). The water-radiotracer solution is injected into the fully water-saturated samples at a range of flow rates with confining pressure being applied to avoid fluid bypass. Reconstruction of PET images then allows visualization of radiotracer concentration along the core, at time intervals of several seconds (20-40s) depending on the material and acquisition settings. An example of a single phase PET experiment is shown in Figure 2-15.

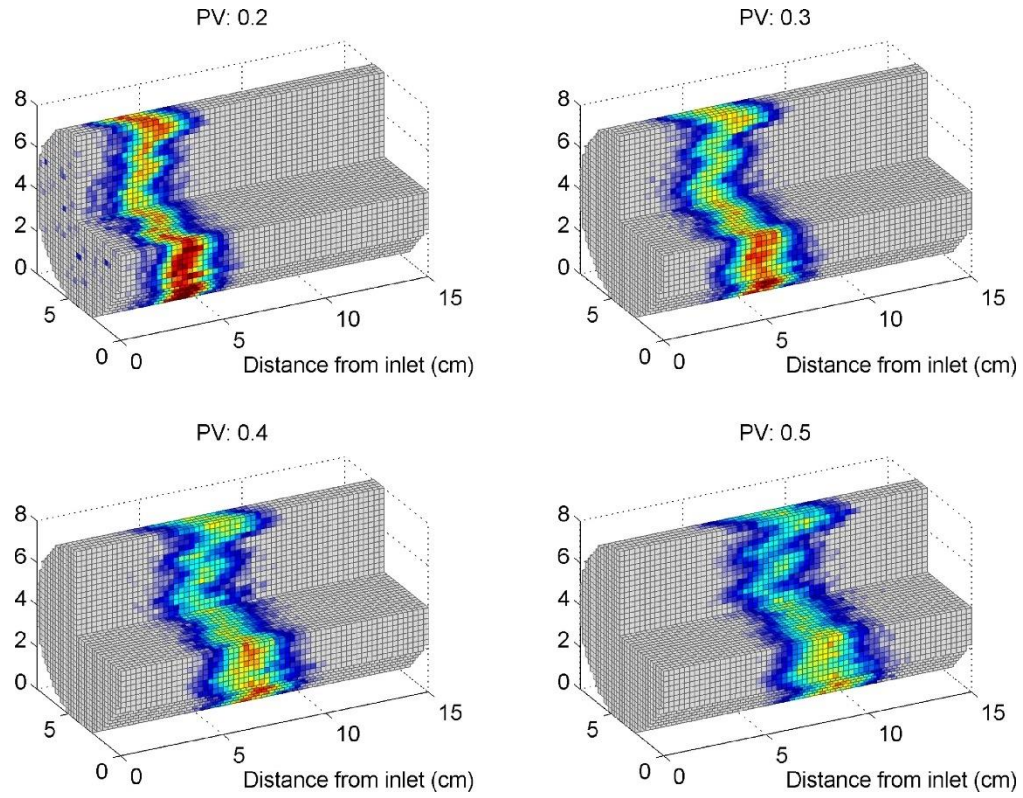

Figure 2-15. Radiotracer concentration distribution at progressive higher pore volume of radiotracer injected at 5 ml/min in a Berea sandstone (Zahasky & Benson, 2018).

Multiphase fluid behaviour in core flooding experiments is captured by acquiring X-ray scan images in three different conditions: the core fully saturated with the injected fluid, the core fully water-saturated with the displaced fluid and the experimental conditions during injection. If a case with injection of CO_2 (non-wetting phase) or CO_2 and water (wetting phase) in a fully water-saturated sample is

considered, the CO_2 saturation and the water saturation can be calculated as follows (Akin & Kovscek, 2003).

$$S_{CO_2} = \frac{CT_{exp} - CT_{water}^{sat}}{CT_{CO_2}^{sat} - CT_{water}^{sat}} \quad \text{and} \quad S_{water} = 1 - S_{CO_2} \tag{2-5}$$

Here CT_{exp} are the CT numbers of the scan images at experimental conditions; CT_{water}^{sat} and $CT_{CO_2}^{sat}$ are CT numbers of X-ray images acquired when the core is fully saturated with CO_2 and water, respectively. To determine the porosity distribution, it is advised to acquire and average several sets of images for each of these conditions to reduce background noise (Pini, et al., 2012). Figure 2-16 shows an example of CO_2 saturation measured during injection of CO_2 and water into a fully water-saturated sample.

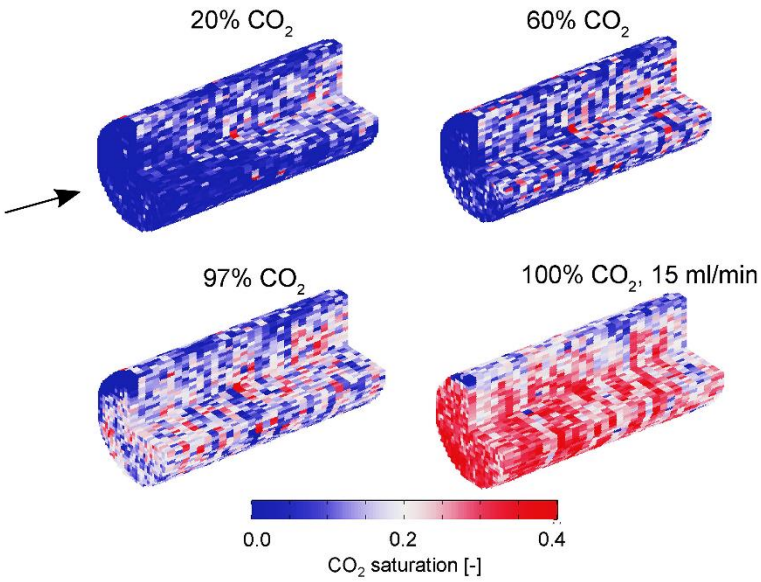

Figure 2-16. CO_2 saturation distribution after injecting CO_2 and water (except for 100% CO2 case) in the fully water-saturated Heletz sandstone core (Hingerl, et al., 2016). Porosity of the sample is shown in Figure 2-12.

Capillary pressure is defined as the difference in pressure between two immiscible fluids along their curved interface. If the pore spaces are assumed to be cylindrical tubes, the capillary pressure is inversely proportional to the radius of the tube, as described by the Washburn equation (Eq. 2-6). A reduction in pore throat size leads to an increase of capillary pressure and capillary entry pressure values (capillary pressure condition at which one fluid starts being displaced from the other), as seen for deformation bands.

$$P_C = \frac{2\sigma \cos\theta_c}{r_c} \quad (2\text{-}6)$$

Here σ is the interfacial tension (N/m) , θ_c is the contact angle and r_c is the radius of the tube (m) (Fanchi, 2002). The interfacial tension is due to the cohesive forces between molecules at the fluid-fluid interface. Its value depends on fluid pair, temperature and pressure conditions. A decrease in the interfacial tension value is observed for increasing pressure and temperature (Bachu & Bennion, 2009; Chiquet, et al., 2007). In a multiphase system with two immiscible fluids, the wettability is referred as the ability of one fluid to adhere to the solid surface when the second fluid is present. The wettability is quantified through the contact or wetting angle, which is the angle between the solid and the fluid adhering to the surface. In an oil/water system, for example, θ_c > 90° indicates an oil wet system; if θ_c > 90° the system is neutrally wet. Intermediate conditions (water wet) are reached if the $0 < \theta_c$ < 90°; θ_c = 0° is observed in total water wet conditions. Contact angle values is variable based on fluid pair, solid material, temperature and pressure conditions. In a CO_2/water/quartz system the contact angle value increases with increasing temperature and pressure (Sarmadivaleh, et al., 2015).

Capillary pressure at the inlet portion of the core can be estimated by injecting 100% of non-wetting fluid at progressively higher flow rates into a core saturated with the wetting fluid (Pini, et al., 2012). The displacement of a wetting fluid by a non-wetting fluid is referred to as the drainage process. Steady state conditions are reached when no change in differential pressure or saturation is registered over time. In this method it is assumed that in steady-state conditions the inlet pressure is equal to the pressure of the non-wetting injected fluid and the outlet pressure corresponds to the pressure of the wetting fluid (no pressure gradient is assumed in water phase) (Figure 2-17).

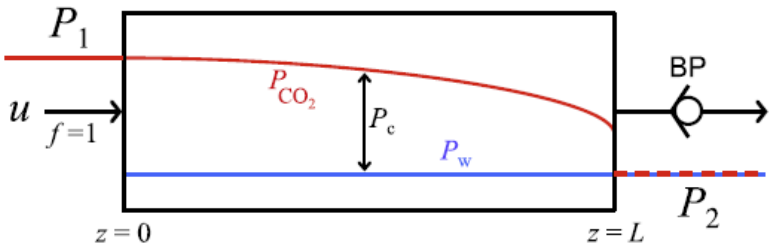

Figure 2-17. CO_2 is injected at a constant flow rate *u* with a fractional flow *f* equal to 1 (100% CO_2 injected). Once steady state conditions are reached, the pressure difference P1 - P2 is equal to the capillary pressure at inlet face. Outlet pressure is imposed by the back pressure pump (BP) (Pini, et al., 2012).

The capillary pressure at the inlet portion of the core ($P_{c_{|x=0}}$) is equal to the change in pressure (ΔP) measured by the pressure transducers placed at the inlet and outlet of the core.

$$P_{c_{|x=0}} = P_1 - P_2 = \Delta P \tag{2-7}$$

Drainage capillary pressure experiments enable estimation of the capillary pressure values at several flow rates. By plotting capillary pressure values against the inlet water saturation, the capillary pressure curve can be fitted with a Brooks-Corey model (Eq. 2-8) (Brooks & Corey, 1964).

$$Pc = Pc_{entry} \cdot Sw_{eff}{}^{1/\lambda} \tag{2-8}$$

$$Sw_{eff} = \left(\frac{Sw - Sw_{ir}}{1 - Sw_{ir}}\right) \tag{2-9}$$

Here Pc is the capillary pressure, Pc_{entry} is the capillary entry pressure, λ is a factor reflecting the pore-size distribution and Sw_{ir} is the irreducible water saturation.

When two fluids are present at the same time in a porous media, the relative permeability of one phase is reduced by the other. The presence of a second fluid reduces the ability of the first fluid to flow. The relative permeability is defined as the ratio between the effective permeability and the absolute permeability. The effective permeability is the permeability of an individual phase, when multiphase fluid flow is taken in account (Glover, 2001). Relative permeability values can be estimated by conducting drainage experiments, injecting the non-wetting fluid at progressively higher fractional flows. Fractional flow is defined as the ratio between the volumetric

flow rate of the non-wetting phase and the total volumetric flow rate imposed (Perrin, et al., 2009). In other words, relative permeability drainage experiments are performed by injecting both wetting and non-wetting fluids at a single total flow rate. For each step, the flow rate of the non-wetting phase is progressively increased, with a consequent decrease in the wetting fluid flow rate in order to keep the total flow rate constant. Relative permeability of the *i* phase for a homogeneous sample is estimated by an extension of the one-dimensional Darcy's law equation for multiphase flow (Krevor, et al., 2012).

$$q_i = -\frac{Akr_i(S_i)}{\mu_i}\frac{\Delta P}{L} \tag{2-10}$$

Here q_i is the volumetric flow rate of the i phase, A is the cross sectional area, k is the absolute permeability, kr_i is the relative permeability of the i phase, μ_i is the dynamic viscosity of i phase, ΔP is the differential pressure across the core and L is the length of the sample. Relative permeability values obtained with core flooding experiments can be fitted with a Brooks-Corey model as follows, (Brooks & Corey, 1964) resulting in characteristic relative permeability curves: .

$$kr_{nw} = (1 - Sw_{eff})^2\left[1 - Sw_{eff}{}^{(2+\lambda)/\lambda}\right] \tag{2-11}$$

$$kr_n = Sw_{eff}{}^{(2+3\lambda)/\lambda} \tag{2-12}$$

Here kr_{nw} and kr_n are the relative permeability values of the non-wetting and wetting phases, respectively. Sw_{eff} and λ are as specified in Equation 2-9 and following sentence.

2.4.3. Sub-core scale influence of small-scale heterogeneities on fluid flow

Several studies have highlighted how small-scale heterogeneities influence fluid flow behaviour. Vasco et al. (2018) and Zahasky and Benson (2018) conducted single phase radiotracer-pulse injection experiments with PET on a Berea sandstone core sample. Despite the rock core appearing to be homogeneous, subtle heterogeneities in porosity and permeability were responsible for variations in the fluid velocity field. High permeability portions of the rock corresponded to low values of the mean arrival time of the radiotracer solution.

In the case of multiphase fluids, in addition to the permeability variation, an important role is played by variations in the capillary entry pressure. Multiple studies have attested that capillary heterogeneities, such as bedding planes, lamination and fractures, influence plume migration, fluid saturation and residual saturation (Krevor, et al., 2011; Hingerl, et al., 2016; Huo & Benson, 2016; Krevor, et al., 2012; Perrin & Benson, 2010; Pini, et al., 2012; Pini & Benson, 2017). Krevor et al. (2011) analysed multiphase flow behaviour and multiphase properties of a Mt. Simon sandstone core sample characterized by finer-grained bedding planes. Drainage and imbibition experiments (100% water flooding after 100% CO_2 flooding) were conducted while medical X-ray CT images were acquired. Results showed that low porosity bedding planes act like capillary barriers, causing a fluid saturation build-up in the host rock region upwards of the bedding planes. Capillary heterogeneities also effectively enhance trapping mechanisms of CO_2 after water flooding (Figure 2-18).

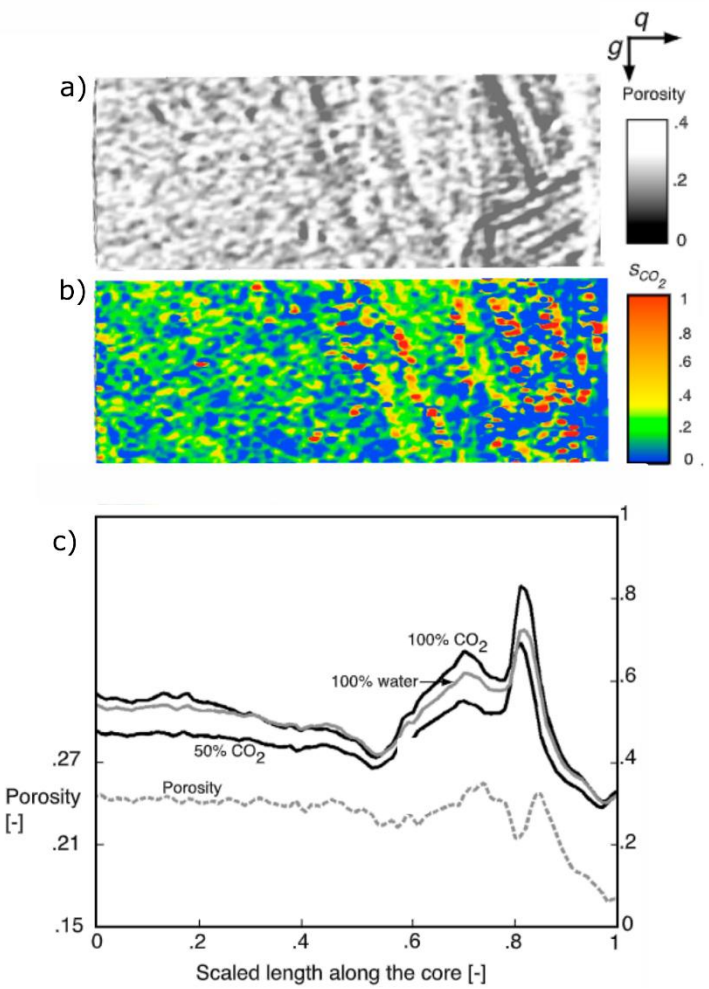

Figure 2-18. a) Porosity distribution of a Mt. Simon sandstone core sample. b) CO_2 saturation distribution at steady state during imbibition. c) Cross-sectional average porosity and CO_2 saturation when 50% CO_2 and 50% water were injected into the fully water-saturated sample, when 100% CO_2 was injected, and when 100% water was injected after 100% CO_2 flooding (Krevor, et al., 2011).

Chapter 3

AUTOMATED HIGH ACCURACY, RAPID BEAM HARDENING CORRECTION IN X-RAY COMPUTED TOMOGRAPHY OF MULTI-MINERAL, HETEROGENEOUS CORE SAMPLES

3.1. Introduction

X-ray computed tomography (X-ray CT) is a modern non-intrusive imaging technique that produces cross-sectional images (slices) of a sample and, using tomography, allows three-dimensional reconstruction of the sample. X- ray CT is widely used in life science, and in the last 30 years, it has completely revolutionized measurement techniques in geoscience. Early X-ray analysis was mostly applied to palaeontology and petroleum engineering (Wellington & Vinegar, 1987). In recent years, thanks to technological progress, and the possibility to reach micrometre resolution, it boasts many more geological applications. For example, it has been used to measure macroscopic soil porosity (Mooney, 2002), pore structure of hydrocarbon reservoir rocks (Van Geet, et al., 2000), and for visualisation of roots in soil (Mooney, et al., 2012). X-ray CT has been integrated into core flooding experiments for understanding how to enhance oil recovery in oil-brine systems (Lager, et al., 2008), and to illuminate trapping mechanisms for carbon storage (Perrin, et al., 2009). Moreover, X-ray CT allows the production of 3D porosity distributions and spatial and temporal measurement of saturation distribution of each phase during multiphase flow experiments. To ensure accurate quantitative results, it is necessary to have high quality images that avoid sources of error, such as artefacts due to the reconstruction process.

A beam of X-rays passes through the sample and radiation is measured by a detection system (detector) to produce attenuation profiles. The attenuation values are

related to the electron densities of the sample's components (Kruth, et al., 2011) and the energy and current values of the scan. All the instruments are characterized by a source-sample-detector system, but in relation to the geometries of the source (point or linear source) and the detector (linear or planar), there are different beam shapes. Cone beam geometry X-ray CT scanners are characterized by a fixed-point X-ray source and a planar detector. The beam is cone shaped and each ray passes through the object with a certain angle. This enables higher resolution images (Lechuga & Weidlich, 2016) but results in a more complicated reconstruction process. In fan beam geometry, instead, the source is a point source and the detector is a curved array. The beam is planar fan shaped and the incident rays are perpendicular to the object. In this case, the reconstruction is fast, but the resolution is low. Artefacts and limitations are mainly related to the operator choices and the reconstruction (Cnudde & Boone, 2013). Such artefacts may affect the accuracy of the measurements of interest. One of the most common artefacts is so-called beam hardening, derived from the incorrect assumption of a monochromatic source, whereas most of the X-ray systems are characterized by polychromatic sources. This assumption is made by the most commonly used and fast method for three-dimensional reconstruction, i.e. Filtered Back Projection (Feldkamp, et al., 1984).

A monochromatic source produces waves with same wavelength. In this case the X-ray is uniformly attenuated when it passes through the sample and the attenuation depends on the X-ray energy and the sample's composition, in accordance with the Beer's Law

$$\boldsymbol{I = I_0\, e^{-\int \mu(s) ds}} \tag{3-1}$$

where I is the X-ray intensity, μ is the attenuation, and s is the ray path (Cnudde & Boone, 2013). A polychromatic source, instead, produces radiations with more than one wavelength; the components of the spectra are not uniformly attenuated, and the lower energies are absorbed more easily by the sample. The consequence of assuming a monochromatic source in the reconstruction process is often higher attenuation values at the sample edges than the centre. This artefact is often termed a cupping effect. Because the measurement of petrophysical properties (i.e. porosity, relative

permeability, capillarity) are strictly related to the quality of the X-ray images, ignoring the beam hardening artefact effects their accuracy.

Different approaches have been proposed to correct the beam hardening artefact, but no solutions that are computationally possible on large datasets, and applicable to all types of materials, have yet been developed. Using physical filters (Jennings, 1988) before scanning often requires higher exposure and it can be time demanding and not economically sustainable. In addition, multiple trials are necessary to define the best filter and the correction of the artefact is not certain. In addition to Filtered Back Projection, several iterative reconstruction (ART, SART, SIRT, MLEM, etc.) methods can be applied on projection data (Gilbert, 1972; Biguri, et al., 2016). However, the computation of these methods on large datasets, such as the 14 GB that results from 3142 projections, is not possible on a standard computer. Most of the pre-reconstruction linearization methods rely on producing a calibration scan using a phantom object with the same density as the sample (Kachelrieß, et al., 2006; Ritschl, et al., 2010). The method cannot be applied if the sample is heterogeneous, multi-material and/or of unknown density. Consequently, these methods are not suitable for correcting scans of geological samples. Linearization can be also determined by pre-determined correction profiles, custom user-specified correction profiles, and custom auto-detected correction profiles (such as those utilized by CT pro 3D, Nikon Metrology). However, in the above methods there are some disadvantages: pre-determined correction profiles always use the same coefficients for linearization of all beam hardening curves and therefore, don't always provide accurate corrections. Custom user-specified correction profiles suffer from a difficulty in determining the optimum coefficients as they are only determined from a single central slice. Some custom auto-detected correction profiles, often implemented in commercial reconstruction software, require a mono-material sample, which is generally not appropriate for geological samples. Ketcham & Hanna (2014) developed an auto-detected correction profile algorithm for heterogeneous geological samples. This method relies instead on defining a region of interest (ROI) characterized by a single material. The ROI is used to infer the density of the material for use in image correction. The method, whilst effective, but may not be applicable in some cases, for example, a clear distinction in density properties may not be possible in low resolution

images or in the case of graduated material properties, such as graded bedding or mineral alteration. Moreover, the method can't be implemented in all reconstruction software and requires expertise in recognizing the scan regions clearly affected by beam hardening. One other post-reconstruction linearization process, is the method proposed by Jovanović et al. (2013), in which the beam hardening correction is simultaneous to segmentation of the images. The procedure is based on the calculation of beam hardening curves for each phase and, as such, it is time demanding. Moreover, it is not applicable to samples in which discrimination between different phases is not possible, for example in materials with a small grain size or in low-resolution scans.

In this study develop a new method for post-reconstruction beam hardening linearization. By considering the limits related to the correction techniques described above, a beam hardening correction method is developed with the following characteristics:

1. is suitable for near-cylindrical geological (multi-mineral) core samples,
2. does not require a priori knowledge of the sample properties,
3. works on samples with a heterogeneous spatial distribution of materials,
4. is applied post-reconstruction, hence works on any X-ray source and scanner configuration,
5. is open source, customizable, and suitable to run on a standard desktop computer.

To this end, an open source ImageJ plug-in was created and it is available to download at https://pureportal.strath.ac.uk/en/datasets/automated-high-accuracy-rapid-beam-hardening-correction-in-x-ray-. Details of the correction methodology employed by the plug-in are provided in a step by step procedure documents available in Appendix 1. The plug-in is validated on a range of natural and artificial geological samples. The implications of beam hardening correction on porosity measurement, multiphase flow measurement and quantitative analysis of geological samples are discussed.

3.2. Materials and equipment

Four samples with cylindrical and quasi-cylindrical shapes and increasing structural complexity have been scanned with micro-CT (μCT) cone-beam scanner (custom Nikon® XT H X-ray CT with 180 and 225 kV sources) in the University of Strathclyde, Advanced Materials Research Laboratory. One of the samples, a Berea Sandstone, has also been scanned with a General Electric Hi-Speed CT/i at the Benson Lab, Stanford University. Scanner settings were chosen to maximise resolution and image quality for each sample scan resulting in the use of different distances from the source and detector, physical filters, values of X-ray energy, current, detector exposure, and even X-ray source unit depending on the sample's physical properties. More details about the settings used for each sample are included Table1.

3.2.1 Plastic rod

A grey Polyvinyl Chloride rod of 40 mm of diameter was scanned to validate the plug-in on homogeneous material.

3.2.2. Loose sand sample

A plastic cylinder was filled with coarse-grained sand pluviated from a constant distance and frequently tapped to ensure uniform packing. The container had an external diameter of 60 mm and an internal diameter of 50 mm.

3.2.3. Deformation band sample

A fine-grained core sample of the Navajo Sandstone Formation was collected at a depth of 59.74 m from a borehole (BH3) in the area of Big Hole Fault, Utah (Shipton, et al., 2002). The core, measuring 60 mm in diameter and 178 mm in length, has 3-4 single anastomosing deformation bands running through the sample. To allow air permeameter tests along the core length, this sample had previously been slabbed creating a 20 to 29 mm wide flat edge (Figure 3-1) hence it was no longer a perfect cylinder when scanned.

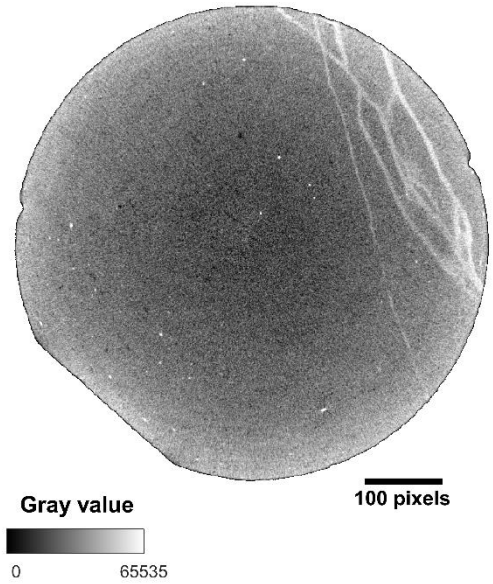

Figure 3-1.Uncorrected slice number 1024 of deformation band core sample. The original core sample had been cut for permeameter tests, and the operation created a flat edge. Pixel size is 100 μm.

3.2.4. Deformation band network core sample

From the same borehole as the first sample a roughly cylindrical Navajo Sandstone core (BH3-1) with length 96 mm and diameter of 60 mm, was collected at a depth of 60.44 m (Shipton et al., 2002). The sample is characterised by a dense network of deformation bands.

3.2.5. Berea sandstone General Electric Hi-Speed CT/i

A homogeneous Berea Sandstone (sample dimensions 100 mm long, 50.8 mm diameter) extracted from the Upper Devonian Berea sandstone formation in Ohio, USA, was scanned with a General Electric medical scanner in both dry (pore space filled with air) and water-saturated conditions and a porosity of approximately 20.6% (Minto, et al., 2017) was previously calculated for the specific sample using the difference between the wet and dry scans in the central core volume unaffected by beam hardening effects. Similar slice-by-slice porosity calculations also showed the porosity to be near-uniform along the core length.

3.2.6. Berea sandstone µCT cone-beam scanner

A highly truncated internal scan of the Berea Sandstone core in section 3.2.5 above was made to have a higher resolution of the upper part of the core, which was unaffected by calcite precipitation (Minto, et al., 2017). A truncated scan is one in which some of the sample lies outside the field of view, hence, sample properties in region surrounding the scan are unknown. Truncated internal scans made with a cone-beam CT do not normally result in a high-quality reconstruction, since they are prone to artefacts caused by X-ray attenuation in the unknown region. This type of artefact presents in a similar manner to beam hardening.

Sample	Distance source object (mm)	Distance object detector (mm)	Energy (kV)	Current	Physical filter	Resolution
Plastic	168.43	505.36	140	86 µA	2 mm Al	49 µm
Loose sand	370.55	688.5	120	196 µA	None	70 µm
Single db	377	377	140	86 µA	0.25 mm Cu	100 µm
Db network	184	867	145	173 µA	1mm Cu	35 µm
Berea medical scan	630	469.31	120	200 mA	None	0.4883 mm
Berea Cone Beam	33.7	640	178	53 µA	1mm Cu	10 µm

Table 1. Table summarizing the settings used and resolutions obtained for each sample scanned.

3.3. Beam hardening correction procedure

In this section, the theory underpinning the proposed beam hardening correction procedure is explained.

3.3.1. Radial profile calculation

The code is suitable for core samples and roughly cylindrical shapes, or for samples contained within a cylindrical core holder or other cylindrical container (for example in the case of the loose material, see 3.2.2.). For images obtained with a cone beam geometry scanner, it is advised to avoid correcting the slices at the very top and very bottom of the sample. These are affected by geometric unsharpness (penumbra) and their attenuation values are not related to the actual composition of the sample, but to geometric factors of the cone beam geometry. The quantity of slices to not consider is variable and depends on the source-object, object-detector distances and the focal spot size (Pauwels, et al., 2014).

As described above, beam hardening in cylindrical shapes produces alteration of the attenuation values in relation to the distance from the centre. Consequently, it seems reasonable to propose a correction based on a radial linearization beam hardening curve.

The beam hardening curve is calculated using the plug-in “Radial Profile Extended” (Carl, 2006). The beam hardening curve, from here on termed the radial profile is a radial average of the attenuation values as a function of the distance from the centre of the sample. The plug-in, in fact, draws concentric circles (usually increasing the radius by 1 pixel) and calculates for each circle the sum of the attenuation or intensity values divided by the number of the pixels included in the circle. In this way, the radial profile is defined for each slice. For computational efficiency, all the radial profile curves obtained (one for each slice once the top and bottom slices affected by penumbra have been removed) are averaged and one single average radial profile (Figure 3-2) is obtained. In this way, the following fitting of beam hardening curve is operated only once. Using a single average radial profile also improves the correction process if there are some heterogeneities in the sample, since it is not much affected by unusually high values, such as those caused by the presence

of deformation bands, bright grains, noise (Figure 3-2), or conversely by low values related to fractures.

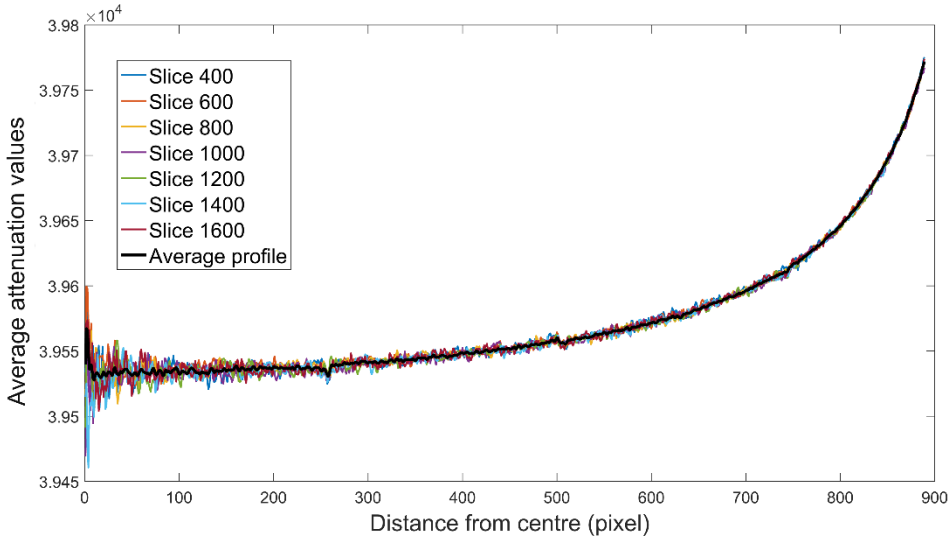

Figure 3-2**.** Radial profile of several slices of the Berea sandstone core sample scanned with cone-beam CT scanner and the average radial profile (black) used for the curve fitting.

3.3.2. Curve fitting

To proceed to the beam hardening correction, the average radial profile is fitted using two equations: an exponential function with offset and an Inverse Rodbard relationship. The first is a single-coefficient exponential model with a vertical offset c,

$$y = ae^{(-bx)} + c \tag{3-2}$$

The second is a four-parameter logistic regression model (4PL):

$$y = c\left(\frac{(x-a)}{(d-x)}\right)^{\frac{1}{b}} \tag{3-3}$$

In equation 3-3, the *a* and *d* coefficient are, respectively, the lower and upper asymptotes. The *b* coefficient represents the steepness of the curve, and the *c* coefficient is the halfway point between *a* and *d*.

Figure 3-3 illustrates the best fit curves for both the Exponential model and the Inverse Rodbard model for the average radial profile in Figure 3-2. The exponential function alone does not provide an accurate correction because it is not able to accurately fit the steep section of the average radial profile close to the edge of the sample (Figure 3-3). The Inverse Rodbard method is well able to fit a steep curve, but when applied to the entire radial profile including the central flat section, it is only possible to achieve a poor fit (Figure 3-3). Achieving a good fit for the last part of the curve, i.e. of the very high attenuation values related to beam hardening, is very important for providing accurate results and is not possible with the exponential model alone. Hence, it was decided to apply the exponential model to the central part of the core and then to fit the Inverse Rodbard only to outer pixels where the curvature is high (Figure 3-4).

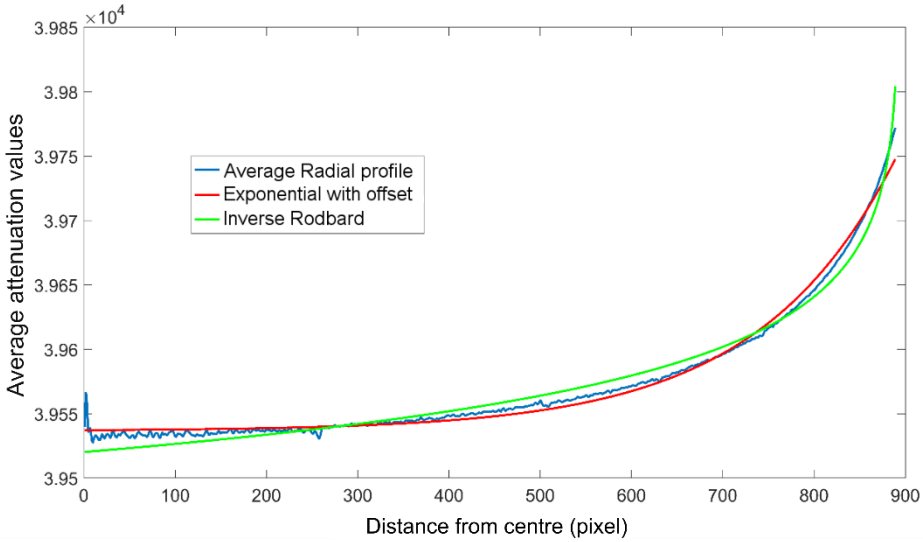

Figure 3-3. Curve fitting on the average radial profile (blue) of several slices of the Berea sandstone core sample with both Exponential with offset function (red) and Inversion Rodbard function (green).

The curvature of each function is related to the maximum and minimum values of each of the two fitted sections. Hence, to obtain a good fit it is important to define the boundary between the two regions, termed the cut-off point (COP, Figure 3-4).

Sensitivity tests were made to determine the best value for the COP that minimised errors in the fit. This resulted in the COP being defined by

$$COP \approx \left(\frac{(max - m_{10})}{100} * 25\right) + m_{10} \tag{3-4}$$

where m_{10} is the mean value of the first 10% of the curve, to remove noise at the centre of the image, and *max* is the maximum value of the average radial profile.

A small overlapping window is set during fitting to ensure a smooth transition from one function to the next at the cut-off point (i.e. to remove any kink). The window starts from the COP (Figure 3-4) and its width is 1% of the entire radius, with a minimum size of 5 pixels. In this window, the average radial profile is fitted with both the Rodbard and Exponential equations. A correction coefficient is then calculated, subtracting the average of the points calculated in the window with the Rodbard equation to the average of the points calculated in the window with Exponential equation.

$$\mathrm{f} = \mathrm{av}_{\mathrm{Exp,w}} - \mathrm{av}_{\mathrm{Rod,w}} \tag{3-5}$$

This correction coefficient is implemented as an additional factor when the outer portion of the core sample is corrected using the Rodbard equation. So, Equation 3-3 becomes,

$$\mathrm{y} = \left(\mathrm{c}\left(\frac{(\mathrm{x}-\mathrm{a})}{(\mathrm{d}-\mathrm{x})}\right)^{\frac{1}{\mathrm{b}}}\right) + \mathrm{f} \tag{3-6}$$

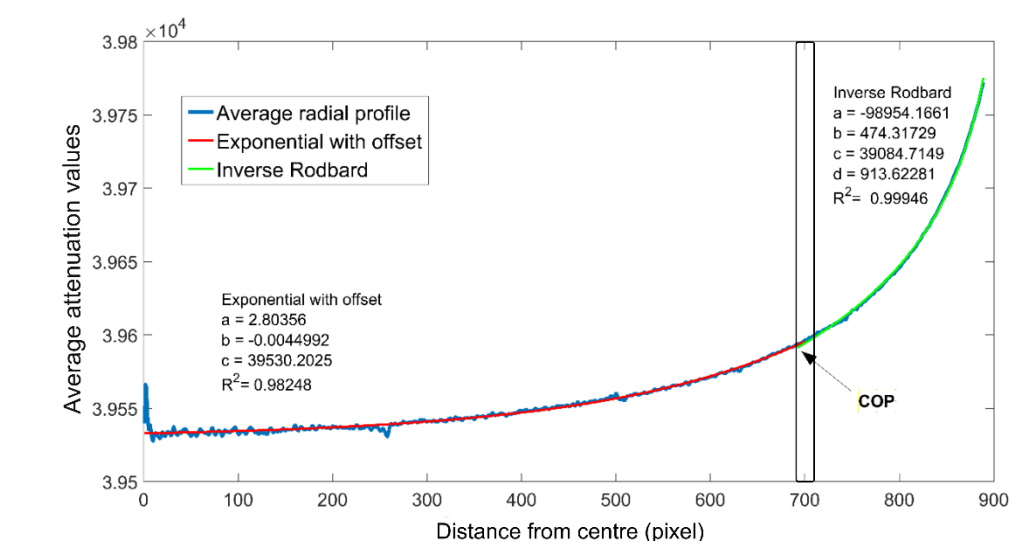

Figure 3-4. The average radial profile of Berea sandstone core sample is split in two for the curve fitting with Exponential with Offset in the central part and with Inverse Rodbard in the outer part. The black box is referred to as the overlapping window

To facilitate the curve fitting and reduce the number of iterations taken to find a reasonable solution for the fitting of the *Inverse Rodbard*, it is desirable to define initial guesses for the *a*, *b*, *c*, and *d* coefficients in the equation. This ensures that the iterative fitting procedure converges. Considering that the *a* coefficient is the lower asymptote and usually has negative values, its initial guess is set as 0. The *d* coefficient is the point at which the curve reaches its maximum value; for this reason, an initial guess equal to the radius is used. For investigating the behaviour of the *b* and *c* coefficients, the fitted values for samples 3.2.1., 3.2.2., 3.2.3., 3.2.4., and 3.2.6., plus two scans made with different X-ray calibration settings for both the plastic rod and for sample 3.2.5 (Figure 3-5). The *b* and *c* coefficients follow respectively a Power law (Figure 3-5a),

$$b = 278245\, x^{(-1.218)} \tag{3-7}$$

and an exponential law (Figure 3-5b)

$$c = 38641\, \mathrm{e}^{(-0.0003x)} \tag{3-8}$$

where *x* is the log to base 10 of the difference between the maximum and minimum values of the section of the radial profile fitted by the Inverse Rodbard function.

For heterogeneous samples (loose sand and multiple deformation bands samples) the *b* coefficient covers several orders of magnitude for the same range on the x-axis (Figure 3-5a). For these samples, using the full range of values on Figure 3-5a for the initial guess resulted in the same solution. The initial guess for the value of *c* can be better constrained (Figure 3-5b). For both the *b* and *c* coefficients, changes to the calibration of the X-ray CT scanner led to significantly different fitted values (old scans on Figure 3-5).

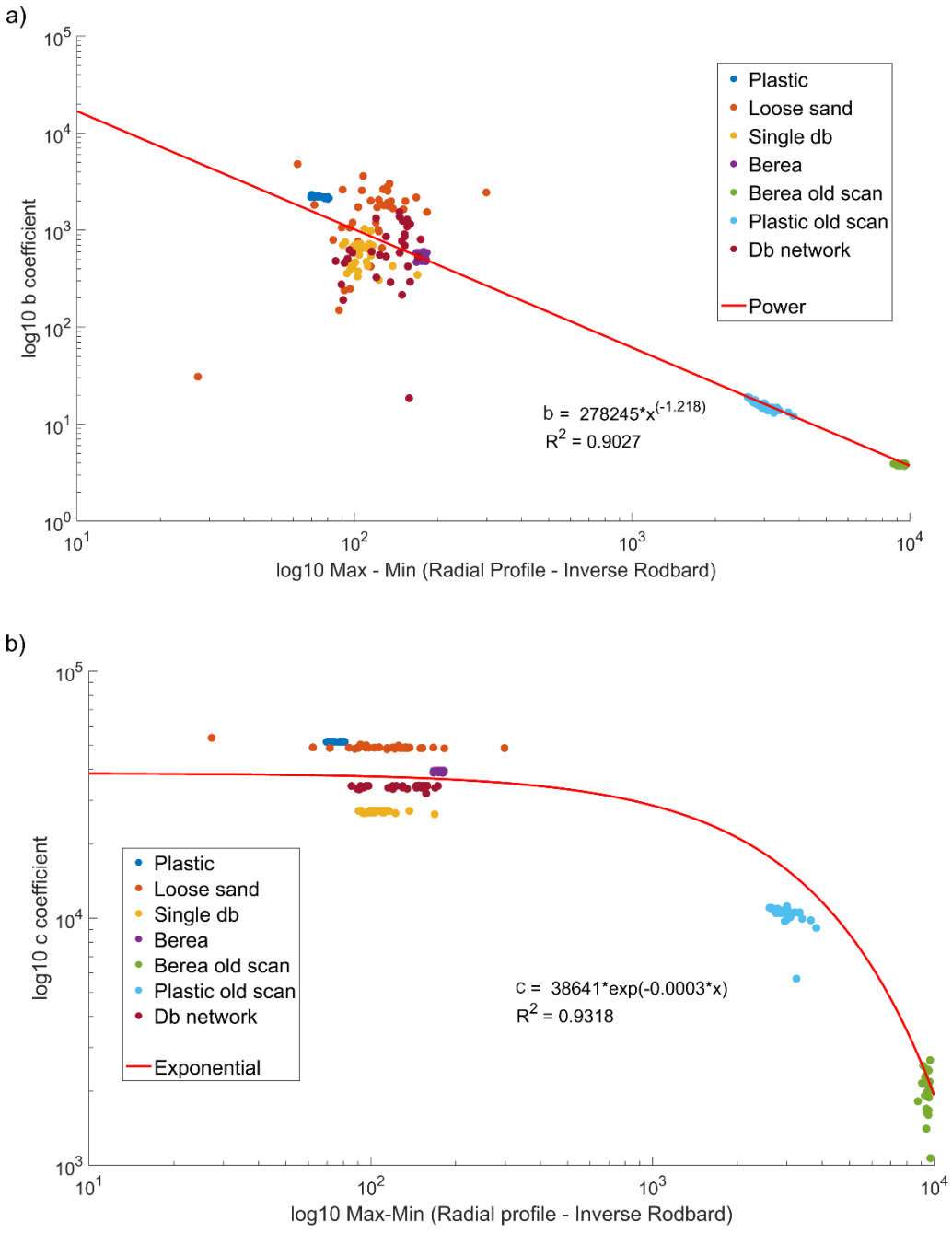

Figure 3-5. a) b coefficient values vs the log difference between the maximum and minimum value of the Radial profile fitted by the inverse Rodbard equation. It follows a power law. b) c coefficient values vs the log difference between the maximum and minimum value of the Radial profile fitted by the inverse Rodbard equation. The red line is a best fit Exponential function.

Once the initial guesses have been defined, it is possible to fit the average profile and, using the calculated coefficients for each equation, *Exponential with offset* and *Inverse Rodbard*, to correct each pixel of the image.

3.4. Results

The plug-in was applied to all the samples described in section 3.2. In each case, the beam hardening artefact was significantly reduced, and the method did not produce any over-correction or blurring of the image.

3.4.1. Homogeneous sample

In this section the results for the plastic rod (Figure 3-6 a,b,c) and the loose sand material sample (Figure 3-6 d,e,f) are shown. The plastic rod was used for testing the reliability of the plug-in and to show that beam hardening occurs in a homogeneous, uniform material. Whereas, the loose sand sample whilst still being a homogeneous sample, contains multi-mineral components. Visual analysis of Figure 3-6 shows that an excellent correction has been achieved in each case.

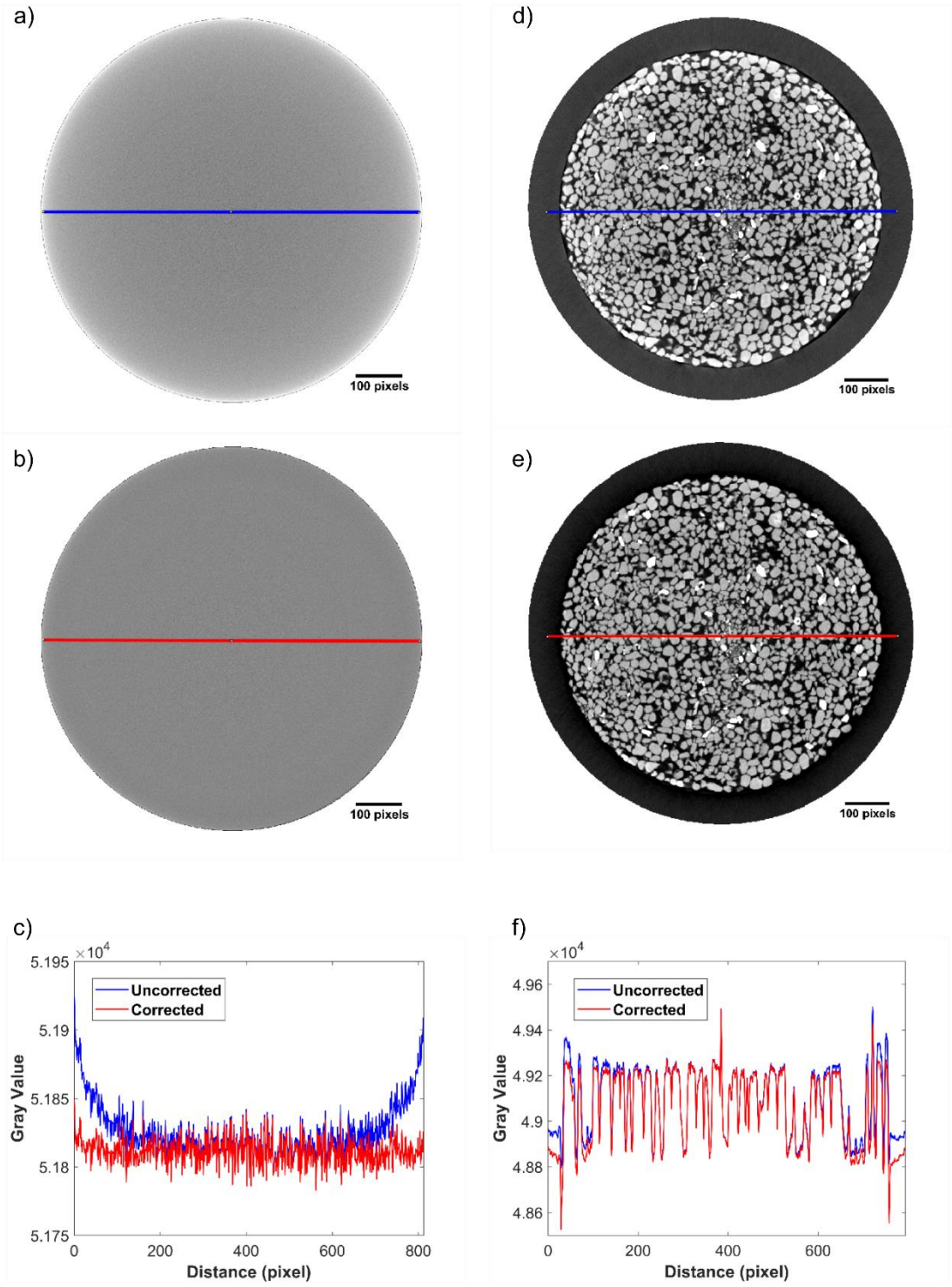

Figure 3-6. a) Slice number 1567 of Plastic rod uncorrected; b) slice number 1567 of Plastic rod uncorrected corrected with the plug-in proposed; c) plot of attenuation values along the selections of the uncorrected (blue) and corrected image (red); pixel size is 49 µm. d) Slice number 1299 of Loose sand with outer ring sample uncorrected; e) slice number 1299 of Loose sand with outer ring sample corrected with the plug-in

proposed; f) plot of attenuation values along the selections of the uncorrected (blue) and corrected image (red). Pixel size is 70 μm.

3.4.2. Non-uniform shapes and heterogeneous samples

Figure 3-7 shows results of the correction applied to the deformation band core sample and the deformation band network core sample. Both have near-cylindrical shapes and contain structural heterogeneities in the form of deformation bands and/or fractures.

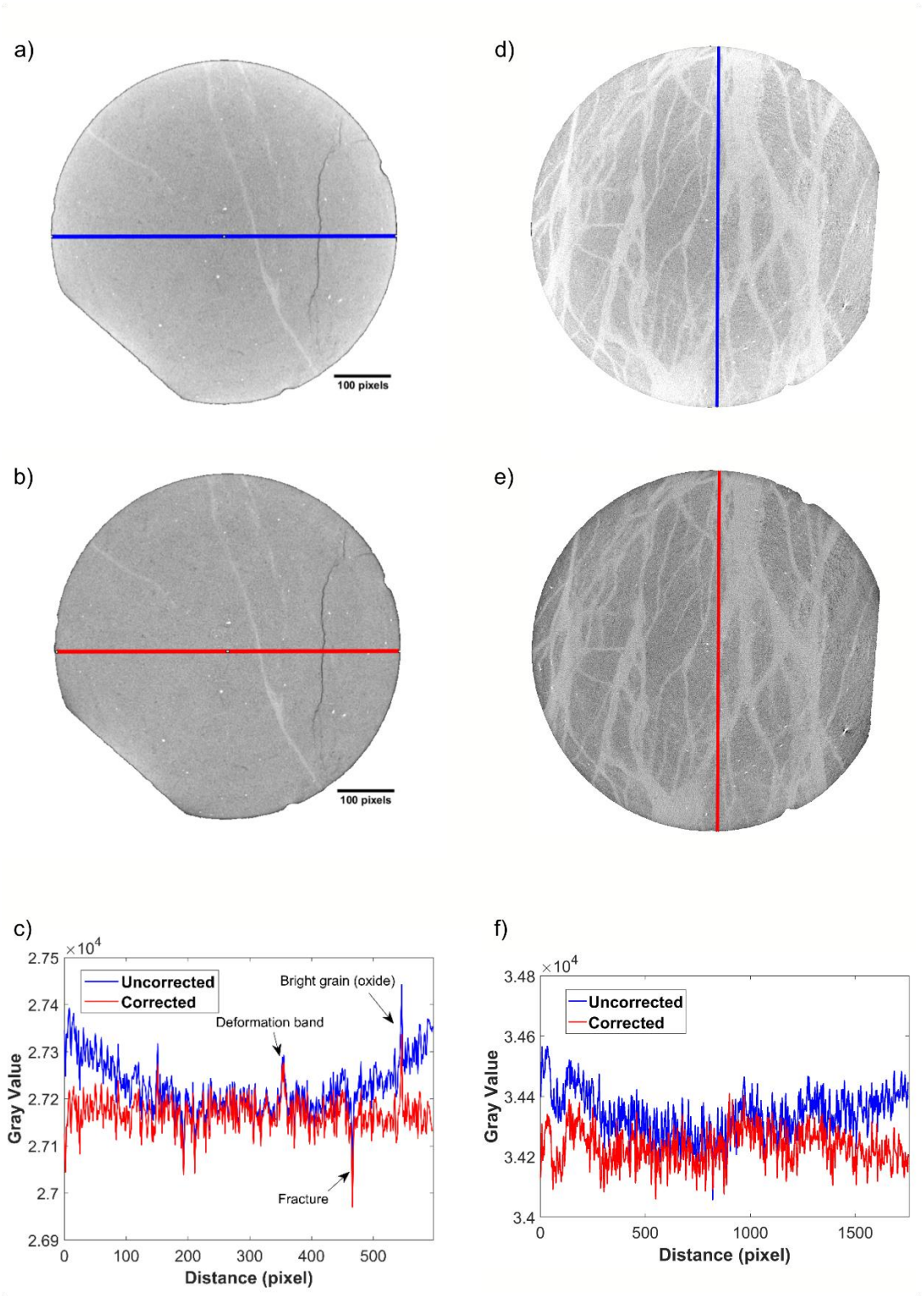

Figure 3-7. a) Slice number 1660 of sand sample uncorrected; b) slice number 1660 of sandstone with deformation bands core sample corrected with the plug-in proposed c) plot of attenuation values along the selections of the uncorrected (blue) and corrected image (red). In both profiles is possible to distinguish a positive spike related to the deformation band, a negative spike related to the fracture and another positive one due

to the presence of oxides in the rock. Pixel size is 100 μm. d) Slice number 1029 of multiple deformation bands core sample uncorrected; e) slice number 1029 of multiple deformation bands core sample corrected with the plug-in proposed; f) plot of attenuation values along the selections of the uncorrected (blue) and corrected image (red). Pixel size is 35 μm.

For cores containing a slabbed edge, a second artefact, in addition to beam hardening is present. This artefact is termed the exponential edge-gradient effect (EEGE) (Joseph & Spital, 1981) and is a non-linear effect arising from the intersection of X-ray paths at corners, which is not accounted for in filtered back-projection algorithms. Its effect results in a lowering of the attenuation values at corners (Ketcham & Hanna, 2014) (Figure 3-8a). For this reason, the correction was not able to fully correct the beam hardening close to the slabbed edge (Figure 3-8b) and it is advised to avoid quantitative measurements in this region.

It is worth noting here that a very similar issue will occur to that of the slabbing in the case of a core that contains a discrete contact between two materials with very different densities e.g. where a sedimentary contact between two very different strata runs along the length of the core. In this case, the beam hardening curve calculated will be an average of the two materials. Hence, the individual rock types in the image will not be accurately corrected. In this case, it is suggested to threshold the image and isolate the two portions of the cores, then apply separately the correction provided in this study.

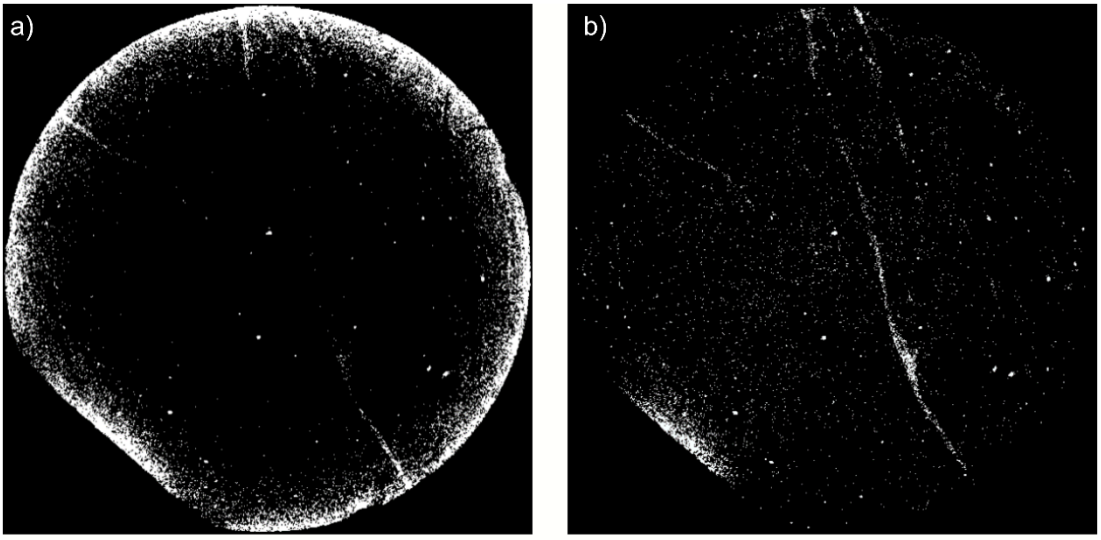

Figure 3-8. a) Global segmentation (Auto Treshold in ImageJ) of the uncorrected image of the sandstone with deformation bands core sample (as shown in Figure 3-7a). The beam hardening artefact is not a radial function for non-cylindrical shapes. Lower attenuation values occur at the corner due to EEGE. b) Segmentation of the corrected image of the sandstone with deformation bands core sample (as shown in Figure 3-7b). The combined EEGE/beam hardening artefact is not corrected along the flat portion.

For the deformation band network sample, segmented images clearly show the beam hardening artefact. Without the correction it is not possible to define the complete pattern of the deformation bands (Figure 3-9a) since segmenting the portion of the deformation bands close to the edge means that the central part of the bands disappears. With the correction applied, Figure 3-9b, the band network is clearly visible.

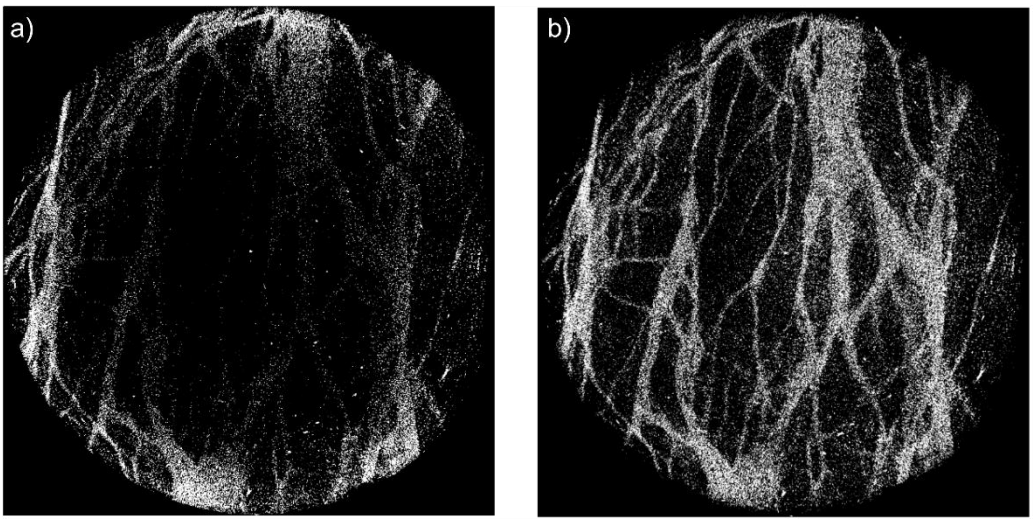

Figure 3-9.a) Global segmentation (Auto Treshold in ImageJ) of the uncorrected image of multiple deformation bands core sample (as shown in Figure 3-7d). Without correction it is not possible to identify completely the deformation bands. b) Segmentation of the corrected image of multiple deformation bands (as shown in Figure 3-7e). All the deformation bands are shown.

3.4.3. Berea sandstone core sample with the medical scan

The correction plug-in is also applied to the medically scanned Berea sandstone sample (section 3.2.5). The sample was scanned inside a high pressure core holder at dry and water-saturated conditions and both datasets were corrected for the beam hardening artefact. Figure 3-10 shows the water-saturated scan and how the code can also remove the beam hardening effect in this lower resolution medical CT scanner dataset. For this specific case, before applying the correction, it was cropped out the

core holder and a minimal portion of the outer part of the core itself, where the partial volume effect resulted in a ring of pixels in which attenuation was part core, part steel core holder (which has extremely high attenuation values). Using such pixels would produce a beam hardening curve that is steeper and not truly representative of the core sample, which will then, in turn, not be properly corrected.

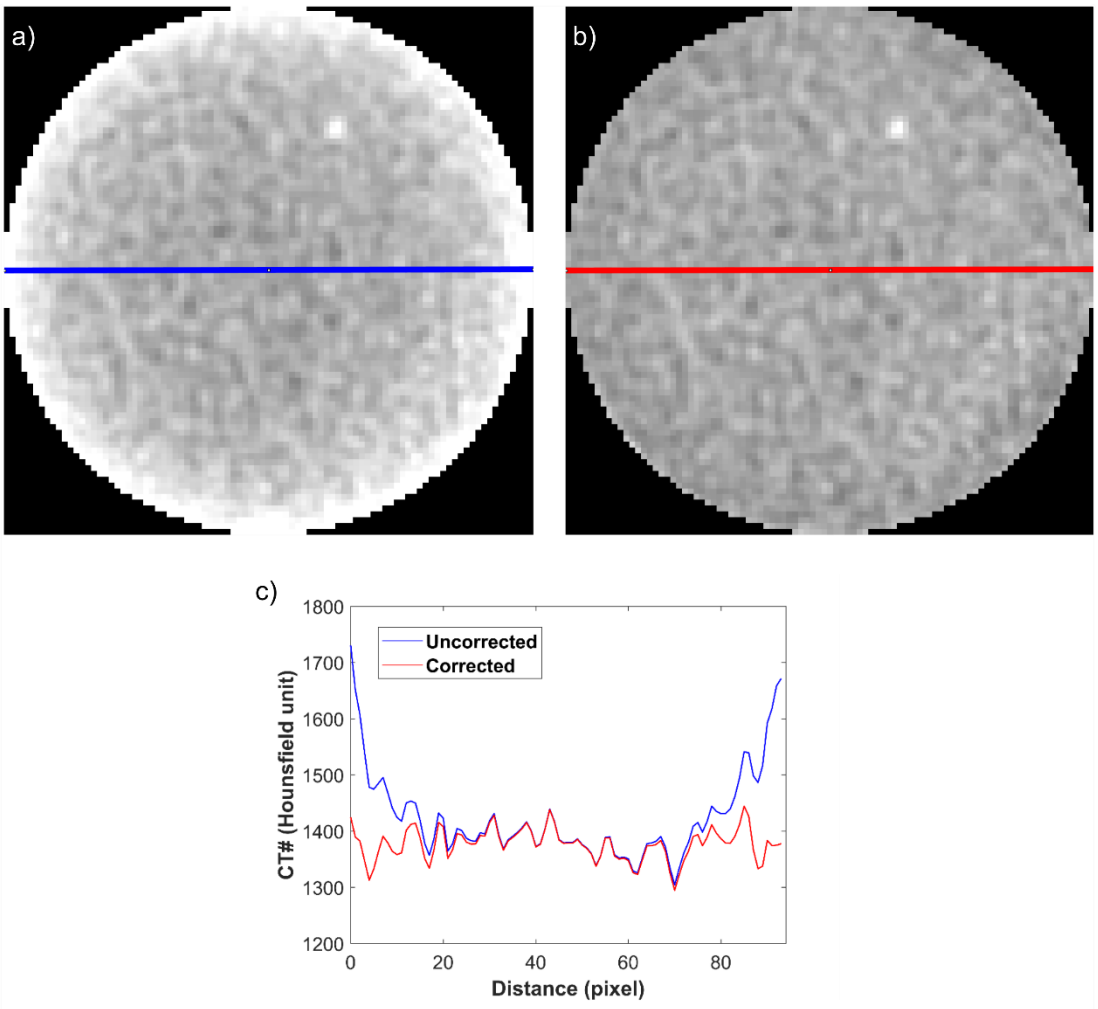

Figure 3-10. a) Slice number 59 of water-saturated Berea sandstone core sample uncorrected. This dataset has been acquired with a medical scan; b) slice number 59 of Berea sandstone core sample corrected with the plug-in; c) plot of attenuation values along the selections of the uncorrected (blue) and corrected image (red). Pixel size is 0.4883 mm.

3.4.4. Berea sandstone core sample internal scan with cone-beam CT

Finally, Figure 3-11 shows the results of the beam hardening correction plug-in applied to the truncated scan of the Berea Sandstone core sample (section 3.2.6).

Once again, the correction is very successful, and the scan artefacts have been removed.

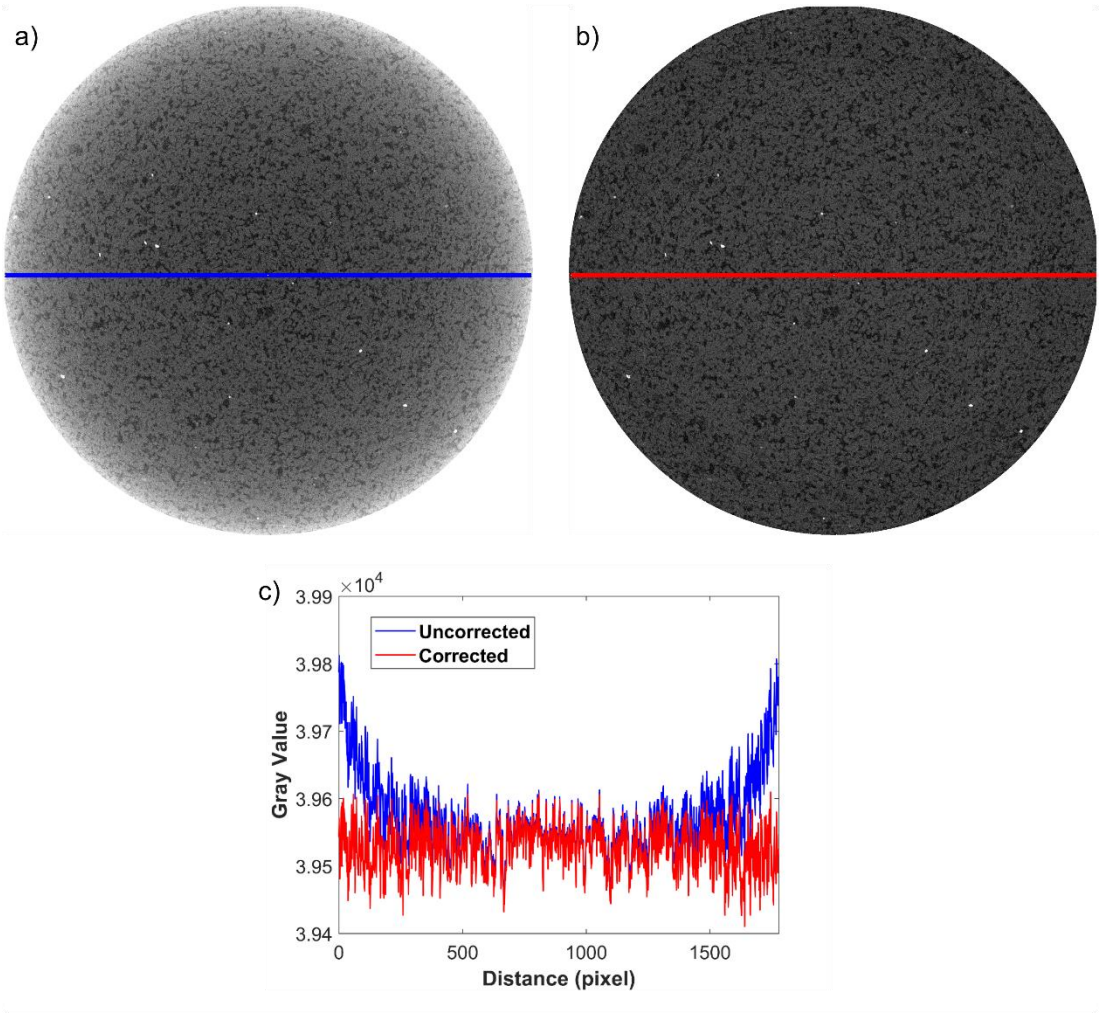

Figure 3-11. a) Slice number 690 of Berea sandstone core sample uncorrected; b) slice number 690 of Berea sandstone core sample corrected with the plug-in; c) plot of attenuation values along the selections of the uncorrected (blue) and corrected image (red). Pixel size is 10 μm.

3.5. Determination of core scale petrophysical properties

3.5.1. Determination of core scale porosity

Determination of porosity through X-ray CT can be achieved following two main methods. The first one requires one single scan with enough resolution to

distinguish void and solid phases. The second method instead consists of using two sets of scan images, one in which the sample is dry and the other in which the sample is fully saturated with water.

3.5.1.1. Segmentation-based method

The segmentation-based method for porosity calculation is common, since it only requires a single scan and, therefore, conserves both time and money. To use the method, there needs to be reference features larger than the image resolution and free from any partial volume effect and blurring. When the resolution does not meet this criteria, additional image techniques (not tested here) can be employed for enhancing the edges and boundaries between different materials (Hanna & Ketcham, 2017). To check the improvement provided by the beam hardening correction plug-in porosity calculation using segmentation, the internal scan of the Berea sandstone core sample is considered. An internal scan is used, since for this method, it is required an extremely high-resolution image. Using a single slice, 2D images of porosity were created using a standard thresholding approach to convert the grey scaled image into a binary image (i.e. pore/not pore). The threshold values are selected such that voids and grains have values of 1 and 0 respectively. Finally, porosity is obtained by calculating the proportion of pixels valued at 1 or 0 in the shape described by the sample.

Results derived using the plug in are compared with those taken straight from the auto-detected correction software supplied with the instrument, CT pro 3D. Even when the *strong* correction is used, it was not able to remove the cupping effect. As explained in the section 3.1, in the CT pro 3D software it is possible to customize the correction profiles and choose different coefficients to those proposed in the *strong* correction, although there is no methodology for their selection. For the uncorrected sample, a porosity of 7.23% is obtained (Figure 3-12a); the porosity calculated for the slice using the *strong* correction option in the Nikon software is 14.24% (Figure 3-12b); and the porosity calculated with the new beam hardening correction is 20.54% (Figure 3-12c). This last porosity is consistent with published values for Berea sandstone and with the value of 20.6% derived for the core in Minto et al. (2017).

Petroleum reservoirs are mostly sandstones, underestimates in porosity of ~13% with no correction and ~6% using the commercially supplied software, would be highly significant and would lead to incorrect assessments of reservoir quality. In fact, 7.23% porosity is outside the usual range for a homogeneous sandstone and even a difference in porosity estimate from 20.5% to 14.24% would result in a downgrading of reservoir quality from good to fair. It is clear the correction plug-in has a significant effect on the estimate of porosity, so it is important to determine accuracy of these porosity estimates.

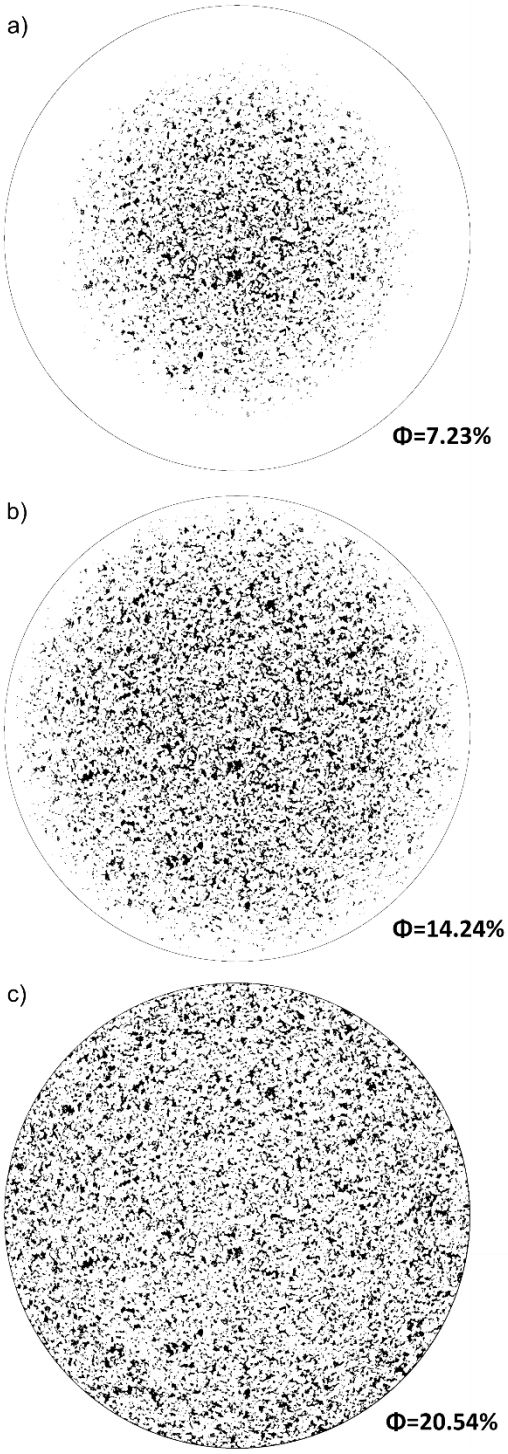

Figure 3-12. a) Image thresholding of slice 690 of Berea sandstone core sample uncorrected: calculated porosity is equal to 7.23%; b) Image thresholding of slice 690 of Berea sandstone core sample with strong correction of Nikon software: calculated porosity is equal to 14.24%; c) Image thresholding of slice 690 of Berea sandstone core sample with beam hardening correction: calculated porosity is equal to 20.54%.

3.5.1.2. Saturated and dry scans method

The saturated and dry scan method for determining porosity is commonly more accurate than the single-scan method, since it uses the 'difference' between the wet and dry scans. As a consequence, if the errors incurred during reconstruction are the same in the wet and dry images, then taking one image form the other removes them. Using this method, the porosity is calculated by (Krevor, et al., 2012)

$$\Phi = \frac{CT_{watersaturated} - CT_{dry}}{I_{water} - I_{air}} \tag{3-9}$$

where the denominator is defined as the difference between the Hounsfield units of the air (-1000) and the water (0). The method also has the advantage that it can be used on low resolution scan images, in which each voxel contains both pores and grains and a clear interface between only two materials is not possible/

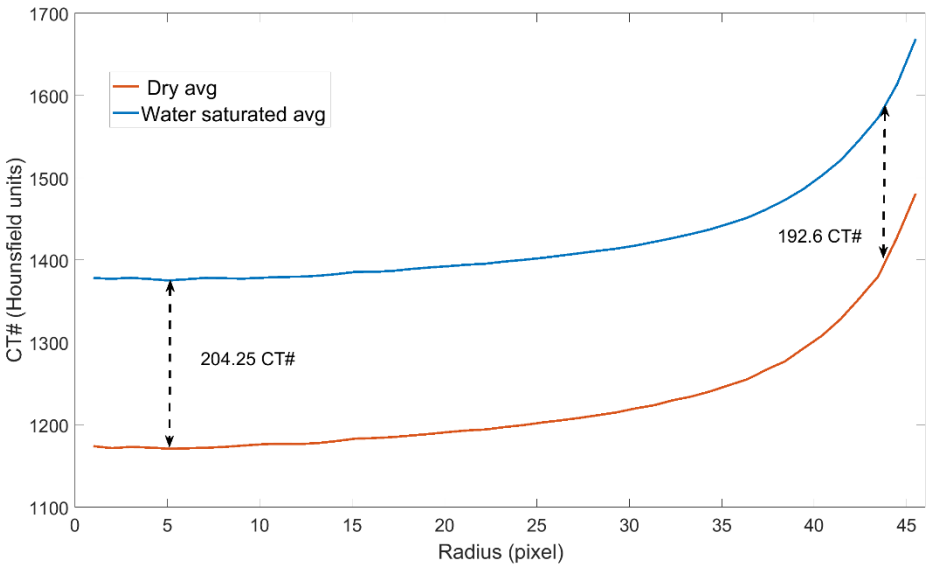

Figure 3-13. Difference between beam hardening curves of the water-saturated and dry datasets. Each curve has been obtained by averaging all the slices of the corresponding dataset and calculating the radial profile.

The wet and dry method was used to obtain a porosity estimate for the Berea sandstone core, acquired with the medical scanner (an internal cylindrical high-resolution scan of the same core was used for the single scan method above). Figure 3-13 shows radial profiles for the dry and water-saturated images, both of which are clearly affected by beam hardening. From visual analysis, whilst the beam hardening

effect in the two scans is similar, they have slightly different curve shapes. This difference in curve shape means that the beam hardening effect does not entirely disappear when subtracting the two datasets. As a result, the uncorrected porosity estimate is characterized by a decrease in porosity toward the radial edge of the slice (Figure 3-14). Since Berea sandstone is known to be very homogeneous, this trend can be attributed to the different shapes of the beam hardening curves.

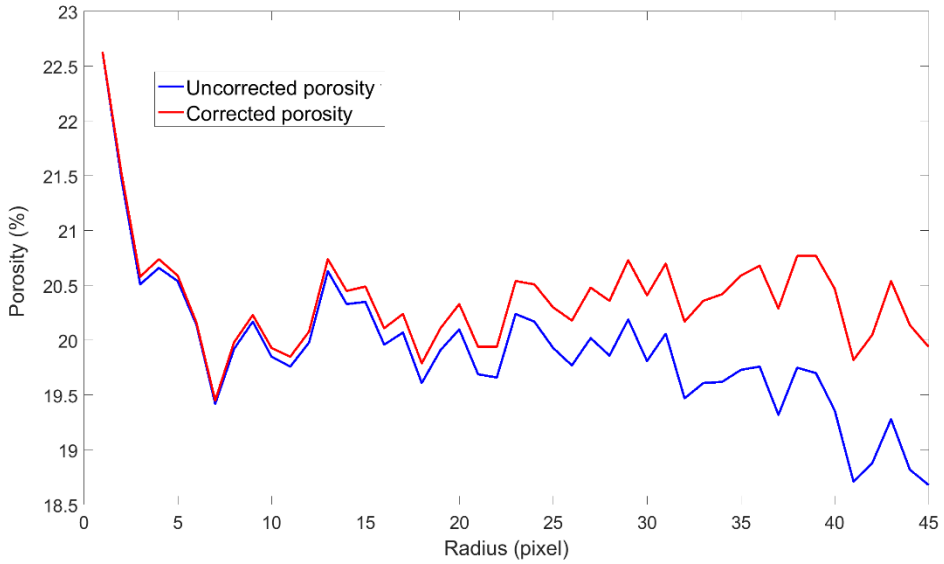

Figure 3-14. Radial profile of both uncorrected and corrected porosity of slice 59. The uncorrected porosity decreases along the edges of the sample.

Both images, dry and water-saturated, were corrected with the proposed plug-in and the porosity was then re-calculated. The core average total porosity was calculated in each case, resulting in values of 20.5% and 19.82% for the corrected and uncorrected images respectively (Figure 3-15). The uncertainty in porosity, based on the uncertainty associated with the CT number at voxel level, for both measurements is ±1.36% (of the calculated total porosity) using the method proposed by Pini et al., (2012). Both measurements are similar to the 20.6% porosity calculated in Minto et al. (2017). However, it is clear from the Figure 3-14, that the two porosity trends are divergent at the end of the sample: the porosity calculated using uncorrected datasets decreases at the edge of the core, which is not justified by any specific compositional of structural feature. Considering that this trend is present in all the slices of the core, the average slice porosity of the uncorrected dataset is lower than the corrected one.

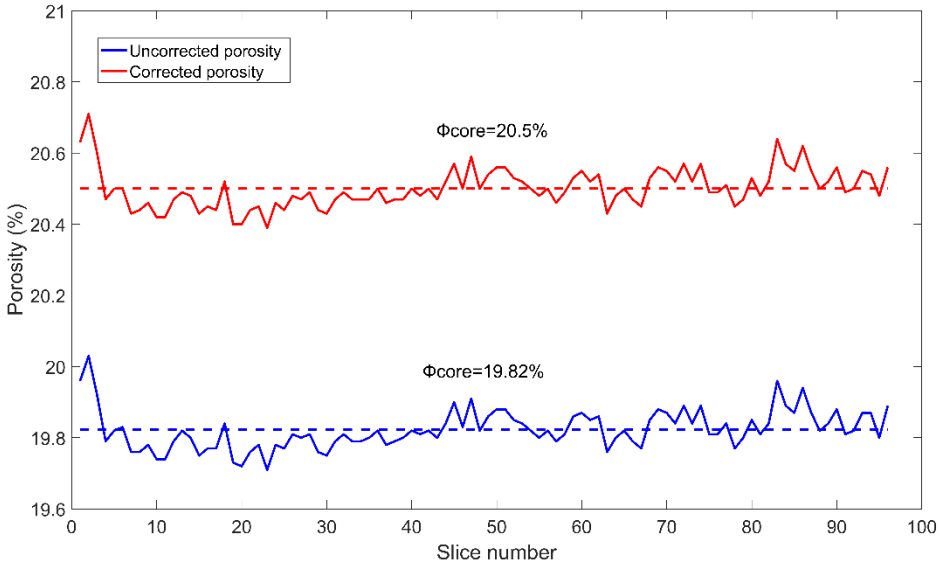

Figure 3-15. Average of uncorrected and corrected porosity for each slice (solid line) and the uncorrected and corrected core average porosity (dashed line).

3.5.2. Determination of core scale permeability

Using CT data, pore-scale flow modelling can be used as a method of estimating the core-scale permeability (~ 200 md for host rock, ~ 1 md for deformation bands). For example, using the CT scan for the multiple deformation band core (Figure 3-16, left), each voxel is defined as either host rock or deformation band (Figure 3-16, middle). The Navier-Stokes equations, with added Darcy-Brinkman losses due to porous resistance (Minto, et al., 2018), can then be solved numerically to simulate 3D flow paths within the core (Figure 3-16, right). The modelled pressure drop across the core for a simulation with a constant flow rate, can be used to calculate the core-average permeability.

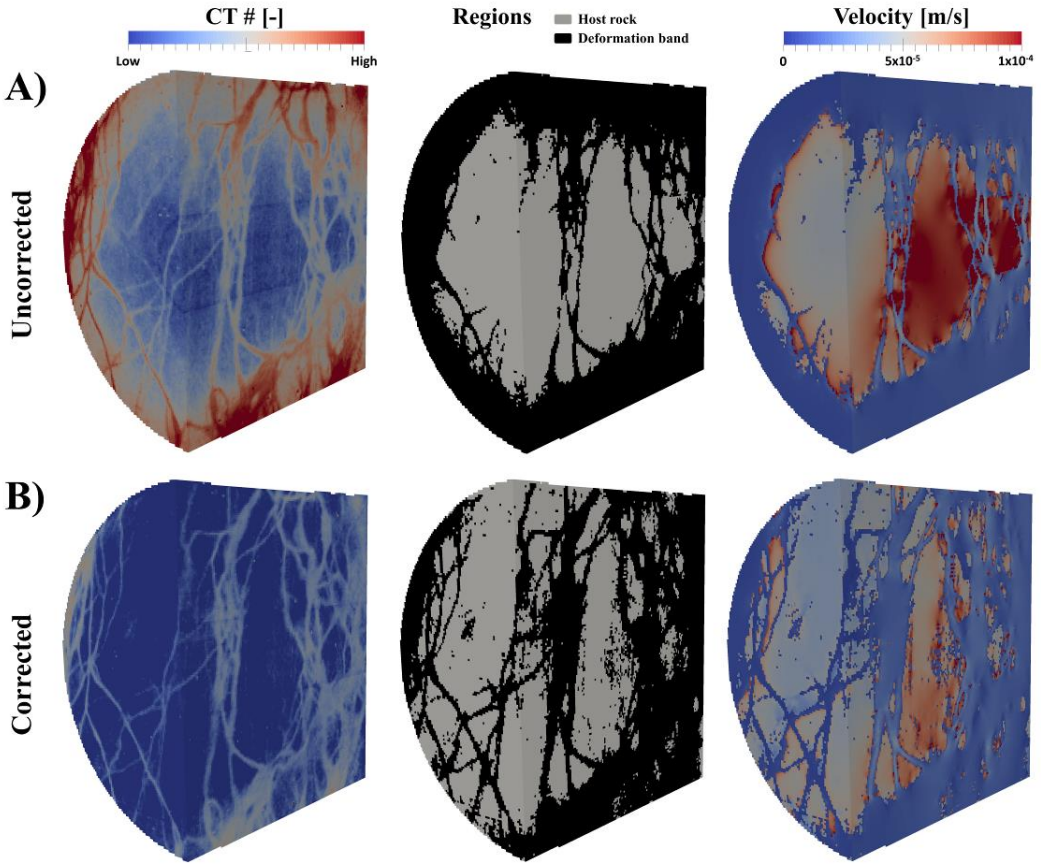

Figure 3-16. From left to right: X-ray attenuation value, binary segmented image, and calculated velocity distribution for A) the original uncorrected scan data and B) the same scan data after beam hardening correction. Core average permeability was calculated as 12.2 md for the uncorrected data and 6.47 md for the corrected model. Cores cut in half to visualise internal properties.

In the uncorrected dataset (Figure 3-16A), the deformation bands are underrepresented in the centre of the core and overrepresented at the edges. This creates an unrealistically high permeability central channel, through which most of the flow is focused, and leads to a bulk permeability estimate of 12.2 md. Whereas, in the corrected dataset, the deformation bands are well represented throughout the core, resulting in a more uniform flow distribution and a bulk permeability estimate of 6.47 md. The error in the spatial representation of deformation bands in the uncorrected core will also have implications for estimates of other petrophysical properties, in particular relative permeability and capillary entry values, both of which are key to understanding reservoir performance for CO_2 enhanced oil recovery, CO_2 trapping and long-term CO_2 storage.

3.6. Conclusion

In this study, a new technique is presented for beam hardening correction. The method is completely automatic and independent of the sample material, the material heterogeneity, scanner resolution, and the scanner settings. The method is presented through development of an open source plug-in running on ImageJ. The correction has been applied on both homogeneous and heterogeneous cylindrical and near-cylindrical geological samples and provides excellent results in all cases. The application of the correction leads to significant differences in the estimates of porosity and permeability. Further, unlike other beam hardening correction methods, the proposed plug-in can be used to correct for cupping errors in truncated internal scans. This is highly valuable, since truncated scans provide small volume, high-resolution data, without the need for sample destruction.

Chapter 4

SUB-CORE SCALE FLUID FLOW BEHAVIOR IN A SANDSTONE WITH CATACLASTIC DEFORMATION BANDS

4.1. Introduction

Sandstones are one of the most high quality and high storage volume candidate geological formations for gas storage due to their global distribution, and high porosity and permeability (Benson & Cook, 2005; Bjørlykke & Jahren, 2010). Key to realizing their potential will be an accurate assessment of their reservoir-scale petrophysical properties and multiphase flow characteristics. These properties govern the behaviour of multiphase fluids within the rock and hence will determine the efficiency of injection projects such as carbon dioxide storage, hydrogen storage, and enhanced oil recovery schemes.

Together with field observations, laboratory core flooding experiments are a valuable tool for determining petrophysical properties and multiphase flow characteristics under reservoir conditions. Integrating experiments with advanced imaging techniques, such as X-ray computed tomography (CT) and positron emission tomography (PET), enables measurement of single and multiphase flow properties from the pore-scale to the centimetre-scale. In X-ray CT, an X-ray beam is generated, and attenuation values are determined based on the electron density of materials within the sample (Kruth, et al., 2011). This allows the spatial distribution of fluids with differing densities to be determined (Akin & Kovscek, 2003). Both medical CT and micro-CT are commonly used in Earth science. Medical CT is able scan centimetre-scale samples in minutes with millimetre resolution while micro-CT provides micrometre-scale images with scans that take several hours. PET imaging, by contrast, relies on the detection of photons from positron-emitting radiotracers that are injected into the rock. Detection of the photons enables time-resolved quantification of

radiotracer migration through the sample. Thus with PET imaging it is possible to quantify fluid transport behaviour, while CT provides high-resolution information about rock structure and fluid saturation distribution (Pini, et al., 2012; Zahasky, et al., 2019).

Imaging and analysis of core flooding experiments enables quantification of rock and fluid properties, such as porosity and absolute permeability (Krause, et al., 2013; Ochi & Vernoux, 1998; Perrin, et al., 2009; Zahasky & Benson, 2018), fluid saturation, capillary pressure and relative permeability (Akbarabadi & Piri, 2013; Krevor, et al., 2012; Pini, et al., 2012; Ruprecht, et al., 2014; Vinegar & Wellington, 1987). Many of these studies indicated that sandstones are characterized by subtle small-scale heterogeneities that actively affect fluid flow. Variations in porosity and permeability affect the fluid velocity field, with high velocities being associated with regions of high porosity and permeability (Bloomfield, et al., 2001; Grathwohl & Kleineidam, 1995; Vasco, et al., 2018; Zahasky & Benson, 2018) and for multiphase fluid flow, variations in capillary pressure and relative permeability affect plume migration and residual saturation at both the pore and the field scale (Hingerl, et al., 2016; Krevor, et al., 2012; Krevor, et al., 2015; Li & Benson, 2015; Perrin & Benson, 2010; Pini & Benson, 2017; Saadatpoor, et al., 2010). In particular, Krevor et al. (2011) reported that regions presenting high capillary entry pressures (i.e. small pore throats) act as capillary barriers for the non-wetting fluid, leading to an increase in saturation of the latter in the preceding pores.

Until now, sub-core scale flow and transport behaviour in heterogeneous porous media has focused on sandstones characterized by the presence of bedding planes, laminae and/or fractures (Corey & Rathjens, 1956; Hingerl, et al., 2016; Kim, et al., 2018; Krevor, et al., 2011; Li, et al., 2019; Manzocchi, et al., 2002; Medina, et al., 2011; Pasala, et al., 2013; Shipton, et al., 2002; Tueckmantel, et al., 2012). Relatively little attention has been given to experimentally understanding the impact of deformation bands on fluid flow. Deformation bands are low porosity bands that form in response to shear and they are extremely common in sandstones with a porosity greater than 0.15 (Aydin, 1978; Fossen, et al., 2007; Schultz & Siddharthan, 2005). Several types of deformation bands can be defined based on their kinematic

mechanisms. The most common are compactional shear or cataclastic bands (Aydin, et al., 2006). These form by a combination of shear and compaction mechanisms and are always characterized by cataclasis. Cataclastic bands are millimetres-thick tabular structures (Aydin, 1978; Aydin & Johnson , 1978), along which grain rolling and grain fracturing lead to a reduced porosity and permeability. Multiple studies have reported that deformation bands are several orders of magnitude less permeable than the host rocks in which they form (Antonellini & Aydin, 1994; Aydin & Johnson , 1978; Ballas, et al., 2015; Fossen, et al., 2007; Taylor & Polland, 2000). , a pre-existing band experiences strain hardening (Aydin & Johnson , 1978; Shipton & Cowie, 2003). As a result, new bands form to accommodate additional strain. This is why conjugate sets or anastomosing clusters of deformation bands are common. Cataclastic bands usually form at burial depths greater than 1 km, but there is evidence of their presence at shallower burial depths in unconsolidated sandstones (Cashman & Cashman, 2000; Rawling & Goodwin, 2003). They are often found in fault damage zones, i.e. in the volume of rock that accommodates deformation during initiation and propagation of slip along fault (McGrath & Davison, 1995; Rotevatn & Fossen, 2011; Shipton & Cowie, 2001; Shipton & Cowie, 2003). Since deformation bands are well below the resolution of seismic data, their extent within the damage zone is not easy to predict (sub-seismic faults are generally faults with an offset of < 10 m that cannot be detected using seismic reflection data, although strike slip faults of much larger offsets are also not resolvable). Moreover, it has been found that no relationship exists between fault displacement and frequency of deformation bands (Schueller, et al., 2013): the same frequency of deformation bands may be associated with seismically resolvable faults and sub-seismic faults.

It is highly likely that deformation bands will be present in most high porosity sandstone reservoirs, hence understanding how they influence fluid flow, and determining their petrophysical properties, is key to accurate reservoir characterization. Several studies have highlighted how deformation bands can negatively affect fluid flow, leading to pressure compartmentalization, a higher degree of tortuosity, fluid bypass and a lower than expected reservoir permeability (Ogilvie, et al., 2001; Qu & Tveranger, 2016; Rotevatn & Fossen, 2011; Rotevatn, et al., 2017; Schultz & Siddharthan, 2005; Shipton, et al., 2002; Shipton, et al., 2005; Wilkins, et

al., 2019). However, most of these studies have relied on results from reservoir simulations and analysis of field data. Here, it is presented the first *in situ* visualization and quantification of sub-core scale single phase and multiphase fluid flow experiments in a sandstone rock core that contains deformation bands and fine-grained laminae. Laminae are mm-thick sedimentary layers forming due to episodic changes in depositional energy (Campbell, 1967). Single phase flow experiments were conducted using PET imaging. Multiphase flow experiments were performed by injecting CO_2 into a water-saturated rock sample and acquiring several consecutive medical X-ray CT scans. Results demonstrate that deformation bands significantly influence single phase flow and that in a multiphase flow setting, they have a profound effect on fluid phase distribution within the rock.

4.2. Methodology

The 5 cm diameter, 10 cm long rock core used in this study was retrieved from a borehole depth of 57 m in the Navajo sandstone formation. The borehole was drilled into the hanging wall of the Big Hole normal fault, in the north of the San Rafael Swell, Utah (Shipton, et al., 2002). The core was sampled from the 17 m thick damage zone that surrounds the Big Hole Fault at this location. The host rock is characterized as a fine-grained sandstone with cataclastic deformation bands (Figure 4-1a).

4.2.1. Micro-CT

To characterize the geometry of the deformation bands, the core was scanned at the University of Strathclyde with an X-ray micro-CT scanner (Nikon XT H 225 LC) that produced three-dimensional (3D) tomographic images with a voxel size of 0.029x0.029x0.029 mm. The above mentioned facility was, however, not available for imaging during the core flooding experiments. Core flooding experiments were conducted at Stanford University using medical CT and PET imaging. The high-resolution micro-CT images provide more detailed information on the deformation band geometries that could not be inferred by the lower resolution of medical CT and PET scanner.

4.2.2. Porosity characterization

The 3D porosity distribution within the core was determined using a medical X-ray CT scanner (General Electric Hi-Speed CT/i) at Stanford University. Image

acquisition was performed at 120 kV and 200 mA, obtaining a voxel dimension of 0.3125x0.3125x0.625 mm. Images of the core were taken when fully dry (CT_{dry}) and when fully water-saturated (CT_{water}). The porosity, Φ, was then calculated using the following relationship (Withjack, 1988; Akin & Kovscek, 2003):

$$\Phi = \frac{CT_{water} - CT_{dry}}{I_{water} - I_{air}} \quad (4\text{-}1)$$

where *I water* and *I air* are the water and air X-ray attenuation values respectively, which differ by 1000 Hounsfield units (Wellington & Vinegar, 1987). To reduce noise in CT images at least three series for each condition were acquired and averaged (Pini, et al., 2012). The images of the entire core were discretized into 38x38x76 cells, each with a dimension of 0.125 cm.

4.2.3. Single phase permeability characterization

Bulk intrinsic permeability was determined using the core-flooding set-up described in the section 4.2.4 and under the same conditions of temperature, pressure and confining pressure as for the multiphase flow experiment. Injecting water at several flow rates into the water-saturated core sample and measuring corresponding differential pressure across the core, allowed permeability calculation with Darcy's Law.

To investigate the 3D distribution of permeability within the core, a tracer experiment was conducted within the micro-PET scanner (Siemens Inveon D-PET) using the experimental setup described in Zahasky & Benson (2018). Before fluid injection, the core was wrapped in two heat-shrinkable Teflon layers and a rubber sleeve to avoid any leakage of the confining fluids into the core. The core was then placed in an aluminum core holder with inlet and outlet caps etched with a pattern of connected grooves for an even distribution of injected fluids. Finally, the core holder was placed in the micro-PET scanner and connected to the core flooding equipment.

To ensure full core water saturation, the core was first dried. CO_2 was then injected to displace the air, followed immediately by water that was injected for displacing and dissolving the CO_2. Once the core was fully saturated, a solution of Fludeoxyglucose (^{18}F-FDG) diluted in tap water was injected at 4 mL/min. The

approximate radioactive concentration was 0.52 mCi/mL. Throughout the experiment a PET scan continuously acquired photon detection data. The experiment was carried out at a constant temperature of 20 °C, with a confining pressure of 2.4 MPa. The back pressure was maintained just above atmospheric pressure.

To calculate the 3D concentration field of the radiotracer within the core, the PET scan data was reconstructed with a time-step length of 40 seconds. The image-based core was discretized into a grid of 22x22x42 cells giving a voxel size for each concentration measurement of 0.23x0.23x0.23 cm. Analysing concentration measurements as a function of time from the PET scans, enables estimates of the mean arrival time and fluid velocity at any location within the core. The radiotracer concentration in each voxel over time was fitted with a first order Gaussian function to remove background noise (Vasco, et al., 2018). The total mass of radiotracer was calculated for each voxel using the temporal zero moment equation

$$M0 = \int_0^t c\, dt \tag{4-2}$$

where c is the radiotracer concentration in each voxel. The mean arrival time is identified as the centre of mass of the Gaussian function and calculated with the temporal first moment equation (Naff, 1990).

$$M1 = \int_0^t ct\, dt \tag{4-3}$$

The normalized first moment then defines the mean arrival time of the plume centre.

$$nM1 = \frac{M1}{M0} \tag{4-4}$$

Knowing the distance between two adjacent units, i.e. the distance between voxels, a map of the velocity field can be derived. The velocity is normalized, enforcing a mass balance, by setting the total flow rate of each cross-sectional slice within the core equal to the inflow rate imposed in the experiment (4 mL/min). This analysis assumes flow is parallel to the axis of the core, a good approximation as the cylindrical faces of the core were no-flow boundaries

4.2.4. Multiphase core flooding experiments

To determine the multiphase flow properties of the rock core, CO_2/water drainage capillary pressure experiments (Pini, et al., 2012) at steady-state conditions were conducted at 25 °C and 9 MPa, with a confining pressure of 11 MPa. Drainage is the process of displacing the wetting phase (water) with non-wetting phase (CO_2). Near ambient temperature was used here because previous studies have shown that temperature has no influence on the saturation end point when CO_2 is injected in a water saturated sample (Niu, et al., 2015)**.**The core flooding setup is similar to the one used in previous experiments (Krevor, et al., 2012; Ni, et al., 2019; Perrin & Benson, 2010) and a schematic diagram can be found in Appendix 2 (Figure A1). The core was not fired before the experiment, due to the low clay content (Shipton, et al., 2002) and because previous studies have shown that firing in CO_2/water/sandstone (with low clay content) system does not change experimental results and wetting properties (Garing & Benson, 2019). The core was first dried in the oven for several days and then wrapped using the same layering protocol as for the single phase experiment (section 4.2.3). Since the CO_2 can permeate through Teflon, an additional layer of aluminum foil has been placed between the Teflon layers to avoid any radial diffusion of CO_2 out of the rock core. The core was then placed in an aluminum core holder and connected to a core flooding setup suitable for conducting high pressure and temperature-controlled experiments.

The flooding system consisted of a syringe pump (Teledyne Isco 260D) for pressurizing the confining fluid, connected to the outer part of the core holder. Backpressure in the core was maintained by a syringe pump (Teledyne Isco 1000D), connected to two dual water syringe pumps (Teledyne Isco 500D) and a two phase separator (TEMCO AMS-900). The phase separator collected and separated water and CO_2 coming out the core. Water sitting on the bottom of the separator, progressively refilled the back-pressure pump, which then refilled the water pumps. CO_2 on the top of the separator was connected to the refilling system of two dual CO_2 syringe pumps (Teledyne Isco 500D) used for injection of CO_2 into the core. Both fluids were injected in the core at constant temperature using a heat exchanger bath ahead of the inlet. Pressure was recorded with two high accuracy pressure transducers (Paroscientific) measuring pressure at the inlet and outlet of the core. The medical X-ray CT scanner

(section 4.2.2) was used for obtaining scan images of the CO_2 saturated core, water-saturated core and partially saturated core with a voxel size of 0.3125x0.3125x0.625 mm.

Before CO_2 injection, the rock core was fully saturated with water that had been pre-equilibrated with CO_2 at the experimental conditions. For the drainage experiment, 100% CO_2 was continuously injected at progressively higher flow rates, from 0.3 mL/min to 20 mL/min. At these conditions the capillary number $Ca = \frac{v\,\mu_{CO_2}}{\gamma}$ ranges from 10^{-7} to 10^{-8}, where ν is the fluid velocity (m/s), $\mu_{CO2} = 7.06 \times 10^{-5}$ (Pa ·s) is the viscosity of the CO_2 at experimental conditions and γ = 35 (mN/m) is the CO_2/water interfacial tension. This suggests that capillary forces dominate over viscous forces in this system. A Bond number, $Bo = \frac{\Delta\rho g L^2}{\gamma}$ (density difference $\Delta\rho$ of 201 kg·m^{-3} and a pore length L of 50 micron) on the order of 10^{-5} indicates that buoyancy forces are smaller compared to capillary forces.

At each flow rate each flow rate, a minimum of least 5 PV (1 PV = 38 mL) of CO_2 were injected to ensure steady state was reached (Perrin, et al., 2009). Once steady state conditions were reached, partially saturated scan images (CT_{exp}) were taken for measuring CO_2 saturation (S_{CO_2}), using the following formula (Akin & Kovscek, 2003):

$$S_{CO_2} = \frac{CT_{exp} - CT_{wat\ sat}}{CT_{CO2\ sat} - CT_{wat\ sat}} \tag{4-5}$$

where $CT_{wat\ sat}$ are scan images taken when the core was fully saturated with equilibrated water, $CT_{CO2\ sat}$ are the scan images of the fully CO_2 saturated core. For each condition, at least three series of scans were taken; and the average of the three was computed for reducing uncertainties on saturation results (Pini, et al., 2012). The resulting images were then coarsened for further noise reduction, obtaining a final voxel resolution of 0.125x0.125x0.125 cm.

Capillary pressure at the inlet portion of the core was measured for each flow rate as the difference between the core inlet and outlet pressure readings. This assumes

that during steady state CO_2 injection the pressure recorded at the inlet is the CO_2 pressure and the pressure recorded at the outlet is the water pressure (Pini, et al., 2012).

4.3. Results

4.3.1. Deformation band geometry

Figures 4-1a and 4-1b show a photograph of the core alongside a 3D image of the distribution of attenuation values from the X-ray micro-CT scanner: higher attenuation values, in white, correspond to higher density materials. A deformation band is clearly visible in both images traversing the full sample horizontally from end-to-end, at an angle of approximately 18° to the long-axis of the core. Two core-perpendicular laminae of finer grained material are also apparent in the micro-CT scan (Figure 4-1b). Analysis of sequential cross-sectional slices in the X-ray micro-CT scan (Figures 4-1c-1f) show that, rather than a single band, there are two bands. These offset the first and second laminae by 3 mm and 5 mm respectively in the slice shown in Figures 4-1c and 4-1e. On all the X-ray micro-CT slices, the two main deformation bands are separated by host rock and therefore they do not isolate any portion of the core (Figure 4-1d). Toward the end of the core (Figure 4-1f), only one deformation band is present, which takes the form of a small anastomosing cluster.

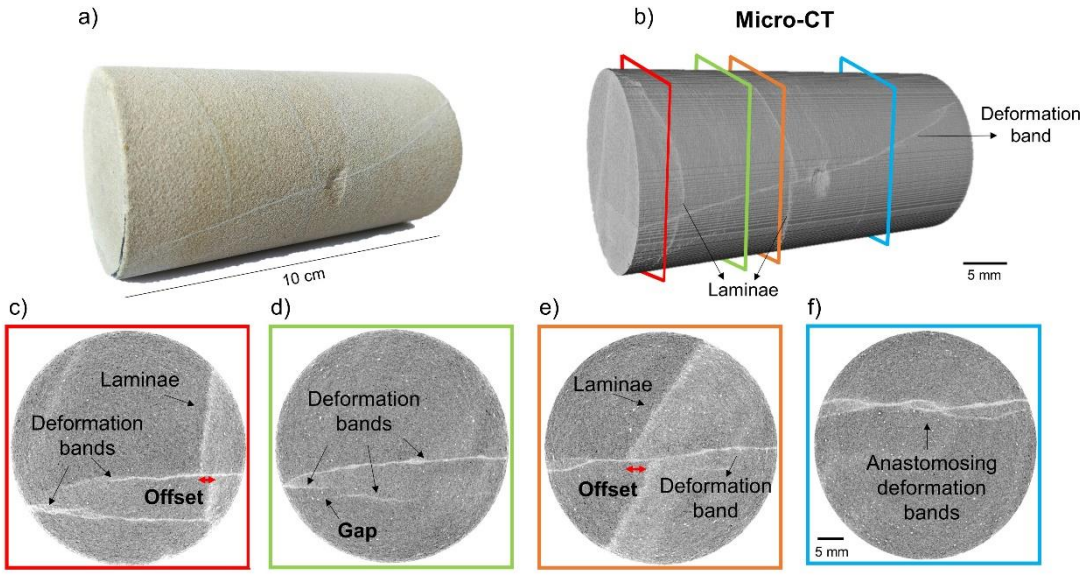

Figure 4-1. a) Sandstone core sample with cataclastic diagonal deformation band. b) 3D micro-CT scan of the sandstone core: the sample is characterized by a cataclastic deformation band and laminae. c) 2D Slice image showing that the two deformation

bands offset the first lamina by 3 mm. Deformation bands do not connect to each other on the left side of the image. d) A third deformation band appears in this slice. The bands are not joined and hence they do not form any isolated compartments. e) Second lamina cut by a single deformation band. Offset of about 5 mm. f) Small anastomosing network of deformation bands at the end of the core.

4.3.2. Porosity distribution

The distribution of porosity within the core, based on the dry and water-saturated medical X-ray CT scans (section 4.2.2), is shown in Figure 4-2. The deformation bands and laminae are clearly visible as low porosity features. Bulk porosity of the core was calculated as 0.196. Deformation band porosity ranges from 0.07 to 0.15, while porosity of laminae varies from 0.13-0.15.

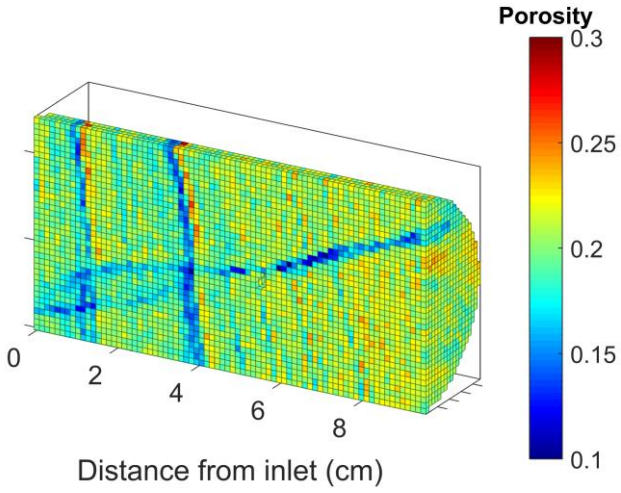

Figure 4-2**.** Porosity map calculated by using water-saturated and dry scan images with the medical X-ray CT scanner. Voxel resolution 0.125x0.125x0.125 cm. An uncertainty (σ_φ) of 0.0082 in voxel porosity due to random error of CT number was calculated using methods explained in Pini et al. (2012).

4.3.3. Intrinsic permeability

Based on measurement of the inlet and outlet pressures at a constant flow rate, a bulk sample permeability of 53 md was estimated using Darcy's Law. The heterogeneous distribution of permeability within the core was investigated using the PET scanner. Figure 4-3 shows the concentrations of the single phase radiotracer injection experiment during six different timeframes of the PET scan taken at consecutive 2-minute intervals. Stylized deformation bands and laminae (derived from the micro-CT images) have been superimposed on the PET images to illustrate their

effect on the tracer plume migration. Results show that the tracer plume above and below the bands is beginning to diverge 4 min after the start of injection. This effect is more pronounced with increasing distance from the inlet. There is a very low radiotracer concentration in the bands.

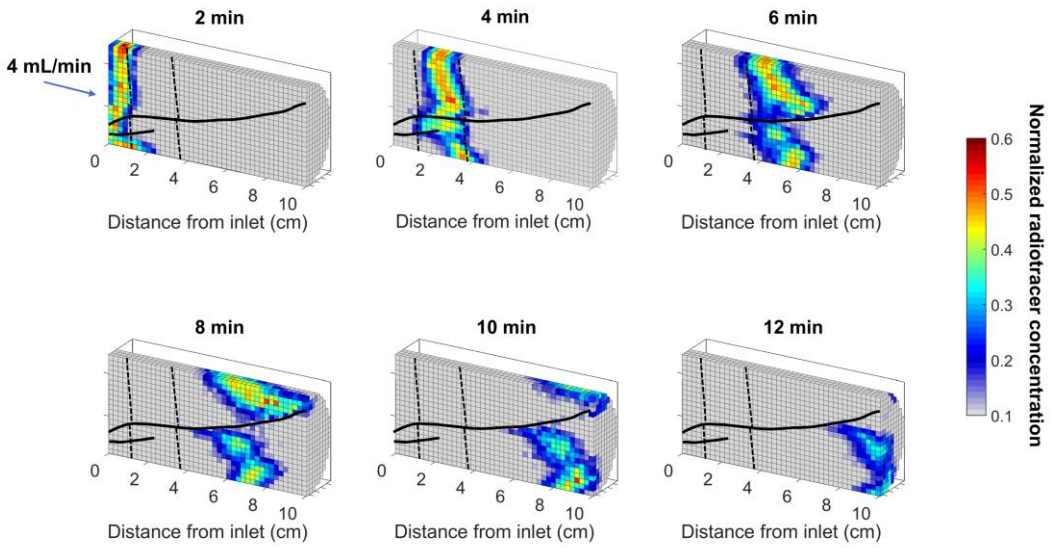

Figure 4-3**.** Axial plane snapshots of radiotracer concentration measured at 2-minute time intervals after injection at 4 mL/min into a sandstone core with deformation bands. In black, the approximate deformation bands (continuous black lines) and laminae (dashed black lines) locations are superimposed on the PET images. Voxel size is 0.23x0.23x0.23 cm.

The 3D map of mean arrival time calculated from the PET images (Figure 4-4a) shows a significantly delayed arrival time for the portion of the host rock that is below the deformation bands compared to above. In the corresponding 3D map of fluid velocity (Figure 4-4b) there is a clear distinction between velocity in the rock above and below the deformation bands. These differences are related to the geometry of the deformation band within the sample. The deformation band, along which the estimated velocity is almost zero, subdivides the host rock into two regions. In the upper region, the cross-sectional area decreases towards the outlet and hence, according to the principle of continuity, if the flow rate is held constant, the velocity increases. Vice-versa for the region below the bands, the cross-sectional area increases towards the outlet and, hence, the fluid velocity decreases. In both the estimated mean arrival time

(Figure 4-4a) and the velocity (Figure4- 4b) maps there is no discernable effect of the two sub-vertical laminae on flow.

To estimate the mean intrinsic permeability for both the host rock and the deformation bands, the PET experiment was modelled numerically using the Stanford University General Purpose Research Simulator software (GPRS) (Cao, 2002; Jiang, 2008; Li, 2011; Boon, et al., 2018; Cao & Aziz, 2002; Krause, 2012; Krause, et al., 2013; Li, et al., 2012; Li & Benson, 2015). Details of model set-up are included in supporting information (Table A1, Figure A2). Multiple combinations of the host rock permeability and deformation band permeability were tested. Each combination had an equivalent bulk core permeability equal to the experimentally measured value of 53 md. Flow within the core was modelled in 2D, using a grid of 35X78 cells with a grid cell resolution of 0.125 cm, a homogeneous host rock and a single, straight, diagonal deformation band are shown in Figure 4-4c). The velocity of the fluid for each cell in the simulations was calculated using Darcy's law, assuming an axial flow direction. The simulation results for three combinations of host rock and deformation band permeability were 55 md and 10 md, 100 md and 0.5 md, 500 md and 0.0005 md. A comparison of the velocity fields calculated from model simulations with the PET-derived velocity field shows that, although all three models have the same bulk permeability, the local velocity distributions differ. The results for a permeability of 100 md for the host rock and 0.5 md for the deformation band most closely resemble the experimental data (Figure 4-4b).

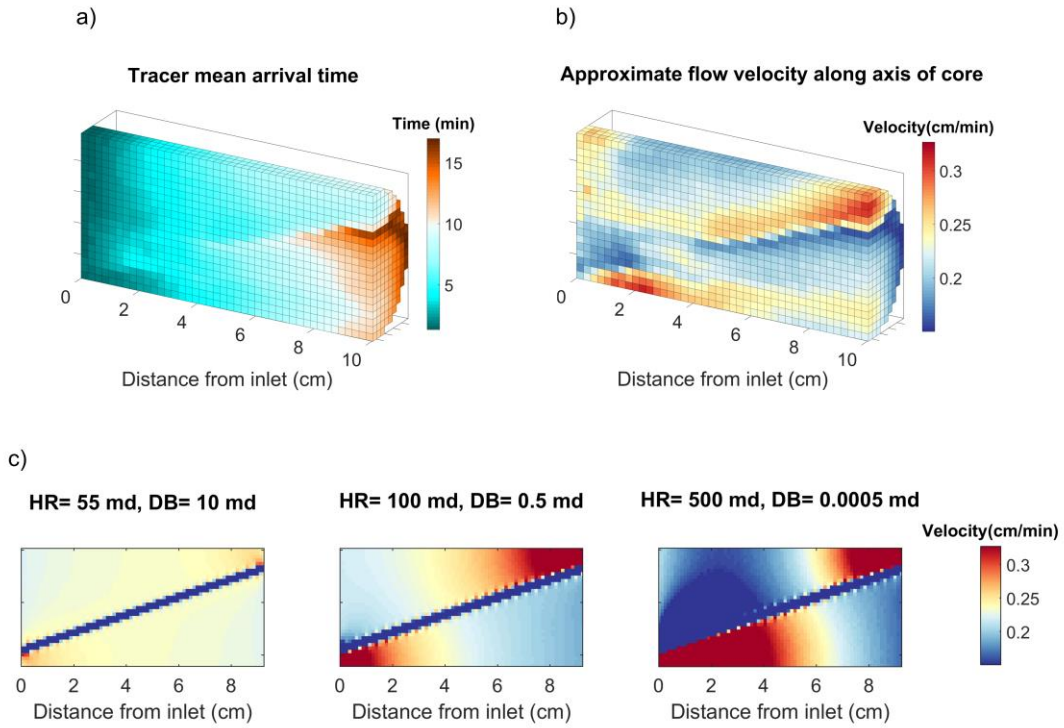

Figure 4-4**.** a) Mean arrival time of the radiotracer solution in the sandstone core with deformation bands. Delayed arrival time in compartment below the deformation bands. b) Fluid velocity along the axis of the core calculated from the experimental data. c) Fluid velocity calculated simulating water injection in three pseudo 3D models with different permeability in the host rock (HR) and deformation band (DB). The model with 100 md in the HR and 0.5 md in the DB provides the best match with the velocity field obtained in the experiments.

The heterogeneous permeability distribution was estimated using the porosity-permeability relationship proposed by Torabi et al. (2013):

$$k_{HR} = 1e-9\ {\varphi_{HR}}^{AHR} \tag{4-6}$$

$$k_{DB} = 2e-7{\varphi_{DB}}^{ADB} \tag{4-7}$$

where k_{HR}, φ_{HR}, k_{DB}, φ_{DB} are permeability (md) and porosity (in percentage) of the host rock and deformation bands respectively and A_{HR} and A_{DB} are dimensionless constants. Among several porosity-permeability relationships, this is preferred considering that it specifically relies on core-plug laboratory measurements of undeformed and deformed samples (single and clusters of bands). For this specific study case, porosity for each voxel in the core was taken from the data in Figure 4-2.

The A_{HR} and A_{DB} coefficients found by Torabi et al. (2013) are 9.09 and 6.31, respectively. However, by using these coefficients the resulting bulk core permeability, calculated performing single phase simulations, was 280 md as opposed to the 53 md experimentally calculated. The constants A_{HR} and A_{DB} were then fitted by constraining the bulk core permeability to have the measured value of 53 md and the bulk host rock and deformation band permeabilities to have values of 100 md and 0.5 md respectively, as estimated from the analysis shown in Figure 4-4. This resulted in estimates for the constants A_{HR} and A_{DB} of 8.6 and 5.4 for the host rock and deformation bands. respectively. The estimated permeability in each cell is shown in Figure 4-5.

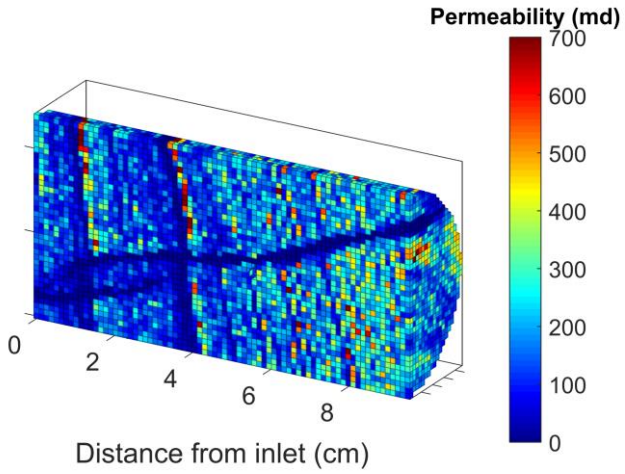

Figure 4-5**.** Permeability distribution in millidarcy (md) calculated using an adapted version of the porosity-permeability relationship found in Torabi et al. (2013).

4.3.4. Multiphase flow properties

Results of the core flooding CO_2 injection experiments are shown in Figure 4-6. The injection flow rate was steadily increased in a step-wise fashion over time (Figure 4-6a). At each step, the flow rate was maintained for a sufficient duration to achieve a steady-state CO_2 saturation distribution (as determined from consecutive medical CT scans). Figure 4-6b shows that as the flow-rate increases, CO_2 saturation increases in the host rock compartments above and below the deformation bands, but that there remains a lower CO_2 saturation in the compartment below the bands. At low flow rates (0.3 mL/min – 0.6 mL/min – 1 mL/min – 2 mL/min) CO_2 is not able to saturate the outlet of the core below the deformation bands, creating a shadow zone of reduced CO_2 saturation.

Due to their low porosity and permeability and high capillary entry pressure, the deformation bands exhibit low CO_2 saturation, even at high flow rates. Flow across the bands can only occur if the capillary entry pressure of the bands has been exceeded. Hence, the bands act as capillary barriers and inhibit most flow between the two compartments even at high flow rates.

In contrast to the single phase PET tracer experiment (Figure 4-3), the laminae have a visible effect on CO_2 distribution, with CO_2 saturation being lower in the laminae than the surrounding host rock. The laminae also act as capillary barriers, although to a lesser extent than the deformation bands. Saturation in the laminae remains lower than in the surrounding rock even when the saturation front has passed through the bands. Only once the flow rate reaches 5 mL/min do the laminae fully saturate and at that point they are no longer clearly visible in the X-ray CT images.

The slice-averaged CO_2 saturation for the individual host rock compartments (Figure 4-6c) indicates that the CO_2 saturation is lower in the compartment below the bands compared to above the bands. This discrepancy becomes less pronounced at the high flow rates. Despite this, even at 20 mL/min of CO_2 injection, the portion of the core near the inlet shows a lower CO_2 saturation in the compartment below the bands.

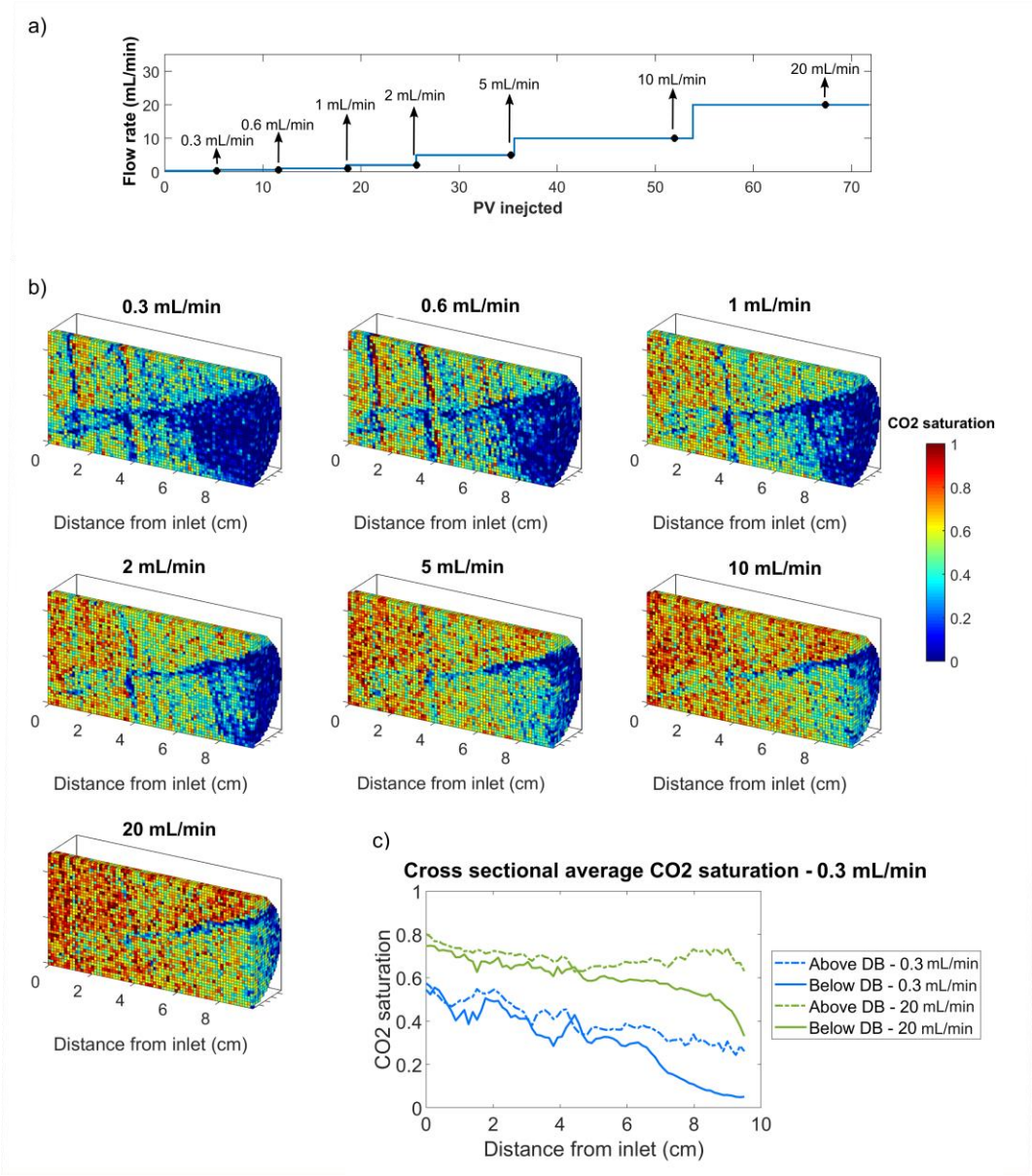

Figure 4-6**.** a) Injection strategy for the core flooding drainage experiments. CO_2 was injected in the water saturated sample at progressively higher flow rates of 0.3, 0.6, 1, 2, 5, 10, 20 mL/min. Circle marks corresponds to the scan images taken at steady state conditions for each flow rate. b) CO_2 saturation measured for different flow rates at steady state conditions. Voxel resolution 0.125x0.125x0.125 cm. Grid size is 38x38x76 cells. c) Slice average CO_2 saturation for the compartment below and above the deformation bands (DB) for both flow rates, 0.3 mL/min and 20 mL/min. The difference in saturation between the two compartments is higher towards the outlet and less pronounced for the highest flow rate. An uncertainty of 0.18 in voxel saturation measurement (σ_S) due to random error of CT number was calculated using methods explained in Pini et al. (2012).

4.4. Numerical modelling of multiphase flow experiments

Multiphase fluid flow simulations were conducted using the GPRS simulator to fully understand the CO_2 saturation distribution and migration in the presence of deformation bands. The porosity and permeability fields used in the model were those derived in section 4.3.2 and 4.3.3. The capillary entry pressure was calculated for each grid block in the model using the Leverett J-function model, which scales the capillary pressure curve derived from the experimental data based on the porosity and permeability distribution (Li, 2011). Water and CO_2 relative permeability curves were calculated using the Brooks-Corey model (Brooks & Corey, 1964). Details of input parameters are included in supporting information (Text A1, Figure A3, A4, A5, Table A2). Given that the bands traverse the full core width, for simplicity, a 2D model was developed (grid size 35X78 cells, pixel resolution 0.125 cm) to model the central rectangular cross-section along the core. The model is initially fully saturated with water prior to injection of CO_2. Boundary conditions (Figure A6 in supporting information) were no flow conditions on the lateral faces, a time-varying CO_2 flow rate, adjusted for cross-sectional area, at the inlet face equal to the experimental flow rate (Figure 4-6a) and a fixed outlet pressure of 9 MPa.

4.4.1. Multiphase fluid flow simulation with capillary end effect

In the experimental setup there is a small gap between the core and the outlet cap, which effectively creates a reservoir at the end of the core where the permeability and porosity are very high. This zone creates a capillary pressure discontinuity. A negative gradient of CO_2 saturation (Pini & Benson, 2013) is associated with this "discontinuity of capillarity in the wetting phase" (Huang & Honarpour, 1998), creating a so-called capillary end effect. To simulate this effect, a small reservoir characterized by low capillary entry pressure (0.02 kPa), high porosity (0.7), and high permeability (100000 md) was placed in the final right-hand column of grid cells at the end of the model.

Simulation results show, for all flow rates, a lower CO_2 saturation in the compartment below the deformation bands than the one above it (Figure 4-7a). A decreasing CO_2 saturation near the end of the core is also apparent (Figure 4-7b). As

in the experiment, the difference in saturation above and below the bands is higher toward the outlet of the core.

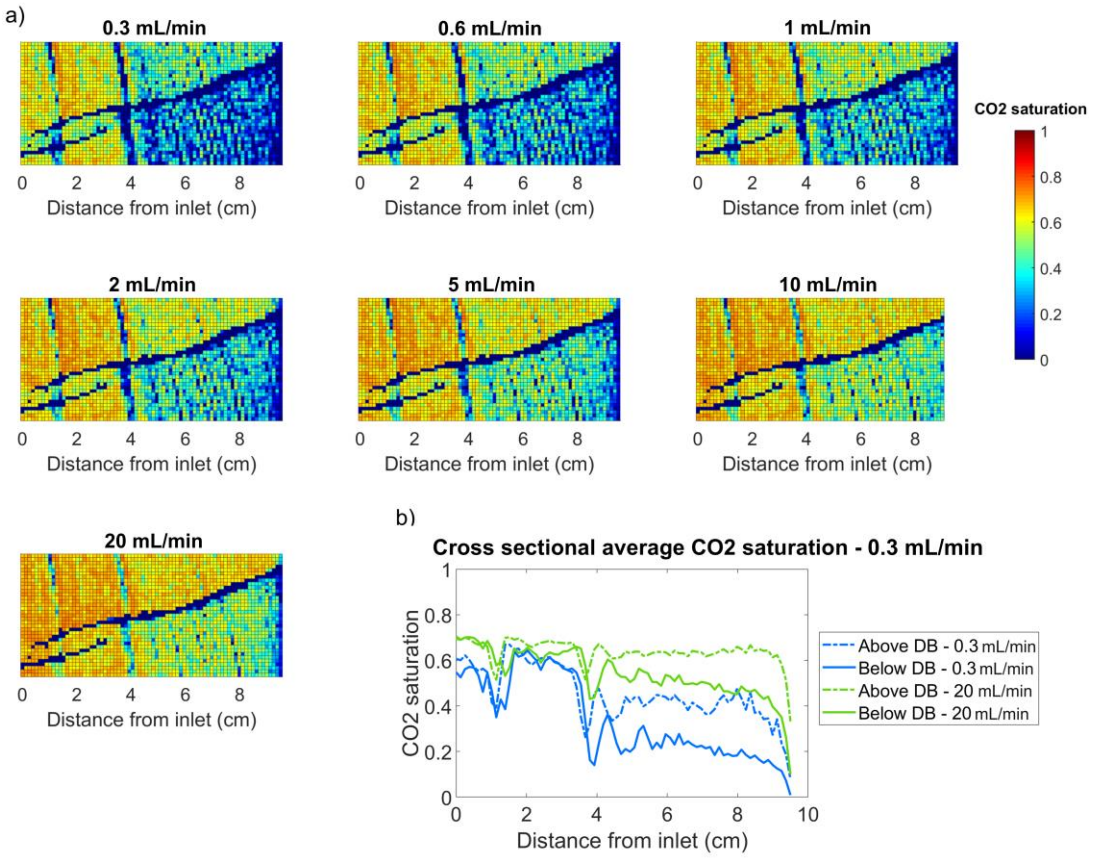

Figure 4-7. a) Simulation results for the model with small reservoir at the end (capillary end effect). Lower CO_2 saturation is seen in the portion below the deformation bands. b) Comparison between the two compartments at 0.3 mL/min and 20 mL/min. This plot illustrates the negative CO_2 saturation trend due to capillary end effect. For all the flow rates, there is a lower CO_2 saturation in the compartment below the bands compared to above the bands.

The model is able to capture the main characteristics of the experiment, specifically the difference in saturation between the two compartments and the effect of the laminae on CO_2 distribution (Figure 4-8). At 0.3 mL/min, the model over-predicts the CO_2 saturation towards the outlet (Figure 4-8 top left). This is likely related to an underestimation in the model of the capillary entry pressure near the outlet. As the viscous pressure drop increases with increasing flow rate, the influence of capillary heterogeneities on fluid saturation distribution decreases. At 2 mL/min (Figure 4-8 top right) the model agrees with the experimental CO_2 saturation at the outlet of the core,

suggesting that the decreasing CO_2 saturation trend in both compartments is strongly influenced by the capillary end effect. At 20 mL/min the model under-predicts the final CO_2 saturation (Figure 4-8 bottom left). This can be explained by the fact that, during experiments, the capillary end effect has lower extension at high flow rates (Guédon, et al., 2017). For flow rates higher than 1 ml/min, the simulation results show higher inlet water saturation and therefore lower capillary pressure values as compared to the experimental results (Figure 8 bottom right). This is probably due to either an overestimation in the model of the capillary entry pressure near the inlet of the core or small errors in the relative permeability used within the model.

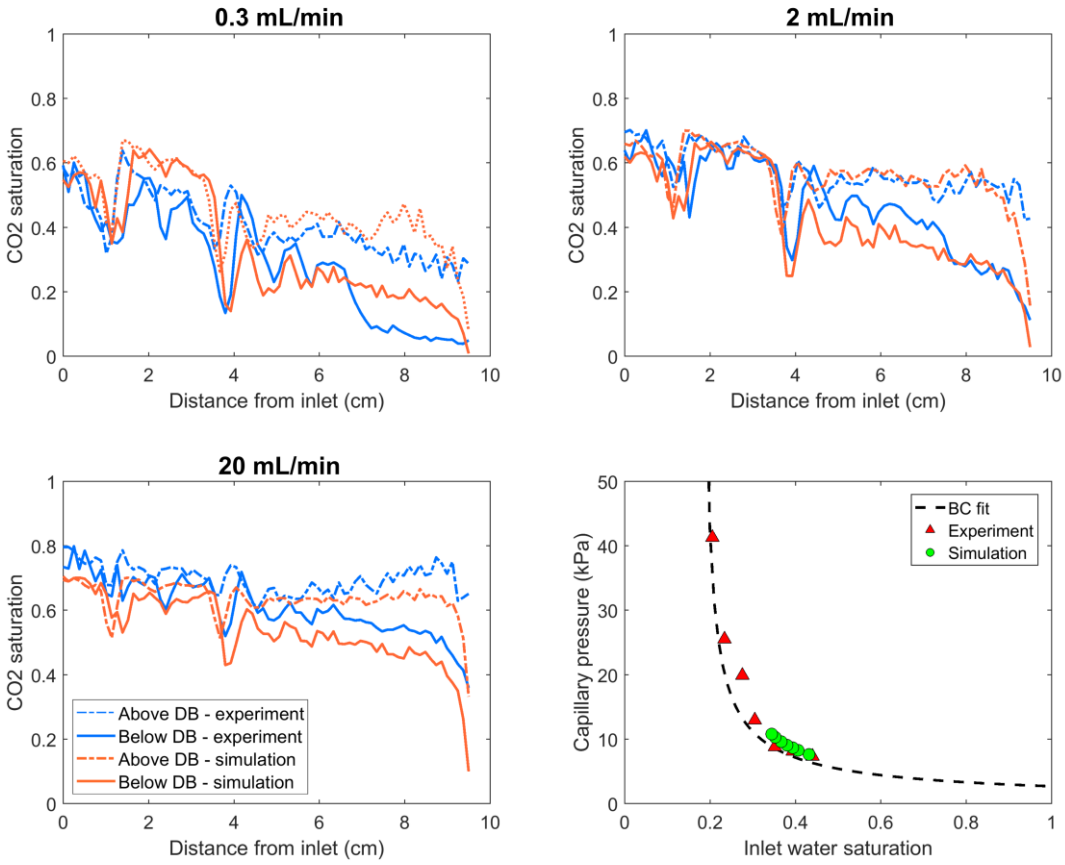

Figure 4-8.Comparison between experimental (blue) and simulation results (orange) for three different flow rates. The model captures the CO_2 saturation behavior in the experiment at 0.3 mL/min (upper left) and 2 mL/min (upper right). At 0.3 mL/min, the saturation shadow zone seen in the experiment is not replicated in the simulation. At 20 mL/min (lower left) the negative trend shown in the simulation is not representative of the experimental results. (lower right) Inlet capillary pressure values for all flow rates, resulting from experiments and simulations with small reservoir at the end of the

core. The capillary pressure in steady state conditions can be assumed to be equal to the differential pressure measured at the inlet slice of the core (Pini, 2012).

4.4.2. Multiphase fluid flow simulation without the capillary end effect

To exclude the influence of the capillary end effect on the CO2 saturation distribution, and isolate the impact of the deformation bands, the same model was used with no small reservoir at the end this time. Results (Figure 4-9) show that the deformation bands continue to compartmentalize fluids in the host rock and that the compartment below the bands continues to have a lower saturation that the one above. At 20 ml/min small portions of deformation bands become saturated with CO2, leading to cross flow between compartments above and below the bands. As shown in Figures 2, 5 and S5, there is no substantial difference in porosity, absolute permeability or capillary entry pressure between the two compartments. As is the case with single phase flow, the difference in CO2 saturation can be attributed to the geometry of the two compartments. The compartment above the bands has a smaller cross-sectional area towards the outlet, resulting in a higher fluid velocity and a higher pressure gradient when compared to the compartment below the bands.

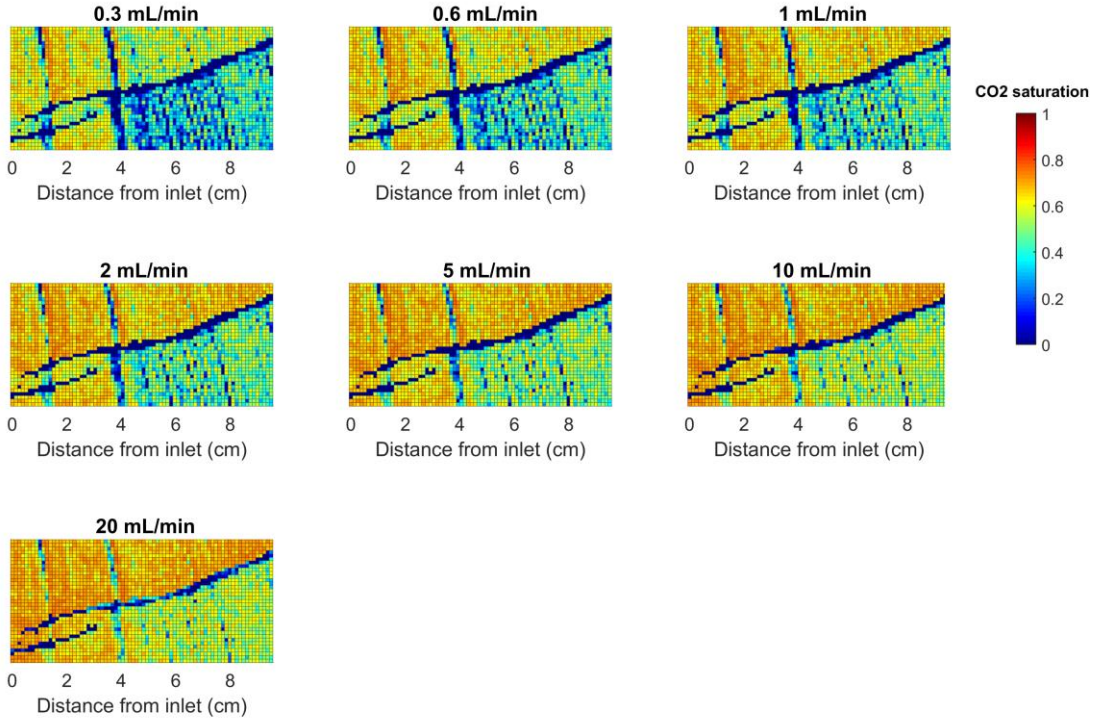

Figure 4-9. Simulation results for the model without small reservoir at the end (with no capillary end effect). Lower CO_2 saturation is shown in the compartment below the

deformation bands. Some portions of the deformation bands are partially saturated with CO_2 at 20 mL/min.

4.4.3. Multiphase fluid flow simulation without laminae

The experimental observations (Figure 4-6) show that the laminae have a significant influence on CO_2 migration. To distinguish the relative effects on CO_2 saturation of the deformation bands and the laminae, a simulation was conducted with no end effects and with the laminae removed.

Figure 4-10 shows CO_2 saturation and capillary pressure distribution with and without the laminae for an injection rate of 0.3 mL/min. This flow rate has been chosen, because the highest influence of laminae on fluid flow has been observed during these drainage flow conditions. With the laminae removed, the difference between the CO_2 saturation above and below the bands is more pronounced; the low saturation levels in the bottom host rock compartment are maintained at the inlet. These results confirm the earlier experimental interpretation that CO_2 saturation increases upstream of the laminae. This demonstrates that the laminae act as capillary barriers at low flow rates.

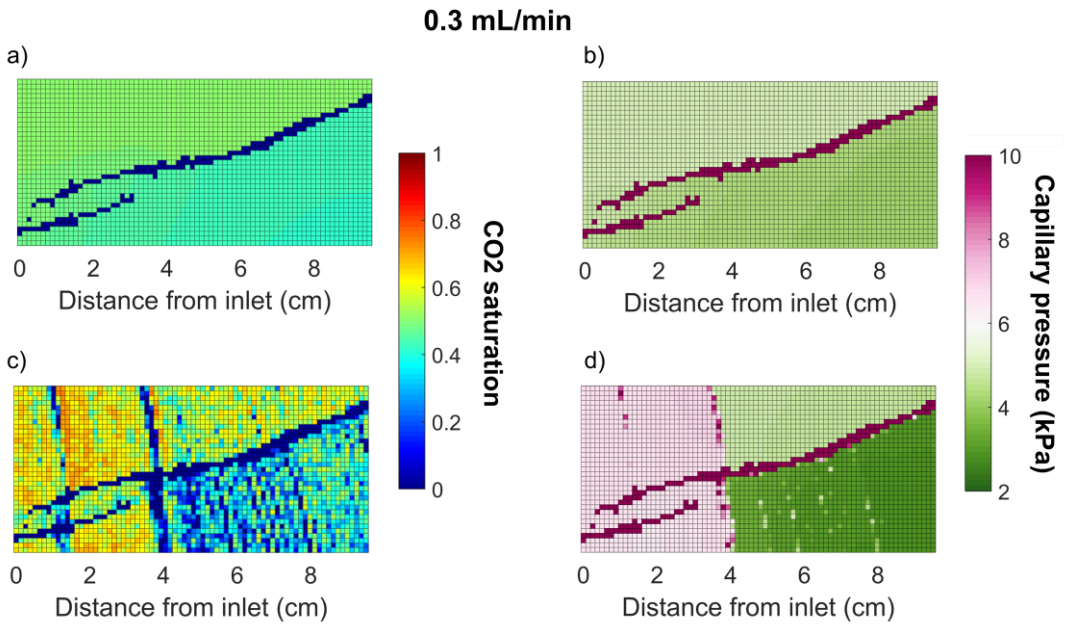

Figure 4-10.a) CO_2 saturation for the model without end effect and laminae. b) Capillary pressure calculated for the model without end effect and laminae. c) CO_2 saturation for the model of the core without end effect. d) Capillary pressure calculated

for the model of the core without end effect. The presence of laminae increases both saturation and capillary pressure for the first 4 cm of the core.

4.5. Discussion

The effect of cataclastic deformation bands on single and multiphase fluid flow have been investigated *in situ* for the first time. While deformation bands do not entirely surround any individual portion of the host rock in the core sample, they significantly contribute to fluid compartmentalization. Deformation bands subdivide the host rock into two distinct regions, above and below the deformation bands. The compartmentalization results in differing fluid velocity distributions and CO_2 saturation values. The low permeability of the bands, demonstrated by the single phase flow experiments, together with their high capillary entry pressure, significantly inhibit cross-flow of CO_2 between the two compartments.

In the experiments, the deformation bands are sub-parallel to the flow direction and therefore fluid is not forced to travel across them. This results in the deformation bands remaining almost entirely unsaturated with CO_2 and almost no cross-flow occurring. If the deformation bands were oriented perpendicular to the flow, a different outcome would be expected. The grain size distribution within individual laminae is narrow because the Navajo sandstone is aeolian. However, within the deformation bands the particle size distribution is much broader. Figure 4-11a shows a microscale image of a deformation band from the Big Hole fault field site. The band is a mixture of larger 'survivor' grains and very fine crushed grain material. This results in almost no residual porosity, since the crushed material entirely fills the gaps between the larger grains (Figure 4-11b). With deformation bands perpendicular to the flow I would expect an effect similar to that of the finer-grained laminae, but much more pronounced as the entry pressure will be much higher.

To understand the implications of my research for multiphase fluid injection at a commercial scale, it is important to be able to characterize deformation band frequency and orientation within a reservoir. Deformation bands do not generally occur with a unique orientation, or indeed, as single isolated bands; they form conjugate sets (Figure 4-11c) and are often present in thick anastomosing clusters. This implies a high degree of 3D reservoir anisotropy and the potential for significant CO_2

channelling in lozenge-shaped compartments confined by deformation bands. Lower fluid saturation zones (shadow zones), fluid compartmentalization, injection pressure buildup and preferential channels for fluid migration, are all potential effects of the presence of deformation bands in a sandstone reservoir. Consequently, adequate characterization of petrophysical deformation band properties,through micro-structural analysis or flow experiments, alongside their orientation, thickness, and spatial distribution, through scan-line sampling, well logs and borehole seismic data, are all important factors to consider when estimating the likely storage volume and injection pressure of, for example, a potential CO_2 storage reservoir.

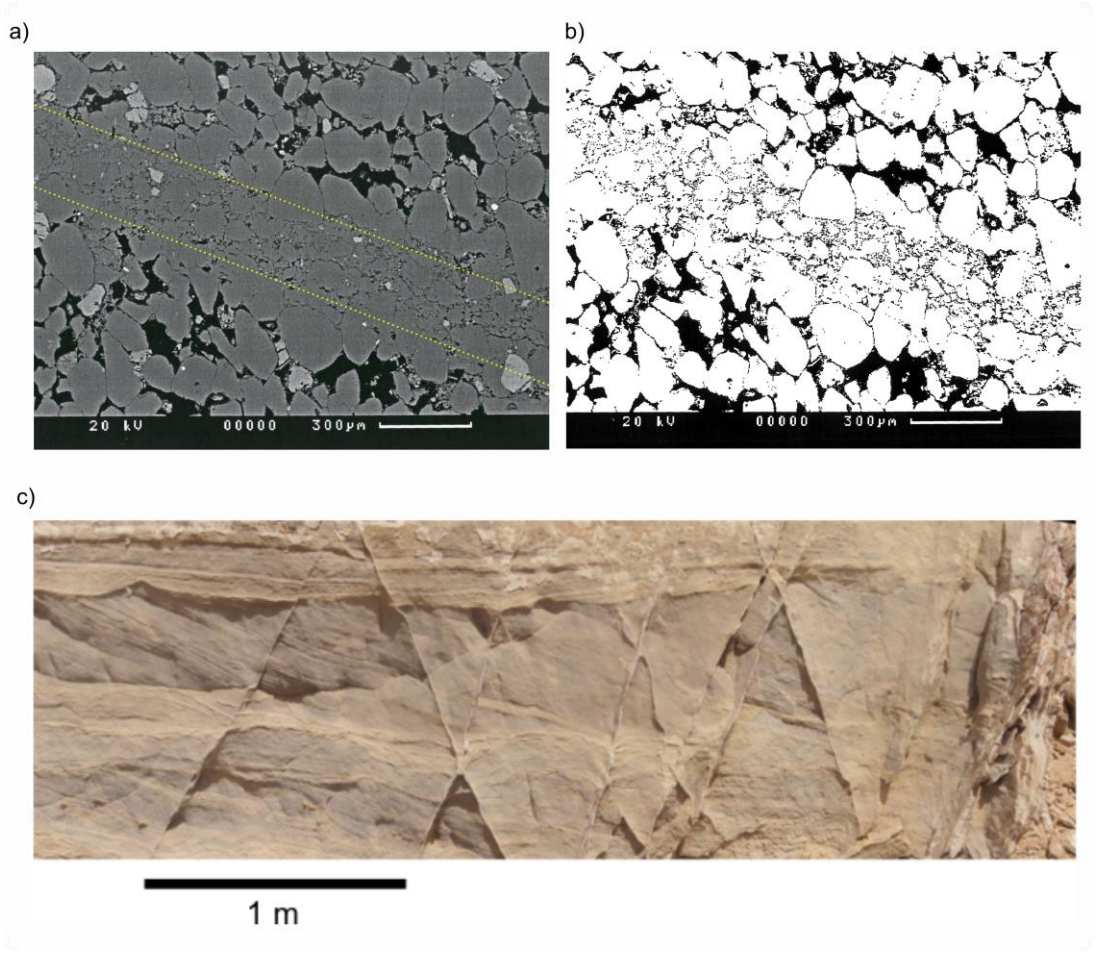

Figure 4-11**.** a) BSEM of a deformation band in the Navajo sandstone at the Big Hole Fault. Deformation bands is included in the yellow dashed lines; pores are in black. b) Segmented image of Figure 4-11a. Smaller grains (white) and pore space (black) along the band. c) Conjugate sets of deformation bands from an outcrop of the Slick Rock Member of Entrada Sandstone in Utah.

4.6. Conclusions

Single phase and multiphase core flooding experiments were conducted in a sandstone core presenting diagonal cataclastic deformation bands and two lower porosity laminae. In the single phase experiment PET imaging revealed that the presence of the diagonal deformation bands created a strong difference in the velocity distributions between compartments of the host rock above and below the deformation bands. This difference was not caused by any difference in porosity and permeability between the two compartments, but instead was attributed to the geometry of the band. No effect of the laminae on single phase flow transport was apparent.

High pressure CO_2 injection drainage experiments were conducted in the same core and imaged with a medical X-ray CT scanner, allowing progressive imaging of CO_2 saturation at different flow rate conditions. Results show that both the finer-grained laminae and the deformation bands acted as capillary barriers. The laminae form weaker capillary barriers than the deformation bands, with the compartment below the bands presenting lower CO_2 saturation for all flow rates, particularly toward the outlet. Numerical simulations of the experiments at low flow rates revealed that whilst some of the low saturation at the outlet was due to the experimental capillary end effect, simulations without the end effect also predicted significant differences in CO_2 saturation due to the presence of the bands. Deformation bands have extremely low permeability and porosity, and a very high capillary entry pressure that inhibits CO_2 migration across the bands. The bands remained saturated with water during the experiments, contributing to the isolation of the two host rock compartments.

At the reservoir scale, deformation bands form conjugate sets and are often present in thick anastomosing clusters. Thus, deformation bands have the potential to channel and compartmentalize both single and multiphase fluid flow. These findings have important consequences for predicting multiphase flow in sandstone reservoirs and specific implications for storage capacity and injectivity of carbon and storage in geological formation.

Chapter 5

EXTREME CAPILLARY HETEROGENEITIES AND *IN SITU* FLUID COMPARTMENTALIZATION DUE TO CLUSTERS OF DEFORMATION BANDS IN SANDSTONES

5.1. Introduction

Accurate site-characterization and understanding of the impact of geology on fluid flow in the subsurface is essential for reservoir management of CO_2 geologic storage projects (Chadwick, et al., 2004; Cowton, et al., 2018; Edlmann, et al., 2016; Eiken, et al., 2011; Hansen, et al., 2013) and enhanced oil recovery operations (Ader & Stein, 1984; Malik & Islam, 2000; Mezzomo, et al., 2001; Sheng, 2013). Small-scale heterogeneities, on the scale of millimetres to centimetres, have been demonstrated to have a strong impact on fluid flow at the reservoir scale (Gershenzon, et al., 2014; Krevor, et al., 2015; Li & Benson, 2015; Lunn, et al., 2008; Qu, et al., 2017; Rotevatn & Fossen, 2011; Saadatpoor, et al., 2010).

Depositional environments and regimes, diagenesis, and structural evolution are all factors promoting multiscale spatial variability of petrophysical and multiphase flow properties in geological reservoirs (Chandler, et al., 1989; Morad, et al., 2010; Wang, et al., 2017; Williams, et al., 2017). Variations in the resulting porosity, permeability, capillary pressure, and relative permeability distributions strongly control reservoir quality, injectivity and fluid/gas capacity. Detailed spatial characterization and quantification of flow properties are required as input parameters for geologic models, necessary for accurate forecasting of important engineering and environmental processes.

Traditional fluid flow property estimation is performed through field observation, core and core-plug analysis, scaling relationships, and interpretation of

borehole log-derived properties (Brown, 1951; Cardwell Jr & Parsons, 1945; Jenning, 1987; Medina, et al., 2011; Odling, et al., 1999; Willis & White, 2000). Advances in experimental and imaging techniques now enable quantification of fluid flow behaviour at the sub-core scale under *in situ* reservoir conditions. Core flooding experiments, combined with imaging techniques such as X-ray computed tomography (CT), enable measurements of three-dimensional (3D) porosity, permeability, relative permeability, and capillary pressure distribution (Akbarabadi & Piri, 2013; Krause, et al., 2013; Krevor, et al., 2012; Perrin & Benson, 2010; Pini, et al., 2012; Pini & Benson, 2013).

In situ characterization studies of sub-core scale multiphase fluid properties in heterogeneous rocks to date have typically focused on simple structures, such as fractures, bedding planes, laminae (Alemu, et al., 2013; Hingerl, et al., 2016; Krevor, et al., 2011; Li, et al., 2019; Ni, et al., 2019; Shi, et al., 2011) and individual deformation bands (Chapter 4). However, a combination of geologic structures is often present in the subsurface, leading to more extreme heterogeneities with complex geometries. For example, cataclastic deformation bands are often found in conjugate sets and clusters of bands (Antonellini & Aydin, 1994; Antonellini & Aydin, 1995; Fossen & Hesthammer, 1997; Rawling, et al., 2001; Shipton & Cowie, 2001; Shipton & Cowie, 2003; Shipton, et al., 2005; Sosio de Rosa, et al., 2018). Cataclastic deformation bands are millimetre-thick tabular structures occurring in sandstones with porosity higher than 0.15 (Aydin, 1978; Antonellini & Aydin, 1995; Fossen, et al., 2007; Schultz & Siddharthan, 2005). They accommodate slip during fault initiation and propagation, and damage zone development (Aydin, 1978; Caine, et al., 1996; Shipton & Cowie, 2003). Continued deformation, often associated with fault growth, can result in dense clusters of conjugate bands with highly complex geometries, even in the case of relatively low offset faults.

The petrophysical properties of cataclastic bands relate to their mechanism of formation: shearing, along with compaction, leads to grain rolling and fracturing. Fine crushed grains fill available pore spaces, decreasing porosity and permeability of the host rock by several orders of magnitude (Aydin & Johnson , 1978; Antonellini & Aydin, 1994; Ballas, et al., 2015; Deng, et al., 2015; Fossen, et al., 2007; Taylor &

Polland, 2000). Cataclastic deformation bands are usually characterized by higher capillary entry pressure values when compared to the surrounding rock (Torabi, et al., 2013). A single deformation band is only able to accommodate few millimetres, or rarely few centimetres of displacement (Aydin & Johnson , 1978). To accommodate higher displacement, new deformation bands must nucleate, adjacent to the pre-existing bands, resulting in the creation of anastomosing clusters (Aydin & Johnson , 1978; Schultz & Balasko, 2003; Shipton, et al., 2002; Shipton, et al., 2005).

Deformation band frequency tends to decrease with increasing distance from the fault (Schueller, et al., 2013; Shipton, et al., 2002). Thick clusters of bands, resulting in very low permeability zones, are likely to be found close to the fault, and within the fault core. The frequency of deformation bands at a given distance from the fault, however, is not related to the maximum fault displacement (Schueller, et al., 2013), and clusters of deformation bands characterize the damage zones of small displacement (< 10 m), seismically unresolvable (sub-seismic) faults. Hence, predicting the presence of deformation bands in a potential reservoir is challenging.

While several studies have highlighted the fact that deformation bands negatively affect fluid flow (Naruk, et al., 2009; Qu, et al., 2017; Rotevatn & Fossen, 2011; Rotevatn, et al., 2017; Shipton, et al., 2005; Wilkins, et al., 2019), the extent of reservoir compartmentalization induced by deformation bands is unclear. Reservoir compartmentalization happens when fluids are segregated into several saturation/pressure regions due to the presence of barriers. Following the reservoir seals classification proposed by Jolley et al. (2010), due to their petrophysical and multiphase flow properties, deformation bands can be considered as “dynamic barriers”, i.e. flow is allowed through the deformation band but the crossflow between host rock compartments is highly reduced, as shown in Chapter4 in both single and multiphase flow conditions.

There are numerous examples of the impact of geologic structures on fluid compartmentalization in the subsurface (Gainski, et al., 2010; Gill, et al., 2010; Hansen, et al., 2013; Milkov, et al., 2007; Richards, et al., 2010; Scott, et al., 2010; Van Hulten, 2010). Unexpected reservoir compartmentalization strongly affects injectivity and adds additional uncertainties on potential storage volume and fluid

mobility (Smith, 2008). Overly simplified geologic models in reservoir simulations fail to predict fluid compartmentalization. Detailed characterization of the pattern and properties of sub-seismic structures, such as deformation bands, is a key challenge in the avoidance of erroneous reservoir simulation forecasts.

In this study, *in situ* multiphase fluid behaviour in a sandstone characterized by clusters of deformation bands is visualized and quantified. High-resolution X-ray micro-CT images are used to define the geometry of the deformation bands. Conjugate clusters of bands subdivide the host rock into multiple compartments. Drainage core flooding experiments were performed by injecting nitrogen into the water-saturated rock core, while medical X-ray CT images were acquired during both un-steady and steady-state flow conditions. This *in situ* imaging at reservoir conditions provides new insights into fluid compartmentalization behaviour of deformation bands during multiphase flow.

5.2. Materials and methods

5.2.1. Rock sample and 3D porosity

The rock core chosen for this study was specifically selected to be representative of the complexity expected to be found in an actual reservoir, regardless of the scale. The sample of the Navajo sandstone formation was collected at 60 m depth in a vertical borehole through the damage zone of a small displacement (8 m) seismically unresolvable normal fault (the Big Hole fault) in Utah (Shipton, et al., 2002). The sample was reshaped to 9.8 cm in length and 5 cm in diameter (Figure 5-1a). A superficial fracture towards the outlet of the rock core formed during core reshaping.

3D digital images of the rock core were obtained with a micro-CT scanner (Nikon XT H 225 LC) in the Advanced Materials Research Lab, University of Strathclyde. The high-resolution images enabled detailed mapping of internal structures and heterogeneities presented by the rock (Figure 5-1b). Deformation bands show higher attenuation values (white) and, therefore are composed of higher density material compared to the host rock. The density in the bands is high due to the mechanism of deformation, which involves grain rolling, fracturing and subsequent

compaction, as opposed to a change in mineralogical composition. The core is characterized by a dense network of deformation bands with angles ranging from 14° to 31° relative to the core axis (vertical in the borehole). Deformation bands subdivide the host rock into multiple compartments and decrease in number towards the end of the core (Figure 5-1b). It is possible to identify several small-scale structures within the sample: For example, a single deformation band and a thick cluster of bands, that are 0.44 mm and 11 mm wide, respectively. Several thin fine-grained laminae perpendicular to the core axis can also be recognized.

A preliminary petrophysical characterization of the rock was obtained by calculating a 3D porosity map of the rock core with a medical X-ray linear scaling technique (Withjack, 1988; Akin & Kovscek, 2003; Mees, et al., 2003). Porosity in each voxel (Φ_i) is calculated as follows

$$\Phi_i = \frac{CT_{wat_i} - CT_{dry_i}}{I_{water} - I_{air}} \tag{5-1}$$

Here, CT_{wat_i} and CT_{dry_i} are CT Hounsfield numbers of water-saturated and dry images, respectively. I_{water} and I_{air} are density values, expressed in Hounsfield Units, of water (0 HU) and air (-1000 HU). These images were acquired using a medical X-ray CT scanner (General Electric Hi-Speed CT/i) at Stanford University. A resolution of 0.325 mm in the x-y plane and 0.625 mm in the z plane was the highest resolution that could be obtained with the instrument, via acquisition at 120 kV and 200 mA. To reduce noise, three sets of images were acquired, averaged and coarsened, resulting in a voxel dimension of 1.25x1.25x1.25 mm. The lower resolution of the medical CT image prevents the spatial characterization of some structural details that are identifiable in the micro-CT images (Figure 5-1b), such as the single band. However, the fast image acquisition offered by the medical CT scanner, compared with the micro-CT scanner, enables imaging during the core flooding experiments. Based on the porosity data in Figure 5-1c, the measured bulk porosity for the whole core is 0.138; this is comprised of a host rock porosity of approximately 0.2, and a deformation band porosity of between 0.01 and 0.12, with an average value for the deformation bands of 0.07 (Figure 5-1c).

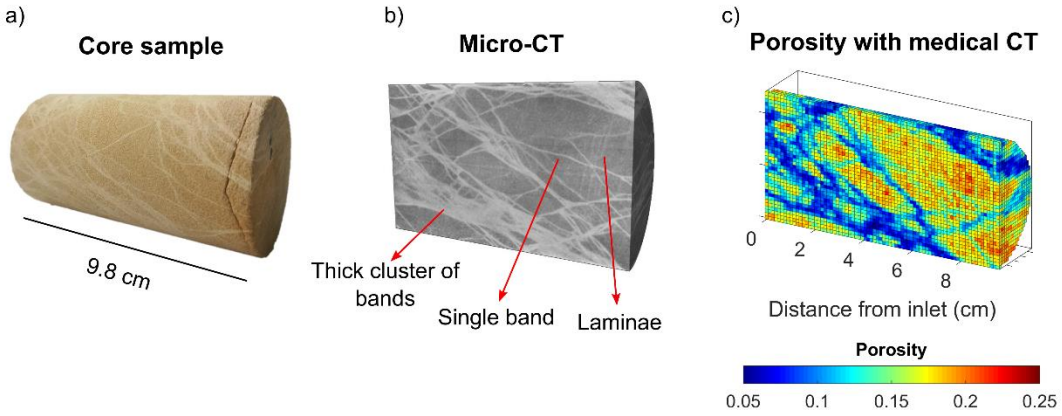

Figure 5-1**.** a) Navajo sandstone core sample characterized by clusters of deformation bands. b) 3D axial view of the sample obtained with micro-CT images. Several images at edges of the micro-CT volume were not taken in account, because affected by geometric unsharpness (penumbra). Voxel size is 0.0275x0.0275x0.0275 mm. c) 3D Porosity distribution of the rock core obtained using dry and water-saturated medical CT images. Voxel size is 1.25x1.25x1.25 mm.

5.2.2. Multiphase core flooding experiments with medical CT scanner

Steady-state capillary pressure experiments (Pini, et al., 2012) were performed on the sample at conditions of 25 °C and 9 MPa, and a confining pressure of 13.4 MPa. A high pressure core flooding experimental setup similar to that reported in other studies is used (Perrin & Benson, 2010; Krevor, et al., 2012; Hingerl, et al., 2016; Minto, et al., 2017; Ni, et al., 2019)**.** Details of the setup can be found in the section 4.2.4. Due to mechanical failure of one pump, a single syringe pump was used for nitrogen injection rather than a dual (continuous flow) syringe pump system. The rock core was wrapped with heat-shrinkable Teflon, aluminum foil, more heat-shrinkable Teflon, and a rubber sleeve before being placed in an aluminum core holder connected to the core flooding experimental setup. During the experiments, medical X-ray CT images were acquired with the same settings, as specified in section 5.2.1. Pressure at the inlet and outlet of the core was measured by two pressure transducers. Nitrogen was first injected into the core in order to acquire baseline scans of the N_2-saturated rock core at the experimental conditions.

Before injecting the non-wetting fluid into the core, single phase water injection was performed for measuring bulk permeability. Water was injected at

several flow rates in the water-saturated sample and the corresponding pressure drop values across the core were recorded. By applying Darcy's law, a bulk intrinsic permeability of 0.18 md of the entire sample was calculated.

The fluid pair used in the multiphase experiment was N_2 and water. The water was pre-equilibrated with nitrogen for several hours for preventing N_2 dissolution during injection. Multiphase core flooding experiments consisted of injecting 100% N_2 at progressively higher flow rates (0.3, 0.6, 0.8, 1, 2 mL/min) into the initially water-saturated sample. Five pore volumes (PV) of injected fluid are generally considered enough to reach steady-state pressure and saturation conditions (Perrin, et al., 2009). However, in this highly heterogeneous rock sample more than 10 pore volumes (1 PV=26.7 mL) were needed.

Nitrogen saturation within individual voxels ($S_{N_2 i}$) can be estimated using Eq. 5-2 by acquiring several sets of medical X-ray CT images (Akin & Kovscek, 2003).

$$S_{N_2 i} = \frac{CT_{exp_i} - CT_{wat\ sat_i}}{CT_{N2\ sat_i} - CT_{wat\ sat_i}} \tag{5-2}$$

Here CT_{exp_i}, $CT_{wat\ sat_i}$, $CT_{N2\ sat_i}$ are scan images at experimental, fully water-saturated and fully N_2-saturated conditions, respectively. Once steady state conditions were reached for each injection flow rate, at least two sets of images were acquired and averaged to reduce the random error in the CT measurements (Pini, et al., 2012). Images were coarsened, up to a resolution of 1.25 mm in the xyz plane, for further noise reduction, as for the voxel porosity calculation (section 5.2.1). Medical CT images were also taken during transient state conditions during the experiments in order to quantify the dynamic behaviour of N_2 invasion into different compartments of the core. During un-steady state conditions only single CT scans were acquired.

5.3. Experimental results: sealing effect of deformation bands on fluid flow

5.3.1. Sub-core scale N_2 saturation in un-steady and steady state conditions

The first stage of injection was performed by injecting N_2 at 0.3 mL/min. After 50 min of injection at 0.3 mL/min (0.55 PV), some of the compartments near the inlet reach a high N_2 saturation (Figure 5-2a). Migration of the N_2 is characterized by

tortuous connections, rather than the relatively uniform saturation front observed in more homogenous systems. Looking more closely at the two dimensional (2D) cross section, or slice, in the x-y plane, at 1 cm from the inlet, it is noticeable that there remain areas with near zero N_2 saturation (Figure 5-2b, marked with arrow). Due to the low resolution of the medical CT images, it is not easy to relate this effect to a specific rock feature. However, the high-resolution dry micro-CT image of the corresponding slice (Figure 5-2e) provides the structural details necessary to link the zero N_2 saturation area to a thick cluster of anastomosing bands that prevent this region and any enclosed compartments, from becoming saturated.

Slices at 4.12 and 4.6 cm from the inlet provide more evidence of the high degree of tortuosity and complexity of 3D compartments' geometry and connectivity. Higher N_2 saturation is measured in the central compartment of the slice at 4.6 cm from inlet, compared to the one at 4.12 cm (Figure 5-2c, 5-2d). This is because the portion of the rock further away from the inlet is saturated through a flow pathway that originates from the left side, whereas in the slice closer to the inlet, invasion is slower and occurs from the right side. The central compartment of these two slices (Figure 5-2c, 5-2d) is subdivided by a thin deformation band that acts as a capillary barrier, delaying crossflow between the two sub-regions (Figure 5-2g, 5-2h).

At 5.3 cm from inlet, only a few compartments are saturated with N_2 (Figure 5-2e). The areas that maintain high water saturation correspond to host rock regions isolated from the inlet, by thick clusters of bands (Figure 5-2i).

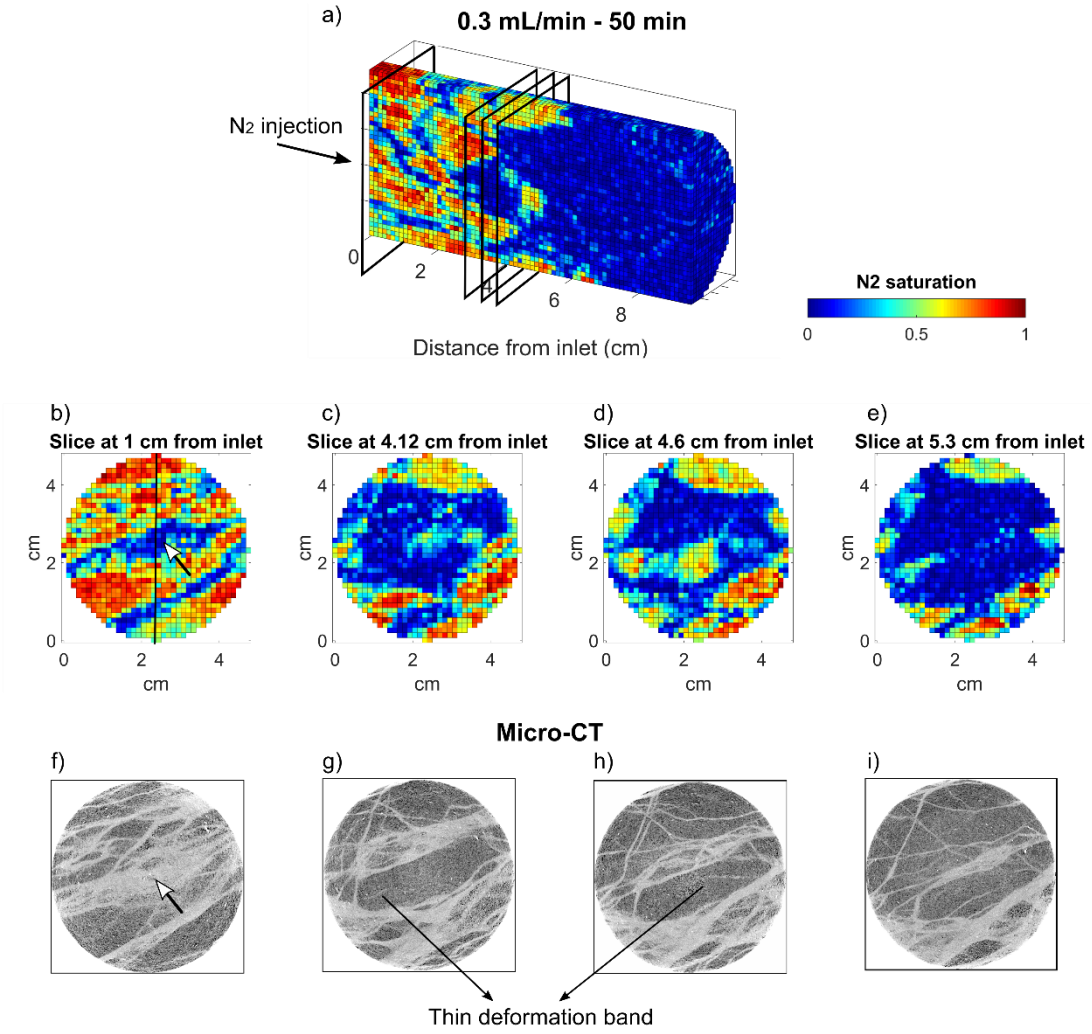

Figure 5-2. a) 3D core axial view of N_2 saturation distribution (N_2 injection from left to right). b) 2D cross section (slice) in the x-y plane at 1 cm from inlet. The vertical line marks the y-z plane cut of the Figure 5-2a. Arrow marks very low saturation area. c) Slice in the x-y plane at 4.12 cm from inlet. d) Slice in the x-y plane at 4.12 cm from inlet. e) Slice in the x-y plane at 5.3 cm from inlet. f) Micro-CT image of the Figure 5-2b. Very low saturation area associated to thick cluster of deformation bands and isolated compartments. g) Micro CT image of the Figure 5-2c. Central compartment characterized by a thin deformation band. h) Micro-CT image of the Figure 5-2d. More details of the central compartment and the thin deformation band. i) Micro-CT image of the Figure 5-2e.

Still with an injection rate of N_2 at 0.3 mL/min, as time increases, nitrogen progressively saturates new compartments that were previously water-saturated (Figure 5-3a). After 3 hours (corresponding to 2 PV), N_2 has saturated some compartments near the end of the core. Figure 5-3b shows the temporal evolution of

N_2 saturation for a slice at 5.3 cm from inlet. The x-y plane is characterized by several compartments, three of which are marked with a circle, a rhombus and a square. The first and second of these are separated by a thick anastomosing cluster of bands. The second and third compartments, however, are only subdivided by a single deformation band (Figure 5-2i). Despite this, the most prominent barrier between compartments is the single deformation band, shown in the Figure 5-1b, which has a near-parallel orientation to the flow direction.

At 50 min from injection, only the compartment marked with a circle is partially saturated with N_2. In this compartment very high N_2 saturation is reached after continuously injecting for 80 min (1 PV). This is strong evidence of the sealing capacity of the deformation bands. At 3 hours of injection, N_2 invades the region marked with a rhombus. At this time, portions of the deformation band, that until previously had shown zero N_2 saturation, start to become saturated. This can be explained by the fact that a single band is characterized by several pore throat sizes and entry pressure values. It is likely that some portions of the deformation band with lower entry pressure are saturated earlier, creating new pathways between different compartments. Steady state conditions are reached after more than 15 hours of injection. At this time the compartment marked with a square still remains water-saturated.

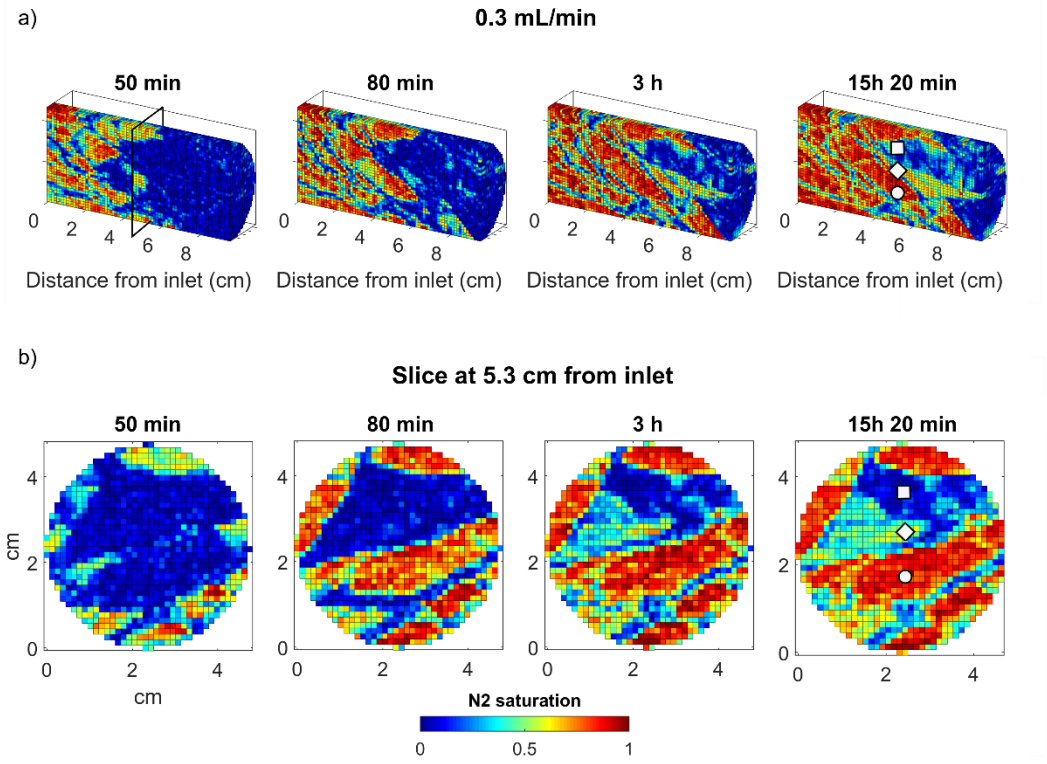

Figure 5-3. a) 3D core axial view of N_2 saturation at several time points until steady-state conditions were reached. The front of the plume is strongly heterogeneous and new compartments are progressively invaded. b) N_2 saturation evolution for the slice at 5.3 from inlet at several time points. Three main compartments are recognized (circle, rhombus, square). The first compartment reaches very high N_2 saturation after 80 min from injection. The second compartment starts being saturated after 3 hours and the third compartment shows very low N_2 saturation even at steady state conditions (15 hours and 20 min). Deformation bands have a strong sealing effect. Portions of bands are progressively saturated, allowing fluid migration across compartments.

Figure 5-4 shows the N_2 saturation distribution at steady state conditions for all (progressively increasing) flow rates. The main change to saturation is seen in the compartment marked with a square in Figure 5-3. The migration of N_2 in this compartment is strongly affected by the fine-grained laminae shown in Figure 5-1b. Very high N_2 saturation characterizes the first half of the rock core even at low flow rates. The thick diagonal cluster that traverses the sample from 3 cm to 8 cm from the inlet, acts as the main capillary barrier in the core. This is illustrated by the upstream accumulation of N_2 behind this cluster. At the highest flow rate of 2 mL/min, with a high differential pressure across the core of 1.8 MPa, two compartments near the outlet still have almost zero N_2 saturation. In the top compartment this behaviour is due to

the presence of a thick cluster of deformation bands. At the end of the experiment, a few other small compartments exhibit very low N_2 saturation. In the micro-CT image these regions, marked with circles in Figure 5-4, are enclosed by multiple bands, with the result that N_2 simply bypasses them. Deformation bands themselves are characterized by low N_2 saturation, with some portions having almost zero N_2 saturation. This is further evidence that pathways are localized onto "weak points" or discontinuities in the bands with lower capillary entry pressure, and that these small breaches are enough to connect compartments and maintain steady state conditions.

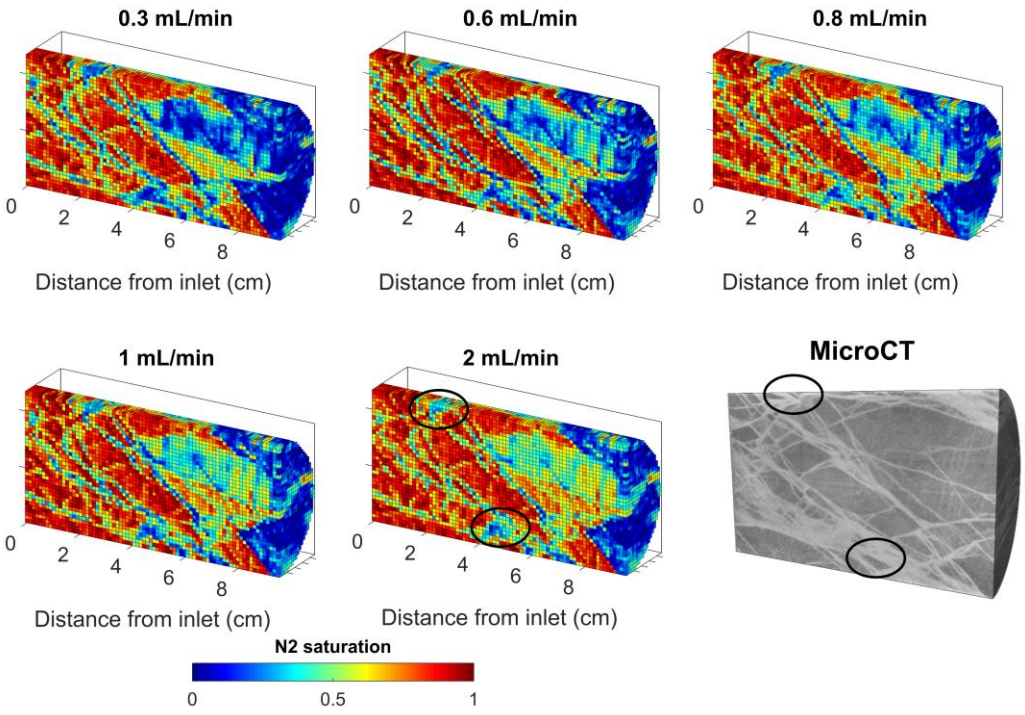

Figure 5-4**.** Snapshot of the 3D axial view of N_2 saturation measured at increased flow rates in steady state conditions. Two compartments towards the outlet of the rock core have almost zero N_2 saturation even at the end of the experiment. Circles mark small compartments bypassed by the flow because they are completely isolated by multiple bands as shown in the micro-CT image.

5.3.2. Evolution of nitrogen migration in single compartments

To understand the temporal evolution in N_2 saturation between compartments, the core was divided into discrete volumes of host rock compartmentalized by deformation bands. Image processing of dry medical X-ray CT scans (which gave the greatest contrast between host rock and deformation band) resulted in 167 such

compartments. For simplicity, only the largest regions are considered, resulting in 12 compartments, each consisting of more than 4000 voxels. Considering that portions of the rock near the inlet reached a very high N_2 saturation immediately on commencing injection, only the compartments placed beyond 2 cm from inlet were considered; this resulted in 7 compartments, which are shown in Figure 5-5a. In each of them the average N_2 saturation in the compartment was calculated over time, using single sets of medical CT images (without averaging between scans); in total, 97 scans were analysed.

The compartments, c_i (i from 1 to 7), are numbered based on the arrival time of the N_2 (Figure 5-5a). Compartments 1 (c1), 2 and 3 begin to be invaded by the non-wetting phase, N_2, from the very first stages of injection and reach a steady-state saturation within five hours (3.4 PV). Compartment 4 reaches very high N_2 saturation before compartments 5 and 6, despite being further from the inlet (Figure 5-5b). This is evidence of the complexity of the 3D flow paths connectivity in the rock.

In compartments 5, 6 and 7, N_2 saturation progressively increases when a higher flow rate, and therefore higher injection pressure, is imposed (Figure 5-5b). At the end of the experiments, the seven analysed compartments exhibit very different final N_2 saturation values. The stepped increases in saturation in these compartments corresponds to temporary peaks in the pressure differential measured across the core (measured with pressure transducers at core inlet and outlet). For each flow rate the delta pressure follows the same trend: it builds up until a maximum value (1.31, 1.31, 1.32, 1.4, and 1.95 MPa) and then decreases and plateaus (Figure 5-5c). The maximum values reached. can be interpreted as pressure threshold values at which N_2 is able to breach a capillary barrier and flow through into a lower saturation region

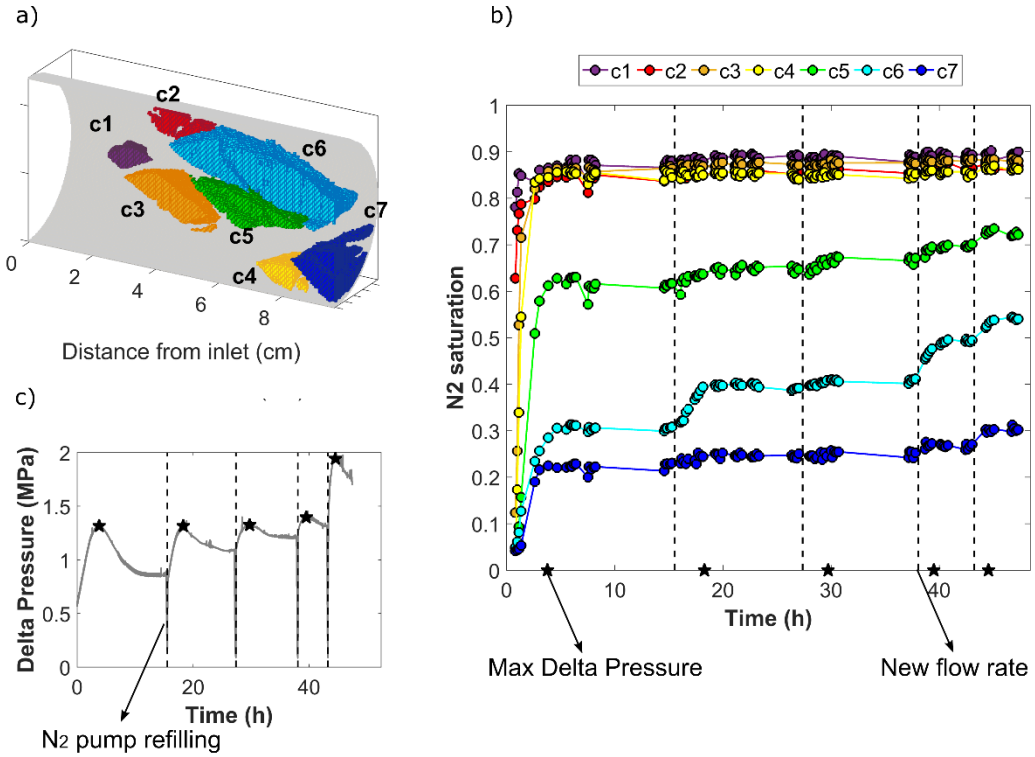

Figure 5-5**.** a) 3D axial view of the seven compartments identified for saturation analysis across the core. They are numerically ordered based on arrival time of N_2. b) Plots of saturation in each compartment for each full-core CT scan (circles). Increase of N_2 saturation in compartments 5, 6 and 7 when new flow rates are imposed (dashed vertical lines). Stepped increases in saturation correspond to maxima in pressure differential (stars). c) Delta pressure profile during the experiments. For each flow rate the same trend is measured: the pressure builds up until a maximum value and then decreases and plateaus. At 1 and 2 ml/min, due to usage of the full volume of N_2 pump, injection was stopped. Steady state conditions may not have been reached. The negative spikes at the end of each flow rate are due to refilling of the N_2 pump.

5.4. Factors influencing compartments' saturation

5.4.1. Model characterization, initial and boundary conditions

Multiphase flow simulations were conducted to better understand how the deformation bands influence fluid flow. For this purpose, the Stanford University General Purpose Research Simulator (GPRS) was used (Cao, 2002; Jiang, 2008; Li, 2011; Boon, et al., 2018; Cao & Aziz, 2002; Krause, 2012; Krause, et al., 2013; Li, et al., 2012; Li & Benson, 2015). Considering the 3D complexity of the core, the aim is not to accurately replicate the experimental results, rather to explore the effects on saturation of the experimental boundary conditions and to understand how discontinuities in the bands may affect the saturation profiles. As a consequence,

simplified 2D models were built for the simulations, using the deformation band geometry shown in Figure 5-6a, each with a grid of 35X78 cells, equivalent to a resolution in the y and z plane of 1.25 mm (the same dimensions as the medical CT scans). Deformation bands (white) discretize the host rock (blue) in 8 compartments. Model cells are categorized as either host rock or deformation band with assigned porosity of 0.16 and 0.07, respectively. Permeability values are estimated using the permeability-porosity relationship proposed by Torabi et al. (2013). With this, a permeability of 89 md was assigned to the host rock and 0.04 md to the deformation bands.

The capillary pressure curve was calculated by fitting a Brooks-Corey model (Brooks & Corey, 1964) to capillary pressure values measured during the experiments (Figure A7 supporting information). Assuming that in steady state conditions the inlet and outlet pressure correspond to N_2 and water pressure respectively, capillary pressure can be considered equal to the pressure drop across the core (Pini, et al., 2012). The capillary pressure curve is scaled for both the host rock and the deformation bands using a Leverett J-function model and using the individual porosity and permeability for each grid block within the model (Li, 2011). With this scaling method, entry pressure values of 7 kPa and 220 kPa were estimated for the host rock and the deformation bands, respectively. Relative permeability curves are assigned using the Brooks-Corey model. The relative permeability curve is included in Appendix 3 (Figure A8).

The lateral faces of the model had no-flow boundaries and the initial condition was a fully water-saturated core (Figure 5-6a). At the inlet face the N_2 flow rate is assumed to be equal to the total flow rate from the experiments, scaled for the 2D model. In the simulations, N_2 is injected at progressively higher flow rates, following the inflow in the experiment, by placing 'injection wells' into each cell of the inlet slice (Figure 5-6b). At the outlet face the pressure is kept constant at 9 MPa by placing 'production wells' in each cell of the outlet slice. A small reservoir (red) with high porosity and permeability and very low entry pressure (0.02 kPa) is placed on the end of the model. This is done to explore the influence of the capillary end effect on saturation (Figure 5-6a). Capillary end effect occurs in core flooding experiments due

to the abrupt discontinuity in the wetting phase at the interface between the rock core and the outlet cap (Huang & Honarpour, 1998). This commonly leads to a negative trend in non-wetting phase saturation in the sample near the outlet of the core (Pini & Benson, 2013).

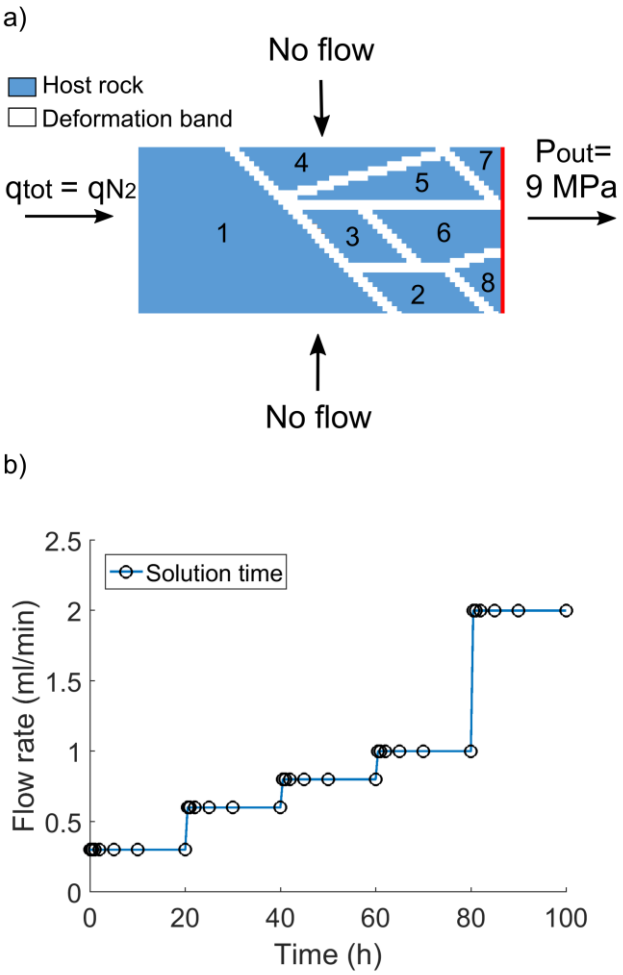

Figure 5-6**.** a) Initial and boundary conditions of the multiphase simulations. The eight host rock compartments are shown in blue, deformation bands in white and the reservoir at the end is in red. b) Injection strategy schematic diagram. Injection progressively at higher flow rates (0.3, 0.6, 0.8, 1, 2 mL/min scaled for the 2D model) and solution at several time (0.16, 0.25, 0.5, 1, 2, 5, 10, 20 hours from the start of each flow rate).

5.4.2. Multiphase fluid flow modeling results

In the first model simulation (Figure 5-7a), saturation increases in the compartment upstream of the first band, which acts as a capillary barrier. The plume has to pass through the band before invading compartments 2, 3, and 4 (see

compartment numbers in Figure 5-6a for reference). After 20 hours of injection at 0.3 mL/min (Figure 5-7b), N_2 saturation reaches very high values in the compartments that are not in contact with the outlet (1 to 5). Deformation bands become more saturated than previously, but still show very low N_2 saturation. The three compartments placed at the outlet (6, 7, 8) are characterized by a decreasing trend in N_2 saturation. This is attributed to the presence of the small reservoir at the end of the model (i.e. the capillary end effect). At the end of the simulation (Figure 5-7c), the decreasing trend due to the capillary end effect dominates the fluid saturation in compartments 6, 7 and 8. The presence of bands towards the outlet (confining compartments 7 and 8) acts to limit the upstream extension of the capillary end effect. It is notable that compartments 2, 3, 4 and 5 have higher saturation than compartment 1, and that fluid compartmentalization happens, regardless of any capillary end effect. The model clearly captures many of the key processes – compartment invasion, end effects and a progressive non-homogeneous saturation front – that were observed in the experiment.

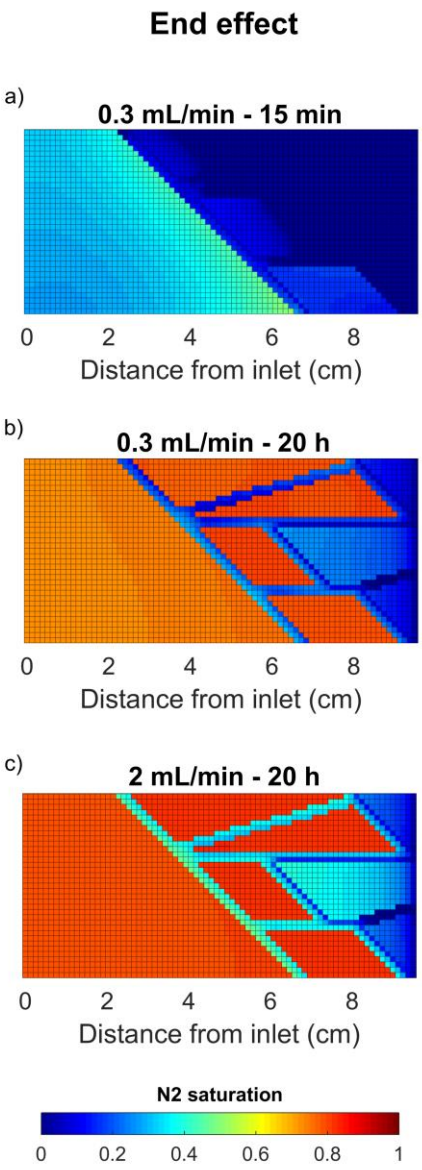

Figure 5-7**.** a) Simulation results of the model with small reservoir at the end (capillary end effect) after 15 min at 0.3 mL/min. The compartment before the band shows nitrogen saturation build up. b) Simulation results after 20 hours of injection at 0.3 mL/min. Negative trend in the compartments at the outlet due to capillary end effect. c) Results at the end of simulation (20 h at 2 mL/min, 100 h total from first injection). Fluid compartmentalization occurs in areas not affected by capillary end effect. Bands closer to the outlet emphasize the capillary end effect in compartment 7 and 8 but limit its spatial extension.

In the second model simulation, discontinuities (holes) were introduced into the deformation bands by assigning host rock petrophysical properties to a cluster of cells in five short sections of the bands (visible as the five gaps in Figure 5-8b). These discontinuities provide pathways for fluids and act to prevent saturation build up in

compartment 1, upstream of the first band. After 20 hours of injection at 0.3 mL/min (Figure 5-8b), N_2 saturation is much lower throughout the core when compared to the previous model simulation (Figure 5-7). Compartments 3, 7 and 8 show zero N_2 saturation and are completely bypassed by flow because of the presence of the discontinuities. A negative trend in saturation, due to the capillary end effect, can be seen in the central compartment in contact with the outlet (compartment 5-6). At the end of the simulation (Figure 5-8c), N_2 saturation has increased in all host rock regions, with the exception of compartments 3, 7 and 8 that are still by-passed by the N_2 and have zero N_2 saturation. The overall N_2 saturation in this model is lower than in the previous one.

These simulation results suggest that discontinuities in the bands can reduce the buildup of pressure and nitrogen saturation in the host rock upstream of the deformation bands. By comparison, a combination of discontinuities in the bands with low entry pressure and the capillary end effect may explain the very low saturation in the bottom compartment at the outlet of the experimental core (Figure 5-4).

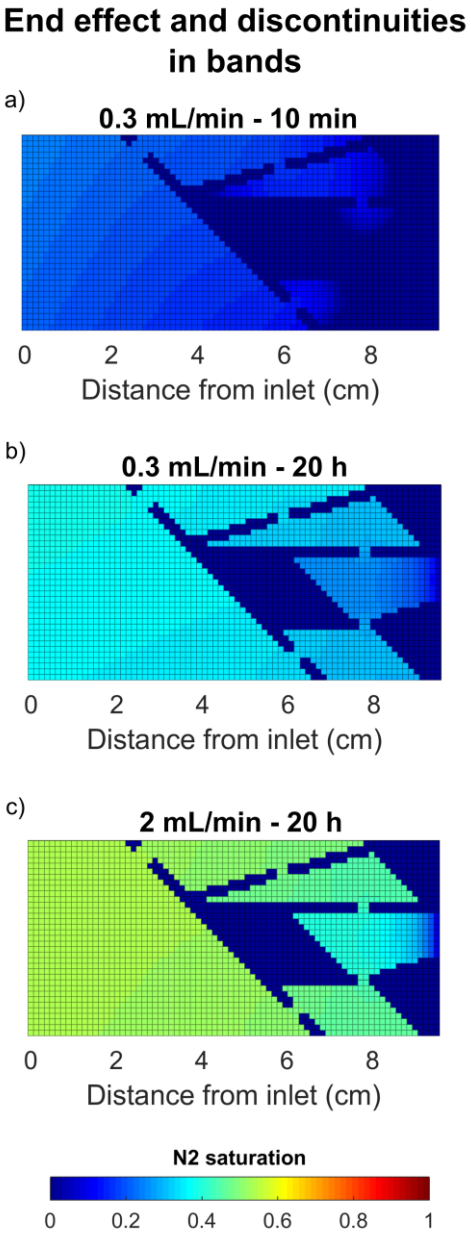

Figure 5-8**.** a) Simulation results of the model with capillary end effect and discontinuities in the bands after 10 min at 0.3 mL/min. The order in which compartments are invaded differs from the first model. b) Simulation results after 20 hours of injection at 0.3 mL/min. Bands, compartment 3, 7 and 8 are by-passed. c) Simulation results at the end of simulation (20 h at 2 mL/min, 100 h total from first injection). Bands, compartment 3 ,7 and 8 are still by-passed. Lower N_2 saturation compared to the first model.

5.5. Impact of deformation band clusters on two-phase flow

The effect of clusters of deformation bands on two-phase fluid flow has been visualized *in situ* and analysed in this study. Clusters of deformation bands strongly

increase the structural complexity and 3D anisotropy of high porosity sandstone reservoirs. They subdivide the host rock into multiple compartments that are not easy to geometrically define in 3D. Due to their mechanism of formation, cataclastic bands are characterized by reduced porosity and permeability and a higher capillary entry pressure when compared to the host rock. In the case of deformation band clusters, the sealing effect on flow is more marked compared to either the laminae, or a single cataclastic band, and, as a result, fluid compartmentalization is pronounced.

Cumulative thickness of the bands and their orientation are important factors influencing fluid migration through the rock. Thick clusters of bands contribute to pressure build up and saturation increase of injected non-wetting fluid in the host rock portions behind the bands. If compartments are enclosed in thick clusters of bands, it is likely that they will never be invaded even when submitted to a high differential pressure. A thin single deformation band, oriented subparallel to the flow direction, still inhibits crossflow between compartments.

When compartments are invaded, breaching commonly occurs through a small portion of the band. This may be governed by discontinuities in the band network, or by varying petrophysical properties within the band itself, resulting in sections with lower capillary entry pressures, locally. This potentially leaves the remaining portions of the bands unsaturated and can create new tortuous flow paths that bypass entire compartments (as shown in Figure 5-8). Clearly, it may not be sufficient to assign a single set of petrophysical properties to the entire band for simulating their effect on fluid flow. Instead, a stochastic approach may be more appropriate.

Several studies have discussed that reservoir compartmentalization due to the presence of deformation bands may never happen. Tindall (2006) highlighted that deformation bands act as “stiff mechanical layers”, that develop joints with spacing linearly related to the mean thickness of deformation bands. The joints represent potential fluid pathways, connecting high porosity and permeability regions and bypassing the low porosity and permeability deformation band zone. In this study, a thick cluster of bands (cb2) crosscuts another cluster of bands (cb1), without developing any joints or fractures (Figure 5-9). Indeed, no joints or fractures are present in the core at all. Hence, for predictive studies it will be important to determine

the geological conditions that are likely to promote such cross-cutting joints and the frequency of their occurrence.

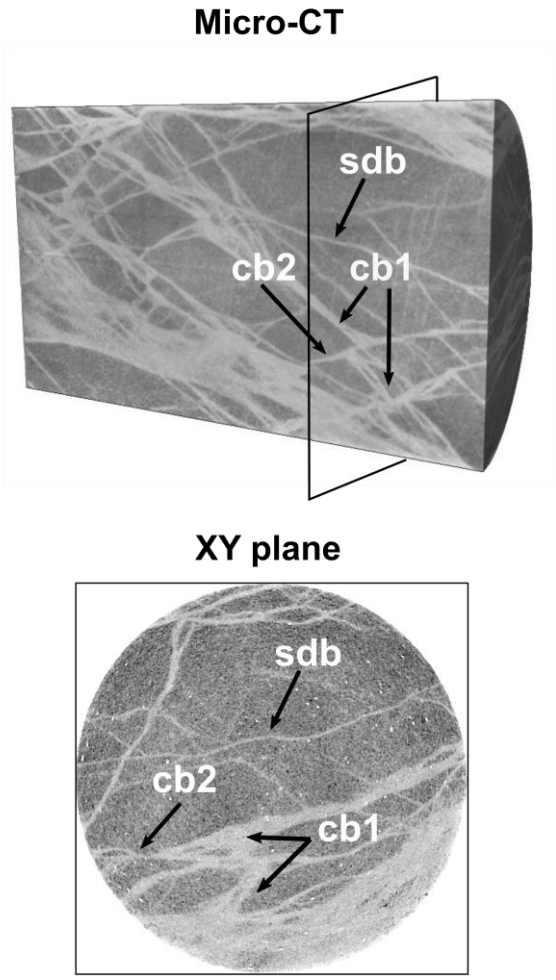

Figure 5-9**.** (top) Axial view of micro-CT images of the rock core. (bottom) Slice corresponding to the xy plane drawn in the top figure. The diagonal cluster of bands marked with cb1 is crosscut by a second cluster cb2. In the xy plane slice is better shown the offset and the difference between clusters and single deformation bands (sdb).

Medeiros et al. (2010) suggest that deformation bands have a limited role in compartmentalization due to their vertically and horizontally limited extension. Whilst this may be true for a single deformation band zone, it is common to find in nature more complex systems characterized by overlapping faults (Childs, et al., 2009; Johansen & Fossen, 2008; Shipton & Cowie, 2001). Large displacement faults can develop adjacent synthetic and antithetic small faults (Berg & Skar, 2005; Bonson, et

al., 2007; Kim, et al., 2004; Torabi, 2014) and in small faults synthetic and antithetic clusters of deformation bands can be found (Johansen & Fossen, 2008; Pontes, et al., 2019; Shipton & Cowie, 2001; Shipton & Cowie, 2003; Shipton, et al., 2005). An example is shown in Figure 5-10a; the photograph is taken from the same field site as the rock core in this study (Shipton, et al., 2002). The main fault, and the surrounding deformation band-dominated damage zone have sub-seismic resolution and the clusters of bands are conjugate. Synthetic and antithetic clusters are apparent at the outcrop (m-cm scale) scale (Figure 5-10b, 5-10c) and at core scale (mm scale) as shown in the core sample used in this study. In addition, in certain circumstances individual layers can become saturated with deformation bands (Fossen & Hesthammer, 1997; Griffiths, et al., 2018; Saillet & Wibberley, 2010).

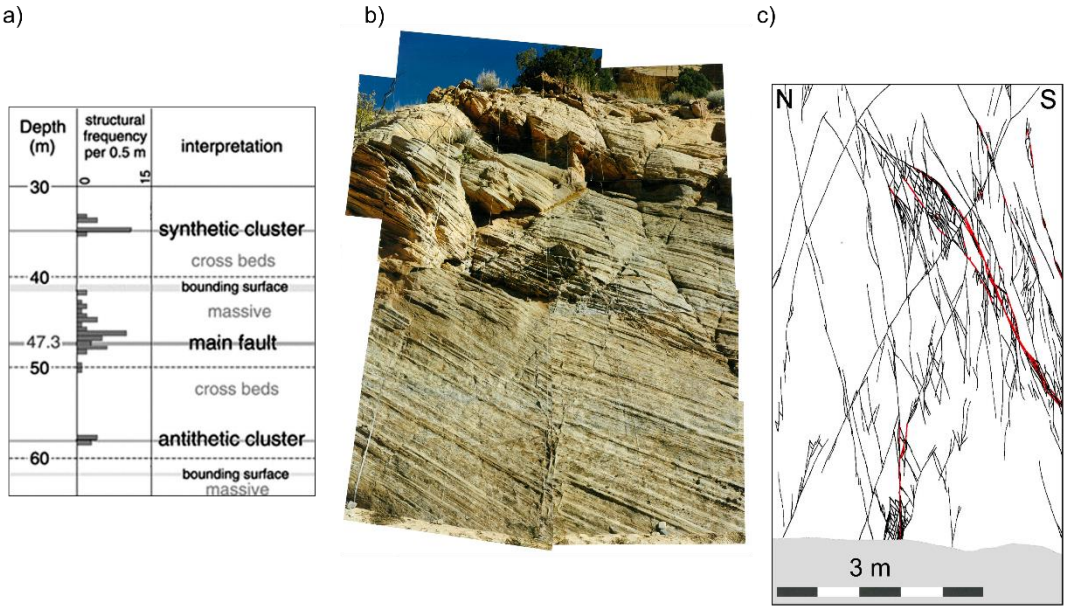

Figure 5-10. a) Structural frequency and interpretation of a borehole through the Big Hole fault, modified from (Shipton, et al., 2002). b) Outcrop of Big Hole Fault damage zone within the bedded Navajo sandstone with synthetic and antithetic deformation bands. The main fault zone, with 8m displacement is off the picture to the left. c) Sketch of the deformation bands (black) and slip surfaces (red) shown in b.

Predicting fluid mobility is hard to achieve due to the sub-seismic nature of deformation bands, and their variable geometry, thickness and orientation. Injection in a reservoir characterized by clusters of deformation bands would likely to fluid compartmentalization and fluid channelling in lozenge-shaped compartments. In the

best-case scenario, where later fractures create connectivity between higher permeability areas, overestimation of potential reservoir capacity will still occur. Additional complications may occur when injecting fluids into deformation bands zones formed in a strike-slip regime. In this case, the lozenge-shaped compartments would likely have a long axis perpendicular to bedding, leading to orthorhombic regions limited in their extent by bed thickness.

To develop realistic geological models for implementation in reservoir modelling, robust estimations of the petrophysical properties of deformation bands and their likely geometric configuration and frequency are required. These can only be derived from outcrop analogues and detailed structural geological studies (fault and fractures logs, micro-structural analysis) (Fox & Bowman, 2010).

5.6. Conclusion

In this study N_2/water drainage capillary pressure experiments were conducted in a sandstone core characterized by diversely oriented clusters of deformation bands. Clusters of deformation bands and single deformation bands subdivide the host rock into several compartments. Results show that N_2 migrates through tortuous pathways and that limited connectivity exists between compartments. Compartments close to the inlet reach very high saturations from the outset of N_2 injection into the fully water-saturated sample. The increase in N_2 saturation is mostly due to the presence of a diagonally oriented thick cluster of bands that traverses the sample and acts as a capillary barrier. The saturation of pores beyond this cluster happens only when N_2 breaches through short sections of the bands. These sections may be linked to discontinuities or to lower capillary entry pressure regions within the bands. Subdivision of one host rock compartment is also caused by a thin single deformation band, oriented parallel to flow. At the end of the experiment, most of the deformation bands themselves and two large compartments towards the outlet of the rock sample remain unsaturated with N_2, even with a high differential pressure (1.95 MPa) across the core. Small compartments enclosed by thick clusters of bands also show low N_2 saturation. A detailed analysis of the temporal evolution of N_2 saturation in individual compartments towards the outlet was conducted. At the end of the experiment, individual compartments retain very different N_2 saturation values. Because of the

complex tortuosity of the network, and the fact that N_2 can travel out of the plane of observation, some compartments at a greater distance from inlet have higher saturations than those that are closer.

Each time the N_2 inflow rate is increased to a new value, the differential pressure across the core rises to a peak. At the peak, additional compartment(s) are invaded and the differential pressure then drops to a new steady value. The peak values are remarkably consistent lying between 1.3MPa and 1.95MPa and likely represent the range of capillary entry pressure values for the deformation band clusters.

Numerical modelling of a simplified 2D representation of the core was conducted to understand the role of experimental conditions and of discontinuities in the bands. Simulations show that the low saturation in compartments close to the outlet is caused by the experimental conditions; commonly termed the capillary end effect. The introduction of discontinuities in some of the modelled bands increased the likelihood of individual compartments being entirely by-passed and remaining at zero saturation, as observed in the experiment.

This research highlights the potential for deformation bands to act as extreme capillary barriers and to result in reservoir fluid compartmentalization. A potential CO_2 or oil reservoir may be characterized by synthetic and antithetic sub seismic faults with associated synthetic and antithetic clusters of deformation bands. A detailed statistical characterization of petrophysical band properties and band geometries is required, at a reservoir scale, to improve probabilistic models of reservoir storage predictions.

Chapter 6

DISCUSSION, CONCLUSIONS AND FUTURE WORK

6.1. Discussion and conclusions

In this study the influence of individual and clusters of deformation bands on fluid flow were investigated at sub-core scale. Previous core flooding experiments identified the importance of small-scale heterogeneities on fluid flow using both single and multiphase fluids. These characterization approaches have not previously been performed on highly heterogeneous sandstones, with flow behaviour dominated by deformation bands.

The internal structure of the samples was investigated with X-ray micro-CT images. As highlighted in Chapter 3, the quality of the image, and the subsequent quantification of petrophysical properties, are dependent on the ability to remove image artefacts. Given the lack of an automatic and efficient correction technique for the beam hardening artefact, a new approach was developed in this study. The correction method consists of a post-processing linearization of the beam hardening curve. The method works for cylindrical or near-cylindrical shapes, homogeneous and heterogeneous material, and it is implemented in an open source code to run in ImageJ, available for download at the permanent DOI:10.15129/2fb54088-1187-48f2-832b-ef76cf5e7bc1.

Micro-CT images were used for investigating the geometry of deformation bands not visible to the naked eye, without compromising the integrity of the core samples. The rock core presented in Chapter 4 (Figure 4-1a) appeared by sight to be characterized by a single diagonal deformation band, however, in the micro-CT images it was apparent that several anastomosing bands are present towards the outlet (Figure 4-1). Moreover, as shown in Chapter 5, micro-CT imaging was extremely valuable for addressing the heterogeneous N_2 saturation distribution as a function of specific rock

features. These features were not visible using the lower resolution medical X-ray CT scanner.

Single and multiphase flow experiments were conducted on a rock core characterized by a simple system of diagonal deformation bands traversing the length of the sample. The deformation bands did not isolate any portion of rock to fluid flow, but they subdivided the host rock into two main compartments, above and below the bands. The compartment above the bands had a reduced cross-sectional area towards the outlet, while the compartment below the bands had a reduced cross-sectional area towards the inlet. PET images acquired over time during radiotracer injection indicated that, while sub-vertical laminae had no effect on flow, deformation bands strongly influenced radiotracer distribution. The presence of the deformation bands and consequent geometry of the two compartments, led to a delayed arrival time and lower fluid velocity caused by the specific geometries of the compartments. The compartment below the bands, for example, is characterized by an increasing cross-sectional area towards the outlet and hence, according to the principle of continuity, as the flow rate is held constant, the velocity decreases toward the outlet.

Drainage CO_2/water high pressure core flooding experiments were also performed on the diagonally banded core sample. Experimental results showed that in the multiphase case both laminae and deformation bands act like capillary barriers. High CO_2 saturation, and therefore accumulation of the non-wetting phase was measured in the region upstream of the laminae. However, the effect of laminae on fluid flow disappeared for high flow rates as fluid flow conditions became more viscosity-dominated, as opposed to capillary-dominated. Deformation bands showed very low CO_2 saturation and they minimized cross flow between compartments for all the flow rates at which CO_2 was injected. This led to a reduced CO_2 saturation (shadow zone) in the compartment below the bands, compared to the one above. Numerical simulations of experimental results highlighted that capillary end effects influenced fluid saturation near the outlet. However, further numerical simulations showed that the same fluid behaviour of reduced CO_2 in the compartments below the bands occurred even after numerically accounting for the capillary end effect.

As described in section 2.2.1. and shown in figure 2-3, deformation bands are only able to accommodate a few millimetres of displacement, and therefore in nature, they are likely to be found in conjugate sets and clusters rather than individual bands. Based on this knowledge, the next step in the research focused on investigating fluid flow behaviour due to clusters of cataclastic bands. For this purpose, a multiphase (N_2/water) high pressure experiment was conducted on a sandstone core sample characterized by conjugate deformation band clusters and single deformation bands cross-cutting laminae in the same aeolian Navajo sandstone. As found in previous laboratory studies, along clusters of deformation bands the reduction in porosity is greater than in individual bands. If the minimum calculated porosity along individual bands of the sample, shown in the Chapter 4, was 0.07, along clusters of deformation bands the porosity reached a lower limit of 0.01. This is consistent with previous lab measurements of porosity (Shipton & Cowie, 2001; Shipton, et al., 2002).

The distribution of saturation of the non-wetting fluid was visualized *in situ* during injection of N_2 into the water-saturated core at progressively higher flow rates, in both unsteady and steady state conditions. A thick diagonally oriented cluster of bands traversing the full sample represents an extreme capillary barrier to flow, leading to a build-up in N_2 saturation in the upstream portion. In the study conducted by Krevor et al. (2011) (section 2.4.3), a similar but more subtle effect was attributed to the presence of finer grained bedding planes in sandstone. Crossflow between compartments was also limited by the presence of sub-parallel-to-the-flow single cataclastic bands. Laminae contributed to a variable N_2 saturation, but the overall distribution was governed by the presence of the deformation bands. Steady state conditions were reached after more than 10 pore volumes injected, as opposed to the 5 pore volumes typically required for more homogeneous rocks, such as the one studied in the Chapter 4. At the end of the experiment several compartments towards the outlet were characterized by very low N_2 saturation. Both the experimental and simulation results attributed this behaviour to: 1) the presence of thick clusters of bands that isolate entire compartments; 2) the capillary end effect; 3) the presence of weak points or discontinuities in bands. Deformation bands cannot be treated as features characterized by a single set of petrophysical and multiphase flow properties; instead, along a single band, several values of porosity, permeability and capillary entry

pressure can be found. *In situ* saturation images (Figure 5.3) showed that N_2 only passed through portions of bands (weak points) characterized by lower capillary entry pressure; the remaining portions remained saturated with water. Weak points in the bands represent potential pathways, able to connect some compartments and bypass some others. Analysis of the N_2 saturation evolution over time in single regions highlighted that some compartments further from the inlet were saturated with N_2 before compartments closer to the inlet. Pressure drop across the core over time registered a temporary peak followed by a decreasing trend and plateau when steady state conditions were reached. The peaks in pressure (from 1.31 MPa at 0.3 mL/min to 1.95 MPa at 2 mL/min) occurred when a new compartment (bounded by bands) was invaded; therefore, they can be interpreted as the pressure values needed for N_2 to exceed the capillary entry pressure and break through the deformation bands. This behaviour has never been observed in previous experimental studies investigating the role of heterogeneities on fluid flow, because these have focussed on heterogeneities in one plane (bedding).

Drainage multiphase experiments conducted in Chapters 4 and 5 allowed for estimation of capillary entry pressure in the inlet portion of the samples. For the rock core characterized by clusters of bands, the estimated inlet capillary entry pressure was 0.14 MPa, as compared to 2.7 kPa for the individual cataclastic bands sample. Despite fluid compartmentalization occurring in both cases, the effect was significantly intensified when the system was characterized by conjugate bands clusters.

The findings presented in this study improve our understanding of fluid flow behaviour when cataclastic deformation bands occur, by visualizing and quantifying fluid flow *in situ*. These findings are also valuable for providing details on structure, petrophysical, and multiphase properties of deformation bands to be implemented in future upscaled reservoir simulations. While the research was focused at sub-core scale, evidence of the strong influence of deformation bands on fluid flow is ubiquitous in outcrops. For example, Figure 6-1 clearly shows how the migration of oil in Entrada sandstone (Utah) is affected by bedding planes and fractures, but mostly by deformation bands. As shown in the experiments -with different fluid pairs-

deformation bands impede further migration of oil, leaving some compartments completely unsaturated.

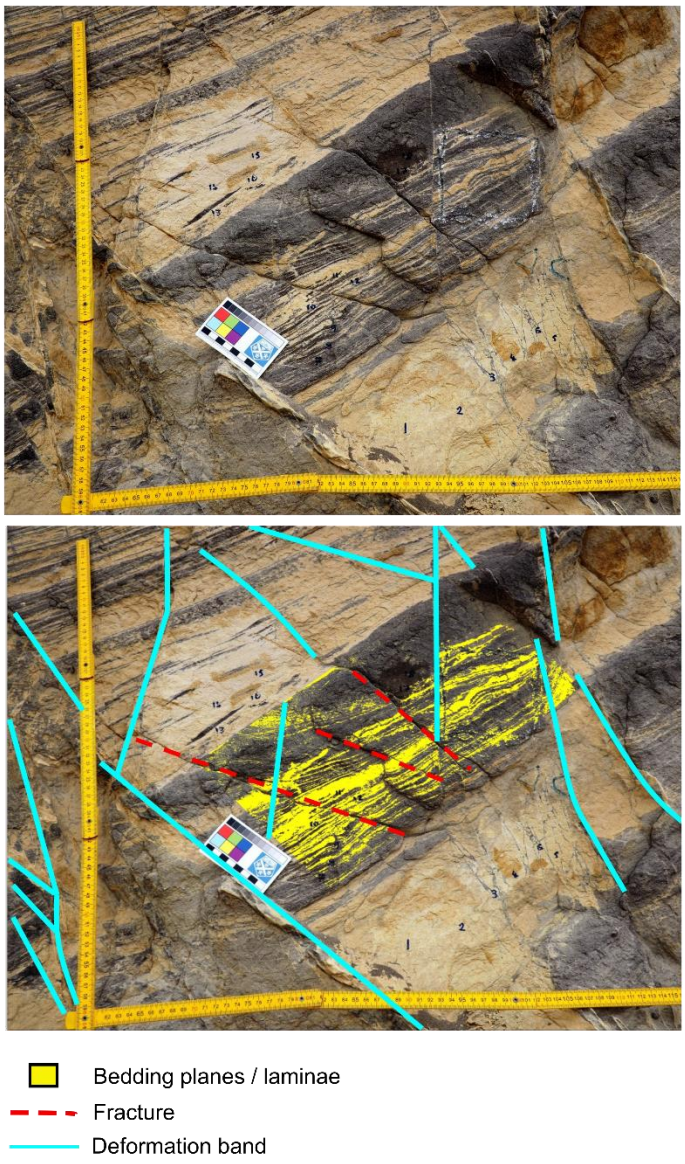

Figure 6-1. Outcrop of Entrada Sandstone in Utah. Bedding planes and laminae (yellow), fractures (red dashed line) and deformation bands (light blue line) affected past oil migration in the reservoir.

Figure 6-1 illustrates how deformation bands may lead to fluid compartmentalization, and result in shadows or unsaturated zones, regardless of the scale. The presence of later fractures may connect high porosity and permeability regions, bypassing deformation band zones and reducing fluid compartmentalization.

However, even this latter scenario would still lead to an overestimation of potential storage.

Overall, deformation bands are shown to have a strong influence on fluid mobility and injectivity strategies for subsurface engineering projects using multiphase fluids, such as geologic carbon dioxide storage. Unexpected pressure buildup due to the presence of fluid barriers may be reduced by lowering injection flow rates. However, this means that, in order to store the volume initially estimated for the project, greater time and cost will be needed. Further, fluid channeling in lozenge-shaped bodies enclosed by deformation bands may lead to unexpected and undetected fluid migration pathways. These impacts imply that more data, monitoring wells and characterization resources may be required for lowering uncertainties on fluid migration.

Implementation of deformation bands structures and their petrophysical and multiphase properties in reservoir modelling is essential for accurate reservoir characterization and project management. However, prediction of the presence of deformation bands in reservoirs remains extremely challenging. As stated in section 2.2, deformation bands form in highly porous sandstones, accommodating fault displacement. Cataclastic deformation bands form in all tectonic regimes, but they are mostly found in proximity to faults in damage zones. Band frequency can be estimated based on the distance to the fault; conjugate clusters of deformation bands and enhanced permeability reduction are found closer to the fault core. However, deformation bands are not only found in large displacement fault zones, but also in small (< 10 m offset), and not seismically resolvable, fault zones. For example, both the rock cores, with individual and clusters of bands, analyzed in Chapters 4 and 5, are taken from an 8 m displacement fault. They can also be found through individual beds (Fossen & Hesthammer, 1997; Griffiths, et al., 2018; Saillet & Wibberley, 2010). Considering that no relationship exists in the literature between band frequency and the magnitude of fault displacement, the same numbers of deformation bands may be found associated with both small and large displacement structures. If the fault core and damage zone are all below seismic resolution, prediction of bands in potential

reservoir needs to be determined by detailed structural geology studies, well log data, and outcrop analogues.

6.2. Future work

6.2.1. Upscaling field models

Based on the findings of this study that deformation bands have a strong influence on fluid flow, future work should focus on effectively upscaling deformation bands properties, understanding deformation band geometries and integrating them into reservoir simulation models. A realistic 3D description of deformation band geometry is included in the study of Qu et al. (2017). However, the same study also highlighted how the upscaling method of coarsening petrophysical and multiphase properties fails when fluid is forced to migrate through deformation band zones. Results produced by a finer scale model differ from the upscaled model. Conceptually it is the same phenomenon as shown in Figure 5-1, where the single deformation band, clearly visible in the micro-CT images, is almost invisible in the porosity distribution derived from lower resolution images (medical X-ray scanner). Moreover, as shown in the Chapter 5, discontinuities or low capillary entry sections of the deformation bands strongly affect fluid mobility. Deformation bands should hence be treated in reservoir modelling as heterogeneous systems and not characterized by a single porosity, permeability and capillary pressure value. A good compromise between accuracy of geometry and properties of the bands and computational time needs to be found.

6.2.2. Residual trapping during imbibition

Several studies showed that capillary heterogeneities enhance the residual trapping mechanism in a CO_2/water system. Residual trapping consists of immobilizing ganglia of CO_2 in pore space when water flooding follows CO_2 flooding. This happens during gravity and capillary-driven plume equilibration following CO_2 injection in saline aquifer formations. The drainage experiments shown in this study were followed by imbibition experiments, where 100% water was injected in the core sample after 100% CO_2 or N_2 injection. Hence, the initial stage of the imbibition process corresponds to the final stage of the drainage. Further analysis of such

experimental data will be carried out in the future for understanding the trapping potential of deformation bands.

6.2.3. Reactivity of calcite minerals with supercritical CO_2 and water

Under geological sequestration conditions, supercritical CO_2 dissolves in water and carbonic acid is produced (Kutchko, et al., 2007). Carbonic acid dissolves carbonate minerals, that are often present in host rock cement and along cementation bands. Dissolution of carbonate minerals may create secondary porosity and drastically change fluid flow behaviour. Core flooding experiments could be conducted injecting supercritical CO_2 in sandstone characterized by either carbonate cement or cemented deformation bands.

6.2.4. Effect of stress conditions, mineralogical content and cementation on development of deformation bands

It is still not clear which stress conditions favour the formation of deformation bands rather than fractures and what the role of host rock cementation and matrix mineralogy play on band formation. Controlled laboratory deformation experiments could be conducted on quartz and feldspar sandstones characterized by different cement nature and content. This would be useful for better prediction of the presence of deformation bands in a potential reservoir based on host rock characteristics.

Bibliography

Achterhold, K. et al., 2013. Monochromatic computed tomography with a compact laser-driven X-ray source. *Scientific reports,* Volume 3, p. 1313.

Ader, J. C. & Stein, M. H., 1984. Slaughter estate unit tertiary miscible gas pilot reservoir description. *Journal of petroleum technology,* Volume 36(05), pp. 837-845.

Akbarabadi, M. & Piri, M., 2013. Relative permeability hysteresis and capillary trapping characteristics of supercritical CO2/brine systems: An experimental study at reservoir conditions. *Advances in Water Resources,* Volume 52, pp. 190-206.

Akin, S. & Kovscek, A. R., 2003. Computed tomography in petroleum engineering research. *Geological Society, London, Special Publications,* Volume 215(1), pp. 23-38.

Alemu, B. L. et al., 2013. Effect of sub-core scale heterogeneities on acoustic and electrical properties of a reservoir rock: a CO2 flooding experiment of brine saturated sandstone in a computed tomography scanner. *Geophysical Prospecting,* Volume 61(1), pp. 235-250.

Antonellini, M. A. & Pollard, D. D., 1995. Distinct element modeling of deformation bands in sandstone. *Journal of structural Geology,* Volume 17(8), pp. 1165-1182.

Antonellini, M. & Aydin, A., 1994. Effect of faulting on fluid flow in porous sandstones: petrophysical properties. *AAPG bulletin,* Volume 78(3), pp. 355-377.

Antonellini, M. & Aydin, A., 1995. Effect of faulting on fluid flow in porous sandstones: geometry and spatial distribution. *AAPG bulletin,* Volume 79(5), pp. 642-670.

Antonellini, M., Aydin, A., Pollard D. D., 1994. Microstructure of deformation bands in porous sandstones at Arches National Park, Utah. *Journal of structural geology*, 16(7), 941-959.

Aydin, A., 1978. Small faults formed as deformation bands in sandstone. *Rock Friction and Earthquake Prediction,* pp. 913-930.

Aydin, A., Borja, R. I. & Eichhubl, P., 2006. Geological and mathematical framework for failure modes in granular rock. *Journal of Structural Geology,* Volume 28(1), pp. 83-98.

Aydin, A. & Johnson , A. M., 1978. Development of faults as zones of deformation bands and as slip surfaces in sandstone. *Pure and applied Geophysics,* Volume 116(4-5), pp. 931-942.

Bachu, S. & Bennion, D. B., 2009. Dependence of CO2-brine interfacial tension on aquifer pressure, temperature and water salinity. *Energy Procedia,* Volume 1(1), pp. 3157-3164.

Ballas, G., Fossen, H. & Soliva, R., 2015. Factors controlling permeability of cataclastic deformation bands and faults in porous sandstone reservoirs. *Journal of Structural Geology,* Volume 76, pp. 1-21.

Ballas, G. et al., 2013. Shear-enhanced compaction bands formed at shallow burial conditions; implications for fluid flow (Provence, France). *Journal of Structural Geology,* Volume 47, pp. 3-15.

Benson, S. & Cook, P., 2005. *Chapter 5: Underground geological storage,* Interlachen, Switzerland: IPCC Special Report on Carbon Dioxide Capture and Storage, Intergovernmental Panel on Climate Change.

Berg, S. S. & Skar, T., 2005. Controls on damage zone asymmetry of a normal fault zone: outcrop analyses of a segment of the Moab fault, SE Utah. *Journal of Structural Geology,* Volume 27(10), pp. 1803-1822.

Biguri, A., Dosanjh, M., Hancock, S. & Soleimani, M., 2016. TIGRE: a MATLAB-GPU toolbox for CBCT image reconstruction. *Biomedical Physics and Engineering Express,* 2(5).

Bjørlykke, K. & Jahren, J., 2010. Sandstones and sandstone reservoirs. *Petroleum Geoscience,* Issue Springer, Berlin, Heidelberg, pp. 113-140.

Bloomfield, J., Gooddy, D., Bright, M. & Williams, P., 2001. Pore-throat size distributions in Permo-Triassic sandstones from the United Kingdom and some implications for contaminant hydrogeology. *Hydrogeology Journal,* Volume 9(3), pp. 219-230.

Bonson, C. G. et al., 2007. Geometric and kinematic controls on the internal structure of a large normal fault in massive limestones: the Maghlaq Fault, Malta. *Journal of Structural Geology,* Volume 29(2), pp. 336-354.

Boon, M., Ni, H., Garing, C. & Benson, S. M., 2018. *Effect of Capillary Induced Flow on Co2 Residual Trapping.* Melbourne, 14th Greenhouse Gas Control Technologies Conference, pp. 21-26.

Bright, A., 2006. *Deformation band fault core: character, evolution and influence on bulk fluid flow*, Dublin: (Doctoral dissertation, Trinity College Dublin).

Brooks, R. A. & Di Chiro, G., 1976. Beam hardening in x-ray reconstructive tomography. *Physics in medicine & biology,* Volume 21(3), p. 390.

Brooks, R. H. & Corey, A. T., 1964. Hydraulic properties of porous media. *Hydrology Papers,Colorado State University*, pp. 22-27.

Brooks, R. H. & Corey, A. T., 1964. Hydraulic properties of porous media. *Hydrology Papers,Colorado State University*, pp. 22-27.

Brown, H. W., 1951. Capillary pressure investigations.. *Journal of Petroleum Technology,* Volume 3(03), pp. 67-74.

Caine, J. S., Evans, J. P. & Forster, C. B., 1996. Fault zone architecture and permeability structure. *Geology,* Volume 24(11), pp. 1025-1028.

Campbell, C. V., 1967. Lamina, laminaset, bed and bedset. *Sedimentology,* Volume 8(1), pp. 7-26.

Cao, H., 2002. *Development of techniques for general purpose simulators,* Doctoral dissertation, Stanford University.

Cao, H. & Aziz, K., 2002. *Performance of IMPSAT and IMPSAT-AIM models in compositional simulation.* In SPE Annual Technical conference and Exhibition, Society of Petroleum Engineers.

Cardwell Jr, W. T. & Parsons, R. L., 1945. Average permeabilities of heterogeneous oil sands. *Transactions of the AIME,* Volume 160(01), pp. 34-42.

Carl, P., 2006. *Radial Profile Extended.* [Online] Available at: https://imagej.nih.gov/ij/plugins/radial-profile-ext.html [Accessed 6 4 2018].

Cashman, S. & Cashman, K., 2000. Cataclasis and deformation-band formation in unconsolidated marine terrace sand, Humboldt County, California. *Geology,* Volume 8(2), pp. 111-114.

Chadwick, R. A. et al., 2004. Geological reservoir characterization of a CO2 storage site: The Utsira Sand, Sleipner, northern North Sea. *Energy,* Volume 29(9-10), pp. 1371-1381.

Chandler, M. A., Kocurek, G., Goggin, D. J. & Lake, L. W., 1989. Effects of stratigraphic heterogeneity on permeability in eolian sandstone sequence, Page Sandstone, northern Arizona. *AAPG Bulletin,* Volume 73(5), pp. 658-668.

Childs, C. et al., 2009. A geometric model of fault zone and fault rock thickness variations. *Journal of Structural Geology,* Volume 31(2), pp. 117-127.

Chiquet, P., Daridon, J. L., Broseta, D. & Thibeau, S., 2007. CO2/water interfacial tensions under pressure and temperature conditions of CO2 geological storage. *Energy Conversion and Management,* Volume 48(3), pp. 736-744.

Chityala, R., Hoffmann, K. R., Rudin, S. & Bednarek, D. R., 2005. Region of interest (ROI) computed tomography (CT): comparison with full field of view (FFOV) and

truncated CT for a human head phantom. *In Medical Imaging 2005: Physics of Medical Imaging,* 5745(International Society for Optics and Photonics), pp. 583-590.

Choi, J. H., Edwards, P., Ko, K. & Kim, Y. S., 2016. Definition and classification of fault damage zones: A review and a new methodological approach. *Earth-Science Reviews,* Volume 152, pp. 70-87.

Cnudde, V. & Boone, M. N., 2013. High-resolution X-ray computed tomography in geosciences: A review of the current technology and applications. *Earth-Science Reviews,* Volume 123, pp. 1-17.

Cnudde, V. et al., 2006. Recent progress in X-ray CT as a geosciences tool. *Applied Geochemistry,* Volume 21(5), pp. 826-832.

Corey, A. T. & Rathjens, C. H., 1956. Effect of stratification on relative permeability. *Journal of Petroleum Technology,* Volume 8(12), pp. 69-71.

Cowie, P. A. & Shipton, Z. K., 1998. Fault tip displacement gradients and process zone dimensions. *Journal of Structural Geology,* Volume 20(8), pp. 983-997.

Cowton, L. R. et al., 2018. Benchmarking of vertically-integrated CO2 flow simulations at the Sleipner Field, North Sea. *Earth and Planetary Science Letters,* Volume 491, pp. 121-133.

Deng, S. et al., 2015. Permeability characterization of natural compaction bands using core flooding experiments and three-dimensional image-based analysis: Comparing and contrasting the results from two different methods. *AAPG Bulletin,* Volume 99(1), pp. 27-49.

Du Bernard, X., Eichhubl, P. & Aydin, A., 2002. Dilation bands: A new form of localized failure in granular media. *Geophysical Research Letters,* Volume 29(24), pp. 29-1..

Edlmann, K. et al., 2016. Lessons learned from using expert elicitation to identify, assess and rank the potential leakage scenarios at the Heletz pilot CO2 injection site. *International Journal of Greenhouse Gas Control,* Volume 49, pp. 473-487.

Eichhubl, P., Hooker, J. N. & Laubach, S. E., 2010. Pure and shear-enhanced compaction bands in Aztec Sandstone. *Journal of Structural Geology.*, Volume 32(12), pp. 1873-1886.

Eiken, O. et al., 2011. Lessons learned from 14 years of CCS operations: Sleipner, In Salah and Snøhvit. *Energy Procedia,* Volume 4, pp. 5541-5548.

Fanchi, J. R., 2002. *Shared Earth Modeling: Methodologies for Integrated Reservoir Simulations.* s.l.:Gulf Professional Publishing.

Feldkamp, L. A., Davis, L. C. & Kress, J. W., 1984. Practical cone-beam algorithm. *Journal of the Optical Society of America A,* 1(6), pp. 612-619.

Fisher , Q. J. & Knipe, R. J., 2001. The permeability of faults within siliciclastic petroleum reservoirs of the North Sea and Norwegian Continental Shelf. *Marine and Petroleum Geology,* Volume 18(10, pp. 063-1081.

Fossen, H., 2010. Deformation bands formed during soft-sediment deformation: observations from SE Utah. *Marine and Petroleum Geology,* Volume 27(1), pp. 215-222.

Fossen, H. & Hesthammer, J., 1997. Geometric analysis and scaling relations of deformation bands in porous sandstone. *Journal of Structural Geology*, Volume 19(12), pp. 1479-1493.

Fossen, H., Schultz, R. A., Shipton, Z. K. & Mair, K., 2007. Deformation bands in sandstone: a review. *Journal of the Geological Society,* Volume 164(4), pp. 755-769.

Fossen, H., Schultz, R. A. & Torabi, A., 2011. Conditions and implications for compaction band formation in the Navajo Sandstone, Utah. *Journal of Structural Geology,* Volume 33(10), pp. 1477-1490.

Fossen, H. et al., 2018. A review of deformation bands in reservoir sandstones: geometries, mechanisms and distribution. *Geological Society, London, Special Publications,* Volume 459(1), pp. 9-33.

Fox, R. J. & Bowman, M. B. J., 2010. The challenges and impact of compartmentalization in reservoir appraisal and development. *Geological Society, London, Special Publications,* Volume 347(1), pp. 9-23.

Gainski, M., Macgregor, A. G., Freeman, P. J. & Nieuwland, H. F., 2010. Turbidite reservoir compartmentalization and well targeting with 4D seismic and production data: Schiehallion Field, UK. *Geological Society, London, Special Publications,* Volume 347(1), pp. 89-102.

Garing, C. & Benson, S. M., 2019. CO2 Wettability of Sandstones: Addressing Conflicting Capillary Behaviors. *Geophysical Research Letters,* Volume 46(2), pp. 776-782.

Gershenzon, N. I., Soltanian, M., Ritzi Jr, R. W. & Dominic, D. F., 2014. Influence of small scale heterogeneity on CO2 trapping processes in deep saline aquifers. *Energy Procedia,* Volume 59, pp. 166-173.

Gilbert, P., 1972. Iterative methods for the three-dimensional reconstruction of an object from projections. *Journal of theoretical biology,* 36(1), pp. 105-117.

Gill, C. E., Shepherd, M. & Millington, J. J., 2010. Compartmentalization of the Nelson field, Central North Sea: evidence from produced water chemistry analysis. *Geological Society, London, Special Publications,* Volume 347(1), pp. 71-87..

Glover, P., 2001. *Formation Evaluation MSC course notes,* Aberdeen University.

Grathwohl, P. & Kleineidam, S., 1995. Impact of heterogeneous aquifer materials on sorption capacities and sorption dynamics of organic contaminants. *AHS Publications-Series of Proceedings and Reports-Intern Assoc Hydrological Sciences,* Volume 79-86, p. 225.

Griffiths, J., Faulkner, D. R. & Edwards, A. P., 2018. Deformation band development as a function of intrinsic host-rock properties in Triassic Sherwood Sandstone. *Geological Society, London, Special Publications,* Volume 435(1), pp. 161-176.

Guédon, G. R. et al., 2017. Influence of capillary end effects on steady-state relative permeability estimates from direct pore-scale simulations. *Physics of Fluids,* Volume 29(12), p. 123104.

Hanna, R. D. & Ketcham, R. A., 2017. X-ray computed tomography of planetary materials: A primer and review of recent studies. *Chemie der Erde-Geochemistry,* Volume 77(4), pp. 547-572.

Hansen, O. et al., 2013. Snøhvit: The history of injecting and storing 1 Mt CO2 in the fluvial Tubåen Fm. *Energy Procedia,* Volume 37, pp. 3565-3573.

Herman, G. T., 1979. Correction for beam hardening in computed tomography. *Physics in Medicine & Biology,* Volume 24(1), p. 81.

Hesthammer, J., Bjørkum, P. A. & Watts, L., 2002. The effect of temperature on sealing capacity of faults in sandstone reservoirs: examples from the Gullfaks and Gullfaks Sør fields, North Sea. *AAPG bulletin,* Volume 86(10), pp. 1733-1751.

Hingerl, F. F. et al., 2016. Characterization of heterogeneity in the Heletz sandstone from core to pore scale and quantification of its impact on multi-phase flow. *International Journal of greenhouse gas control,* Volume 48, pp. 69-83.

Hingerl, F. F. et al., 2016. Characterization of heterogeneity in the Heletz sandstone from core to pore scale and quantification of its impact on multi-phase flow. *International Journal of greenhouse gas control,* Volume 48, pp. 69-83.

Huang, D. D. & Honarpour, M. M., 1998. Capillary end effects in coreflood calculations. *Journal of Petroleum Science and Engineering,* Volume 19(1-2), pp. 103-117.

Huo, D. & Benson, S. M., 2016. Experimental investigation of stress-dependency of relative permeability in rock fractures. *Transport in Porous Media,* Volume 113(3), pp. 567-590.

Jenning, J. B., 1987. Capillary pressure techniques: application to exploration and development geology. *AAPG Bulletin,* Volume 71(10), pp. 1196-1209.

Jennings, R. J., 1988. A method for comparing beam-hardening filter materials for diagnostic radiology. *Medical physics,* 15(4), pp. 588-599.

Jiang, Y., 2008. *Techniques for modeling complex reservoirs and advanced wells,* Doctoral dissertation, Stanford University.

Johansen, T. E. S. & Fossen, H., 2008. Internal geometry of fault damage zones in interbedded siliciclastic sediments. *Geological Society, London, Special Publications,* Volume 299(1), pp. 35-56.

Jolley, S. J., Fisher, Q. J. & Ainsworth, R. B., 2010. Reservoir compartmentalization: an introduction. *Geological Society, London, Special Publications,* Volume 347(1), pp. 1-8.

Joseph, P. M. & Spital, R. D., 1981. he exponential edge-gradient effect in x-ray computed tomography. *Physics in medicine and biology,* 26(3), p. 473.

Jovanović, Z., Khan, F., Enzmann, F. & Kersten, M., 2013. Simultaneous segmentation and beam-hardening correction in computed microtomography of rock cores. *Computers and Geosciences,* Volume 56, pp. 142-150.

Kachelrieß, M., Sourbelle, K. & Kalender, W. A., 2006. mpirical cupping correction: A first-order raw data precorrection for cone-beam computed tomography. *Medical physics,* 33(5), pp. 1269-1274.

Ketcham, R. A. & Hanna, R. D., 2014. Beam hardening correction for X-ray computed tomography of heterogeneous natural materials. *Computers & geosciences,* Volume 67, pp. 49-61.

Kim, K. Y. et al., 2018. Two-phase flow visualization under reservoir conditions for highly heterogeneous conglomerate rock: A core-scale study for geologic carbon storage. *Scientific reports,* Volume 8(1), p. 4869.

Kim, Y. S., Peacock, D. C. & Sanderson, D. J., 2004. Fault damage zones. *Journal of structural geology,* Volume 26(3), pp. 503-517.

Knipe, R. J. et al., 1997. Fault seal analysis: successful methodologies, application and future directions. *Norwegian Petroleum Society Special Publications,* Volume 7, pp. 15-38.

Krause, M. H., 2012. *Modeling and investigation of the influence of capillary heterogeneity on relative permeability.* In SPE Annual Technical Conference and Exhibition, Society of Petroleum Engineers.

Krause, M., Krevor, S. & Benson, S. M., 2013. A procedure for the accurate determination of sub-core scale permeability distributions with error quantification. *Transport in porous media,* Volume 98(3), pp. 565-588.

Krevor, S. et al., 2015. Capillary trapping for geologic carbon dioxide storage–From pore scale physics to field scale implications. *International Journal of Greenhouse Gas Control,* Volume 40, pp. 221-237.

Krevor, S. C., Pini, R., Li, B. & Benson, S. M., 2011. Capillary heterogeneity trapping of CO2 in a sandstone rock at reservoir conditions. *Geophysical Research Letters,* Volume 38(15).

Krevor, S. C., Pini, R., Zuo, L. & Benson, S. M., 2012. Relative permeability and trapping of CO2 and water in sandstone rocks at reservoir conditions. *Water Resources Research,* Volume 48(2).

Krevor, S. C., Pini, R., Zuo, L. & Benson, S. M., 2012. Relative permeability and trapping of CO2 and water in sandstone rocks at reservoir conditions. *Water Resources Research,* Volume 48(2).

Kruth, J. P. et al., 2011. Computed tomography for dimensional metrology. *CIRP Annals-Manufacturing Technology,* 60(2), pp. 821-842.

Kutchko, B. G. et al., 2007. Degradation of well cement by CO2 under geologic sequestration conditions. *Environmental science & technology,* Volume 41(13), pp. 4787-4792.

Kyle, J. R. & Ketcham, R. A., 2015. Application of high resolution X-ray computed tomography to mineral deposit origin, evaluation, and processing. *Ore Geology Reviews,* Volume 65, pp. 821-839.

Labaume, P., Sheppard, S. M. & Moretti, I., 2001. Fluid flow in cataclastic thrust fault zones in sandstones, Sub-Andean Zone, southern Bolivia. *Tectonophysics,* Volume 340(3-4), pp. 141-172.

Lager, A. et al., 2008. Low salinity oil recovery-an experimental investigation1. *Petrophysics,* 49(1).

Lechuga, L. & Weidlich, G. A., 2016. Cone Beam CT vs. Fan Beam CT: A Comparison of Image Quality and Dose Delivered Between Two Differing CT Imaging Modalities. *Cureus,* 8(9).

Leveille, G. P. et al., 1997. Compartmentalization of Rotliegendes gas reservoirs by sealing faults, Jupiter Fields area, southern North Sea. *Geological Society, London, Special Publication,* Volume 123(1), pp. 87-104..

Li, B., 2011. *Including fine-scale capillary heterogeneity in modeling the flow of CO2 and brine in reservoir cores,* Doctoral dissertation, Stanford University.

Li, B. & Benson, S. M., 2015. Influence of small-scale heterogeneity on upward CO2 plume migration in storage aquifers. *Advances in Water Resources,* Volume 83, pp. 389-404.

Li, B., Benson, S. M. & Tchelepi, H. A., 2012. *Modeling fine-scale capillary heterogeneity in multiphase flow of CO2 and brine in sedimentary rocks.* University of Illinois at Urbana-Champaign, IL, USA, Proceedings of the XIX International Conference on Water Resources.

Li, C. H. & Lee, C. K., 1993. Minimum cross entropy thresholding. *Pattern recognition ,* 26(4), pp. 617-625.

Li, Y. et al., 2019. Investigation of the Dynamic Capillary Pressure during Displacement Process in Fractured Tight Rocks. *AIChE Journal.*

Lunn, R. J., Shipton, Z. K. & Bright, A. M., 2008. How can we improve estimates of bulk fault zone hydraulic properties?. *Geological Society, London, Special Publications,* Volume 299(1), pp. 231-237.

Malik, Q. M. & Islam, M. R., 2000. *CO2 Injection in the Weyburn field of Canada: optimization of enhanced oil recovery and greenhouse gas storage with horizontal wells.* In SPE/DOE improved oil recovery symposium, Society of Petroleum Engineers.

Manitoba, U. o., 2018. *Micro-PET Overview - The Origin of the PET Signal.* [Online] Available at: http://umanitoba.ca/faculties/health_sciences/medicine/units/cacs/sam/micro_pet/8125.html
[Accessed 8 10 2019].

Manzocchi, T., Heath, A. E., Walsh, J. J. & Childs, C., 2002. The representation of two phase fault-rock properties in flow simulation models. *Petroleum Geoscience,* Volume 8(2), pp. 119-132.

Ma, X. & Haimson, B. C., 2016. Failure characteristics of two porous sandstones subjected to true triaxial stresses. *Journal of Geophysical Research: Solid Earth,* Volume 121(9), pp. 6477-6498.

McGrath, A. G. & Davison, I., 1995. Damage zone geometry around fault tips. *Journal of Structural Geology,* Volume 17(7), pp. 1011-1024.

Medeiros, W. E. et al., 2010. Evidence of hydraulic connectivity across deformation bands from field pumping tests: two examples from Tucano Basin, NE Brazil. *Journal of Structural Geology,* Volume 32(11), pp. 1783-1791.

Medina, C. R., Rupp, J. A. & Barnes, D. A., 2011. Effects of reduction in porosity and permeability with depth on storage capacity and injectivity in deep saline aquifers: A case study from the Mount Simon Sandstone aquifer. *International journal of greenhouse gas control,* Volume 5(1), pp. 146-156.

Mees, F., Swennen, R., Van Geet, M. & Jacobs, P., 2003. Applications of X-ray computed tomography in the geosciences. *Geological Society, London, Special Publications,* Volume 215(1), pp. 1-6.

Mezzomo, R. F., Luvizotto, J. M. & Palagi, C. L., 2001. Improved oil recovery in Carmópolis field: R&D and field implementations. *SPE Reservoir Evaluation & Engineering,* Volume 4(01), pp. 4-10.

Milkov, A. V. et al., 2007. Compartmentalization and time-lapse geochemical reservoir surveillance of the Horn Mountain oil field, deep-water Gulf of Mexico. *AAPG bulletin,* Volume 91(6), pp. 847-876.

Minto, J. M., Hingerl, F. F., Benson, S. M. & Lunn, R. J., 2017. X-ray CT and multiphase flow characterization of a 'bio-grouted'sandstone core: The effect of dissolution on seal longevity. *International Journal of Greenhouse Gas Control,* Volume 64, pp. 152-162.

Minto, J. M. et al., 2018. "Microbial Mortar"- restoration of degraded marble structures with microbially induced carbonate precipitation. *Construction and Building Materials,* Volume 180, pp. 44-54.

Mooney, S. J., 2002. Three-dimensional visualization and quantification of soil macroporosity and water flow patterns using computed tomography. *Soil Use and Management,* Volume 18(2), pp. 142-151.

Mooney, S. J., 2002. Three-dimensional visualization and quantification of soil macroporosity and water flow patterns using computed tomography. *Soil Use and Management,* 18(2), pp. 142-151..

Mooney, S. J., Pridmore, T. P. & Helliwell, J. B., 2012. eveloping X-ray computed tomography to non-invasively image 3-D root systems architecture in soil. *Plant and soil,* 352(1-2), pp. 1-22.

Morad, S., Al-Ramadan, K., Ketzer, J. M. & De Ros, L. F., 2010. The impact of diagenesis on the heterogeneity of sandstone reservoirs: A review of the role of

depositional facies and sequence stratigraphy. *AAPG bulletin,* Volume 94(8), pp. 1267-1309.

Naff, R. L., 1990. Arrival times and temporal moments of breakthrough curves for an imperfectly stratified aquifer. *Water Resources Research,* Volume 28(1), pp. 53-68.

Naruk, S. J. et al., 2009. *Naruk, S. J., Wilkins, S., Davies, R., Bikun, J., Uzoh, O., & Jensen, L. (2009, September). Subsurface Observations of Deformation Bands and Their Impact on Hydrocarbon Production within the Holstein Field, Gulf of Mexico, USA.* s.l., 2nd EAGE International Conference on Fault and Top Seals - From Pore to Basin Scale 2009.

Ngwenya, B. T., Elphick, S. C., Main, I. G. & Shimmield, G. B., 2000. Experimental constraints on the diagenetic self-sealing capacity of faults in high porosity rocks. *Earth and Planetary Science Letters,* Volume 183(1-2), pp. 187-199.

Ni, H., Boon, M., Garing, C. & Benson, S. M., 2019. Predicting CO2 residual trapping ability based on experimental petrophysical properties for different sandstone types. *International Journal of Greenhouse Gas Control,* Volume 86, pp. 158-176.

Niu, B., Al-Menhali, A. & Krevor, S. C., 2015. The impact of reservoir conditions on the residual trapping of carbon dioxide in Berea sandstone. *Water Resources Research,* Volume 51(4), pp. 2009-2029.

Ochi, J. & Vernoux, J. F., 1998. Permeability decrease in sandstone reservoirs by fluid injection: hydrodynamic and chemical effects. *Journal of hydrology,* Volume 208(3-4), pp. 237-248.

Odling, N. E. et al., 1999. Variations in fracture system geometry and their implications for fluid flow in fractures hydrocarbon reservoirs. *Petroleum Geoscience,* Volume 5(4), pp. 373-384.

Ogilvie, S. R. & Glover, P. W., 2001. The petrophysical properties of deformation bands in relation to their microstructure. *Earth and Planetary Science Letters,* Volume 193(1-2), pp. 129-142.

Ogilvie, S. R., Orribo, J. M. & Glover , P. W. J., 2001. The influence of deformation bands upon fluid flow using profile permeametry and positron emission tomography. *Geophysical Research Letters,* Volume 28(1), pp. 61-64.

Pasala, S. M., Forster, C. B., Deo, M. & Evans, J. P., 2013. Simulation of the impact of faults on CO 2 injection into sandstone reservoirs. *Geofluids,* Volume 13(3), pp. 344-358.

Pauwels, R., Araki, K., Siewerdsen, J. H. & Thongvigitmanee, S. S., 2014. Technical aspects of dental CBCT: State of the art. *Dentomaxillofacial Radiology,* 44(1).

Perrin, J. C. & Benson, S., 2010. An experimental study on the influence of sub-core scale heterogeneities on CO2 distribution in reservoir rocks. *Transport in porous media,* Volume 82(1), pp. 93-109.

Perrin, J. C. et al., 2009. Core-scale experimental study of relative permeability properties of CO2 and brine in reservoir rocks. *Energy Procedia,* Volume 1(1), pp. 3515-3522.

Pini, R. & Benson, S. M., 2013. Simultaneous determination of capillary pressure and relative permeability curves from core-flooding experiments with various fluid pairs. *Water Resources Research,* Volume 49(6), pp. 3516-3530.

Pini, R. & Benson, S. M., 2017. Capillary pressure heterogeneity and hysteresis for the supercritical CO2/water system in a sandstone. *Advances in Water Resources,* Volume 108, pp. 277-292.

Pini, R., Krevor, S. C. & Benson, S. M., 2012. Capillary pressure and heterogeneity for the CO2/water system in sandstone rocks at reservoir conditions. *Advances in Water Resources,* Volume 38, pp. 48-59.

Pini, R. et al., 2016. Quantifying solute spreading and mixing in reservoir rocks using 3-D PET imaging. *Journal of Fluid Mechanics,* Volume 796, pp. 558-587.

Pontes, C. C. et al., 2019. Petrophysical properties of deformation bands in high porous sandstones across fault zones in the Rio do Peixe Basin, Brazil. *International Journal of Rock Mechanics and Mining Sciences,* Volume 114, 1, pp. 153-163.

Qu, D. & Tveranger, J., 2016. Incorporation of deformation band fault damage zones in reservoir models. *AAPG Bulletin,* Volume 100(3), pp. 423-443.

Qu, D., Tveranger, J. & Fachri, M., 2017. Influence of deformation-band fault damage zone on reservoir performance. *Interpretation,* Volume 5(4), pp. SP41-SP56.

Rawling, G. C. & Goodwin, L. B., 2003. Cataclasis and particulate flow in faulted, poorly lithified sediments. *Journal of Structural Geology,* Volume 25(3), pp. 317-331.

Rawling, G. C., Goodwin, L. B. & Wilson, J. L., 2001. Internal architecture, permeability structure, and hydrologic significance of contrasting fault-zone types. *Geology,* Volume 29(1), pp. 43-46.

Richards, F. W., Vrolijk, P. J., Gordon, J. D. & Miller, B. R., 2010. Reservoir connectivity analysis of a complex combination trap: Terra Nova Field, Jeanne d'Arc Basin, Newfoundland, Canada. *Geological Society, London, Special Publications,* Volume 347(1), pp. 333-355.

Ritschl, L., Bergner, F., Fleischmann, C. & Kachelrieß, M., 2010. Water calibration for CT scanners with tube voltage modulation. *Physics in medicine and biology,* 55(14), p. 4107.

Rotevatn, A. & Fossen, H., 2011. Simulating the effect of subseismic fault tails and process zones in a siliciclastic reservoir analogue: Implications for aquifer support and trap definition. *Marine and Petroleum Geology,* Volume 28(9), pp. 1648-1662.

Rotevatn, A. et al., 2017. Do deformation bands matter for flow? Insights from permeability measurements and flow simulations in porous carbonate rocks. *Petroleum Geoscience,* Volume 23(1), pp. 104-119.

Ruprecht, C. et al., 2014. Hysteretic trapping and relative permeability of CO2 in sandstone at reservoir conditions. *International Journal of Greenhouse Gas Control,* Volume 27, pp. 15-27.

Saadatpoor, E., Bryant, S. L. & Sepehrnoori, K., 2010. New trapping mechanism in carbon sequestration. *Transport in porous media,* Volume 82(1), pp. 3-17.

Saillet, E. & Wibberley, C. A., 2010. Evolution of cataclastic faulting in high-porosity sandstone, Bassin du Sud-Est, Provence, France. *Journal of Structural Geology,* Volume 32(11), pp. 1590-1608.

Sarmadivaleh, M., Al-Yaseri, A. Z. & Iglauer, S., 2015. Influence of temperature and pressure on quartz–water–CO2 contact angle and CO2–water interfacial tension. *Journal of colloid and interface science,* Volume 441, pp. 59-64.

Scarfe, W. C. & Farman, A. G., 2008. What is cone-beam CT and how does it work?. *Dental Clinics of North America,* Volume 52(4), pp. 707-730.

Schueller, S., Braathen, A., Fossen, H. & Tverang, J., 2013. Spatial distribution of deformation bands in damage zones of extensional faults in porous sandstones: Statistical analysis of field data. *Journal of Structural Geology,* Volume 52, pp. 148-162.

Schultz, R. A. & Balasko, C. M., 2003. Growth of deformation bands into echelon and ladder geometries. *Geophysical Research Letters,* Volume 30(20).

Schultz, R. A., Okubo, C. H. & Fossen, H., 2010. Porosity and grain size controls on compaction band formation in Jurassic Navajo Sandstone. *Geophysical Research Letters,* Volume 37(22.

Schultz, R. A. & Siddharthan, R., 2005. A general framework for the occurrence and faulting of deformation bands in porous granular rocks. *Tectonophysics,* Volume 411(1-4), pp. 1-18.

Scott, E. D. et al., 2010. Sedimentological control of fluid flow in deep marine turbidite reservoirs: Pierce Field, UK Central North Sea. *Geological Society, London, Special Publications,* Volume 347(1), pp. 113-132.

Sheng, J., 2013. *Enhanced oil recovery field case studies.* s.l.:Gulf Professional Publishing.

Shi, J. Q., Xue, Z. & Durucan, S., 2011. Supercritical CO2 core flooding and imbibition in Tako sandstone—Influence of sub-core scale heterogeneity. *International Journal of Greenhouse Gas Control,* Volume 5(1), pp. 75-87.

Shipton, Z. K. & Cowie, P. A., 2001. Damage zone and slip-surface evolution over μm to km scales in high-porosity Navajo sandstone, Utah. *Journal of Structural Geology,* Volume 23(12), pp. 1825-1844.

Shipton, Z. K. & Cowie, P. A., 2003. A conceptual model for the origin of fault damage zone structures in high-porosity sandstone. *Journal of Structural Geology,* Volume 25, p. 333–345.

Shipton, Z. K. et al., 2002. Structural heterogeneity and permeability in faulted eolian sandstone: Implications for subsurface modeling of faults. *AAPG bulletin,* Volume 86(5), pp. 863-883.

Shipton, Z. K., Evans, J. P. & Thompson, L. B., 2005. The geometry and thickness of deformation band fault core, and its influence on sealing characteristics of deformation band fault zones. *American Association of Petroleum Geologists Memoir,* Volume 85, pp. 181-195.

Skurtveit, E., Torabi, A., Gabrielsen, R. H. & Zoback, M. D., 2013. Experimental investigation of deformation mechanisms during shear-enhanced compaction in poorly lithified sandstone and sand. *Journal of Geophysical Research: Solid Earth,* Volume 118(8), pp. 4083-4100.

Smith, P., 2008. Studies of United Kingdom Continental Shelf fields after a decade of production: How does production data affect the estimation of subsurface uncertainty?. *AAPG bulletin,* Volume 92(10), pp. 1403-1413.

Soliva, R., Ballas, G., Fossen, H. & Philit, S., 2016. Tectonic regime controls clustering of deformation bands in porous sandstone. *Geology,* Volume 44(6), pp. 423-426.

Soliva, R. et al., 2013. A model of strain localization in porous sandstone as a function of tectonic setting, burial and material properties; new insight from Provence (southern France). *Journal of Structural Geology,* Volume 49, pp. 50-63.

Sosio de Rosa, S. et al., 2018. Along-strike fault core thickness variations of a fault in poorly lithified sediments, Miri (Malaysia). *Journal of Structural Geology,* Volume 116, pp. 189-206.

Taylor, W. L. & Polland, D. D., 2000. Estimation of in situ permeability of deformation bands in porous sandstone, Valley of Fire, Nevada. *Water Resources Research,* Volume 36(9), pp. 2595-2606.

Tindall, S. E., 2006. Jointed deformation bands may not compartmentalize reservoirs. *AAPG bulletin,* Volume 90(2), pp. 177-192.

Torabi, A., 2014. Cataclastic bands in immature and poorly lithified sandstone, examples from Corsica, France. *Tectonophysics,* Volume 630, pp. 91-102.

Torabi, A. et al., 2019. Fault zone architecture and its scaling laws: where does the damage zone start and stop?. *Geological Society, London, Special Publication,* Volume 496, pp. SP496-20.

Torabi, A. & Fossen, H., 2009. Spatial variation of microstructure and petrophysical properties along deformation bands in reservoir sandstones. *Aapg Bulletin,* Volume 93(7), pp. 919-938.

Torabi, A., Fossen, H. & Braathen, A., 2013. Insight into petrophysical properties of deformed sandstone reservoirs. *Aapg Bulletin, 9,* Volume 97(4), pp. 619-637.

Townsend, D. W., 2004. Physical principles and technology of clinical PET imaging. *Annals-Academy of Medicine Singapore,* Volume 33(2), pp. 133-145.

Tueckmantel, C. et al., 2012. Two-phase fluid flow properties of cataclastic fault rocks: Implications for CO2 storage in saline aquifers. *Geology,* Volume 40(1), pp. 39-42.

UTCT, 2016. *ARTIFACTS AND PARTIAL-VOLUME EFFECTS.* [Online] Available at: https://www.ctlab.geo.utexas.edu/about-ct/artifacts-and-partial-volume-effects/
[Accessed 08 10 2019].

Van Geet, M., Swennen, R. & Wevers, M., 2000. Quantitative analysis of reservoir rocks by microfocus X-ray computerised tomography. *Sedimentary Geology,* 132(1), pp. 25-36.

Van Hulten, F. F., 2010. Geological factors effecting compartmentalization of Rotliegend gas fields in the Netherlands. *Geological Society, London, Special Publications,* Volume 347(1), pp. 301-315.

Vasco, D. W., Pride, S. R., Zahasky, C. & Benson, S. M., 2018. Calculating trajectories associated with solute transport in a heterogeneous medium. *Water Resources Research,* Volume 54(9), pp. 6890-6908.

Vinegar, J. H. & Wellington, S. L., 1987. Tomographic imaging of three-phase flow experiments. *Review of Scientific Instruments,* Volume 58(1), pp. 96-107.

Walderhaug, O., 1996. Kinetic modeling of quartz cementation and porosity loss in deeply buried sandstone reservoirs. *AAPG bulletin,* Volume 80(5), pp. 731-745.

Wang, G. et al., 2017. Impact of diagenesis on reservoir quality and heterogeneity of the Upper Triassic Chang 8 tight oil sandstones in the Zhenjing area, Ordos Basin, China. *Marine and Petroleum Geology,* Volume 83, pp. 84-96.

Wellington, S. L. & Vinegar, H. J., 1987. X-ray computerized tomography. *Journal of Petroleum Technology,* Volume 39(08), pp. 885-898.

Wilkins, S. J., Davies , R. K. & Naruk, S. J., 2019. Subsurface Observations of Deformation Bands and Their Impact on Hydrocarbon Production within the Holstein

Field, Gulf of Mexico, USA. *Geological Society, London,* Volume Special Publications, 496, pp. SP496-2018.

Williams, R. T., Goodwin, L. B. & Mozley, P. S., 2017. Diagenetic controls on the evolution of fault-zone architecture and permeability structure: Implications for episodicity of fault-zone fluid transport in extensional basins. *GSA Bulletin,* Volume 129(3-4), pp. 464-478.

Willis, B. J. & White, C. D., 2000. Quantitative outcrop data for flow simulation. *Journal of Sedimentary Research,* Volume 70(4), pp. 788-802.

Withjack, E. M., 1988. Computed tomography for rock-property determination and fluid-flow visualization. *SPE formation evaluation,* Volume 3(04), pp. 696-704.

Worden, R., 2004. *Quartz Cementation in Sandstones: Reappraising the Controls.* Austin, Texas, AAPG HEDBERG CONFERENCE.

Worden, R. H. & Morad, S., 2000. Quartz cementation in oil field sandstones: a review of the key controversies. *SPECIAL PUBLICATION-INTERNATIONAL ASSOCIATION OF SEDIMENTOLOGISTS,* Volume 29, pp. 1-20.

Yan, C. H., Whalen, R. T., Beaupre, G. S. & Yen, S., 2000. Reconstruction algorithm for polychromatic CT imaging: application to beam hardening correction. *IEEE Transactions on medical imaging,* Volume 19(1), pp. 1-11.

Zahasky, C. & Benson, S. M., 2018. Micro-positron emission tomography for measuring sub-core scale single and multiphase transport parameters in porous media. *Advances in Water Resources,* Volume 115, pp. 1-16.

Zahasky, C., Kurotori, T., Pini, R. & Benson, S. M., 2019. Positron emission tomography in water resources and subsurface energy resources engineering research. *Advances in Water Resources,* Volume 127, pp. 39-52.

Zeng, G. L., 2010. *Medical image reconstruction: a conceptual tutorial.* New York: Springer.

List of Captions for Figures

List of Captions for Tables

Appendices

Appendix 1: Beam hardening correction step by step procedure

This text is the step by step procedure of the plug-in. The first paragraph explains how to import data and fill the initial box. The following steps are automatic. This text is related to both versions of the beam hardening correction plug in. To check which one is suitable for your dataset, please check that the average grey value (calculated for each slice) doesn't increase from bottom to top and vice versa. If yes, use the code "BeamHardening_Correction_plugin_NOaverage_profile". The differences between the two are explained in the second paragraph of this manual.

Importing data and dialogue box

Once the operator has imported the stack of the slices into ImageJ, the code can be loaded trough the option Plugins – Macro – Edit. A dialogue box is shown as soon the code is running, requesting the top and bottom number slices on which the correction should be applied and if the scan considered is an internal scan. To crop out any material outside the sample, the dialogue box requests the width in pixels of the outer ring or the sum of the outer rings if they are present around the sample (if no outer ring is present put 0 as value). The outer ring option can be also used in case there are few pixels not representative of beam hardening effect. For example, in low resolution scan characterized by a sample inside an outer metal ring, some pixels between the two are just related to the low resolution and to the interaction between the sample and the ring. Besides, in some internal scan images, there could be some really bright pixel, not related to beam hardening effect that should be not taken in account for the correction. Once that the all the sections in the dialogue box are filled, the code automatically computes the following steps.

Finding the centre of the sample and calculating the average radial profile

To proceed at calculation of radial profile, the centre coordinates and the radius of the circle, in which the sample shape is inscribed, are requested. The following process is applied to each slice of the stack except in case of internal scan. In this case, there is

no chance that the circle of interest is shifted along the stack. Then the centre coordinates will be the same for all the slices. In a general way, to define the centre coordinates and the radius of the circle, each slice is duplicated and an automatic thresholding type Li (Li & Lee, 1993) is applied Using the "doWand" tool in ImageJ it is possible to automatically select the shape (enough contrast should be provided between the sample and the background) and having the x and y coordinates of the points of the selection.

According to the theorem by which "One and only circle passes through any three points", for each slice, different sets of three points along the selection are investigated. For each set of three points a circle is drawn and its x y centre coordinates and radius are calculated and stored respectively in three different arrays. The process continues until all the points of the selection have been taken in account. The mode of each array is calculated for having just one and correct value respectively for x coordinate, y coordinates and radius. This method has been used to being suitable also for near-cylindrical shapes. In fact, if in the set of three points there is one point lying on the flat portion, the circle drawn is shifted from the right centre. The presence of the flat portion is the main reason why other methods, such as centre of mass cannot be applied in case of near-cylindrical shapes: the flat portion, in fact, will affect the centre calculated, which will be slightly different from the actual centre of the original cylindrical shape. To avoid the same problem and considering that the flat portion is just a small part of the sample, in this workflow the mode of the coordinate's arrays is calculated for defining the right centre of the sample.

If one or more outer rings are present, the final radius will be the difference between the radius calculated by the mode and the value of the outer ring in pixel inserted at the beginning in the dialogue box. This works only in the case in which the outer ring and the sample are concentric components. If not, we advise to crop the image without considering outer rings. Once that the centre coordinates and radius values are obtained, they are set as input in the plug in *Radial Profile Angle Ext Extended* (Carl, 2006). The plug-in calculates the radial profile or beam hardening curves. Specifically, starting from the centre it creates concentric circles with regular step (usually 1 pixel) and for each circle the average intensity (grey) value is defined. We have then intensity

values as function of the distance from the centre. The process is repeated for all the slices of the stack. Considering that some pixels of the background are included in the radial profile calculation and they may affect the fitting of the beam hardening curve, the latter is cut at its maximum value.

Two version of the code are available: in the standard one, all the radial profiles calculated for each slice are averaged for creating a single average radial profile. This is done to have one single curve fitting and save time. The second version of the code is suitable in case the average value of the entire slices from bottom to top and vice versa are characterized by a systematic increase. In this case the average radial profile cannot be representative of the entire stack and then the curve fitting is operated for each radial profile curve.

Curve fitting

The average radial profile is fitted with both Exponential with offset and Inverse Rodbard equations. The curve is then split in two in correspondence of the cut-off point (COP). To have homogeneous results between the two fittings around the cut-off point an overlapping window is set. The size of the overlapping window is 1% of the size of the average radial profile, but it has a minimum size of 5 points. We fit the first part of the average radial profile with Exponential with offset equation and the last part with Inverse Rodbard equation. The curve fitting is operated in ImageJ with doFit built-in function. The difference in mean between the two fitting registered in the overlapping window is used as additive parameter for correction.

Correction

Once that the coefficients for both equations are obtained, the correction of all the pixels of the images is applied following these steps:

1) duplicate each image of the stack and correct the central part with the Exponential with offset coefficients;
2) correct the original images with Inverse Rodbard coefficients;
3) copy the central portion of the image of the step 1
4) past in the central part of the image of the step 2.

Appendix 2: Supplementary text, figures and tables of Chapter 4

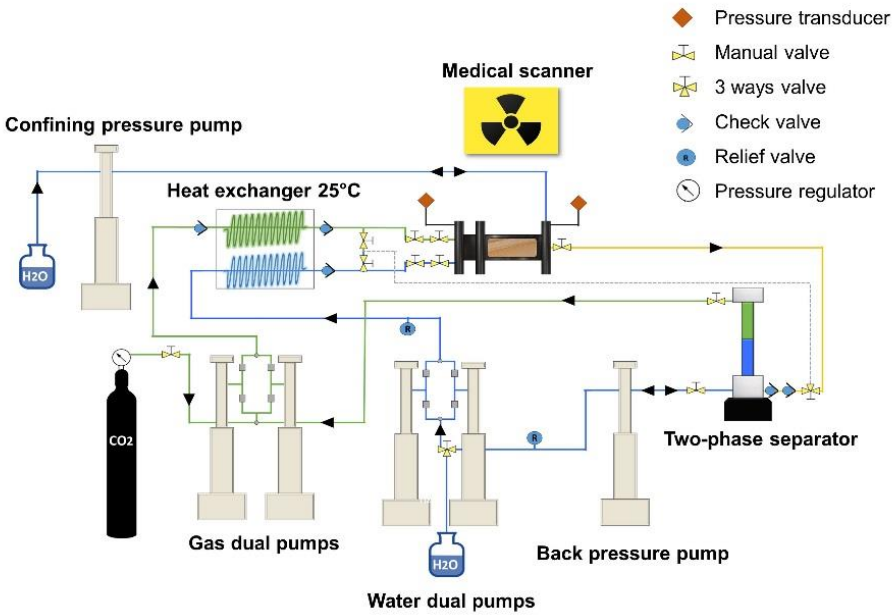

Figure A1. Schematic representation of core flooding experimental setup for injection of 100% CO2 (green) into water (blue) saturated sample at conditions of 25°C and 9MPa.

Dimension grid	35 x 5 x 78	35 x 5 x 78	35 x 5 x 78
Resolution	0.125 cm^3	0.125 cm^3	0.125 cm^3
Porosity HR	0.20	0.20	0.20
Porosity DB	0.12	0.12	0.12
Permeability HR	55 md	100 md	500 md
Permeability DB	10 md	0.5 md	0.0005 md
Rock compressibility	3E-9 (1/psi)	3E-9 (1/psi)	3E-9 (1/psi)
Temperature	20°C	20°C	20°C
Pressure	101.325 kPa	101.325 kPa	101.325 kPa

Flow rate	0.617 mL/min	0.617 mL/min	0.617 mL/min

Table A1. Input parameters for single phase models used for velocity maps in the section 4.3.3 of main manuscript

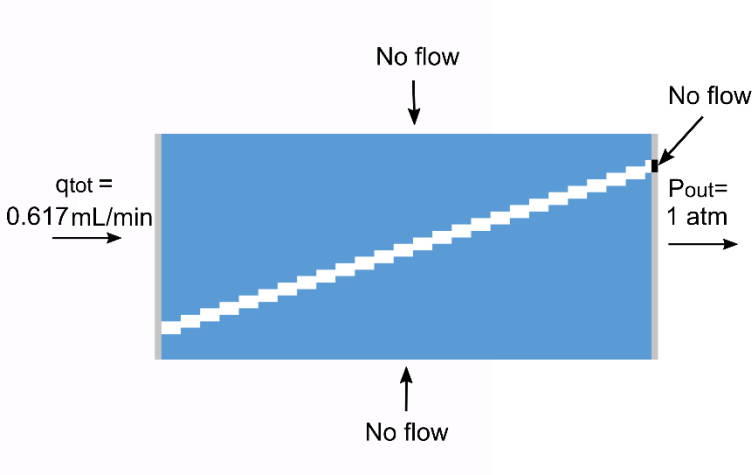

Figure A2. Boundary conditions of model used for simulating single phase water injection in a simple case with host rock (blue) and a single deformation band (white). Injection wells are placed in each grid of the inlet slice (grey) with a constant injection rate (0.617 mL/min, scaled from 4 mL/min of all core). Production wells are placed at the outlet slice (grey) where conditions of constant pressure (1 atm) are applied. No flow conditions characterize lateral faces and the portion of outlet slice attached to the band.

Text A1. With the multiphase experiments, we are able to measure capillary pressure at the inlet slice (Pini, et al., 2012). By plotting the inlet water saturation (Sw =1-SCO_2) against the differential pressure for each flow rate at steady state conditions, the capillary pressure curve is obtained (Fig. A3) parameterized by fitting experimental points with the Brooks-Corey capillary pressure model (Brooks & Corey, 1964)

$$Pc = Pc_{entry} \cdot Sw_{eff}{}^{1/\lambda}$$

$$Sw_{eff} = \left(\frac{Sw - Sw_{ir}}{1 - Sw_{ir}}\right)$$

Here Pc is the capillary pressure, Sw is water saturation, Sw_{ir} is the irreducible water saturation and λ is a parameter related to the distribution of pore size. For fitting experimental data, we used Pc_{entry}= 2.7kPa, Sw_{ir}=0.18 and λ=1.35.

The relative permeability of CO2 and water is then calculated with (Brooks & Corey, 1964).

$$kr_{CO2} = (1 - Sw_{eff})^2\left[1 - Sw_{eff}^{(2+\lambda)/\lambda}\right]$$

$$kr_w = Sw_{eff}^{(2+3\lambda)/\lambda}$$

Relative permeability curves are shown in Figure A4.

Capillary entry pressure for each voxel in the simulator is calculated using this scaling equation (Li, 2011).

$$Pc = Pc^r \frac{\sigma \cos\theta}{\sigma^r \cos\theta^r} \sqrt{\frac{k^r}{\varphi^r} \cdot \frac{\varphi}{k}}$$

Here r is the notation used for specifying the rock sample, σ is the interfacial tension, θ is the contact angle, k is the permeability and φ is the porosity. Capillary entry pressure for each grid cell is shown in Figure A5.

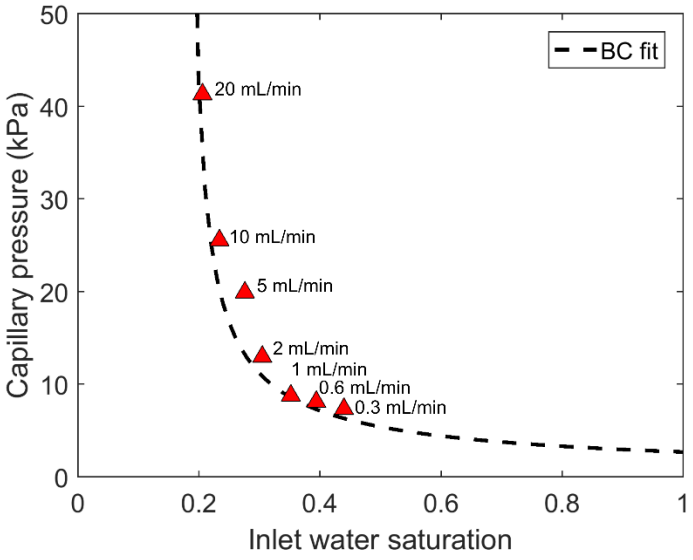

Figure A3. Capillary pressure measured with experimental data (red triangles) for each flow rate. Brooks-Corey model (dashed black line) used for fitting experimental data. Entry pressure = 2.7 kPa, irreducible water saturation = 0.18, λ = 1.35.

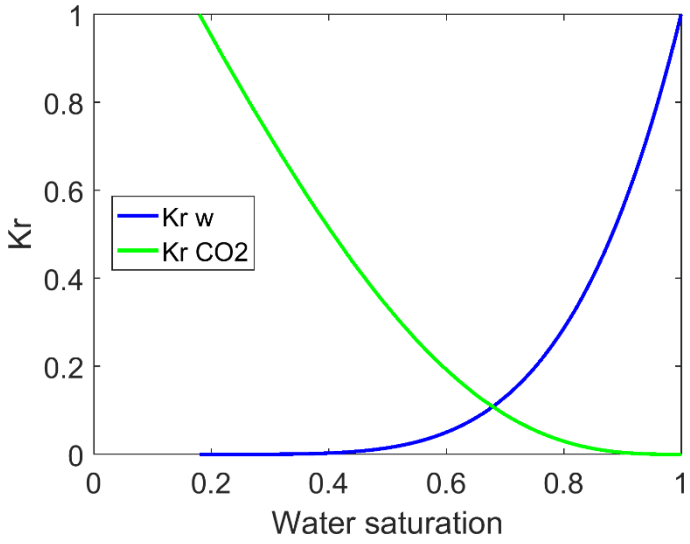

Figure A4. Relative permeability curves for CO2 (green) and water (blue) used in the GPRS simulator.

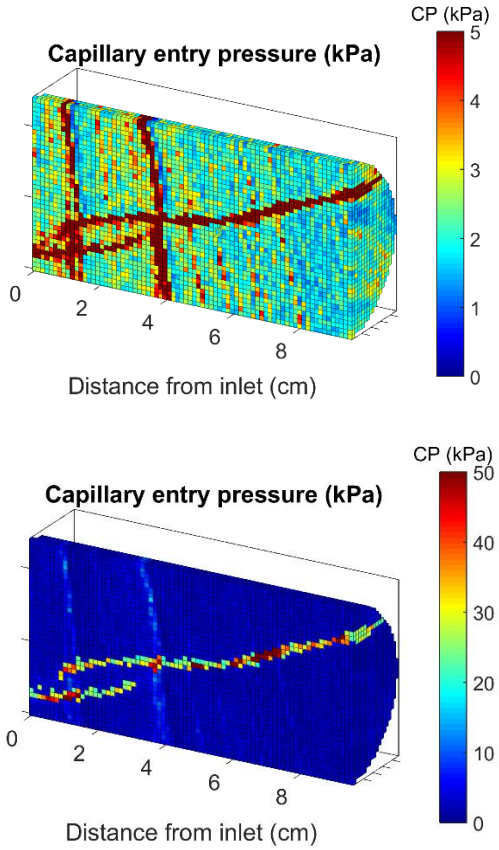

Figure A5. Capillary entry pressure used in the GPRS simulator. On the left scale bar from 0 to 5 kPa, on the right scalebar from 0 to 50kPa.

Dimension grid	35 x 5 x 78
Resolution	0.125 cm3
Porosity	Figure 4-2
Permeability	Figure 4-5
Relative permeability	Figure A4
Capillary pressure	Figure A5
Rock compressibility	4.35E-10 (1/kPa)
Temperature	25°C
Pressure	9 MPa

Table A2**.** Input parameters for multiphase simulations shown in the section 4.4 of main manuscript.

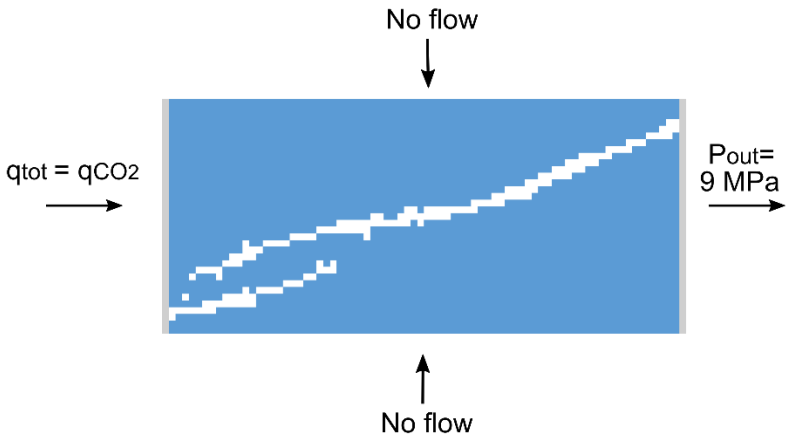

Figure A6. Boundary conditions of model (host rock in blue, deformation bands in white) used for simulating multiphase experiments. Injection wells are placed in each grid of the inlet slice (grey) with a constant injection rate. Production wells are placed at the outlet slice (grey) where conditions of constant pressure (9 MPa) are applied. No flow conditions characterize lateral faces.

Appendix 3: Supplementary figures of Chapter 5

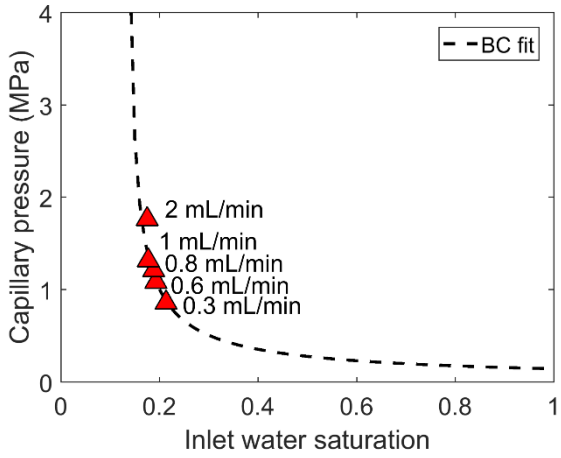

Figure A7. Capillary pressure measured with experimental data (red triangles) for each flow rate. Brooks-Corey model (dashed black line) used for fitting experimental data. Entry pressure = 0.14 MPa, irreducible water saturation = 0.13, $\lambda = 1.3$.

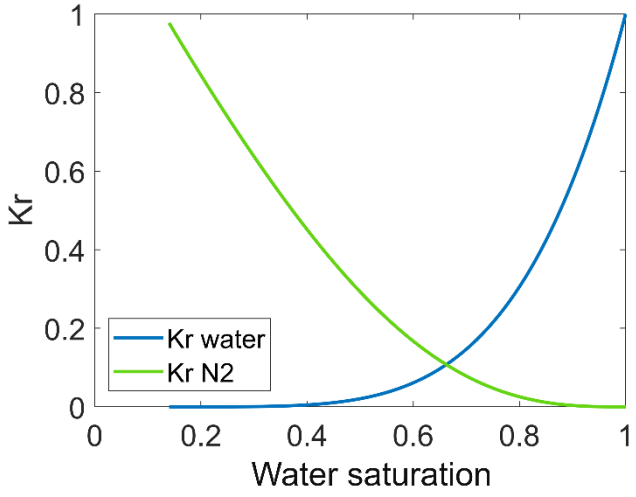

Figure A8. Relative permeability curves for N_2 (green) and water (blue) used in the GPRS simulator.

Appendix 4: Error analysis

Uncertainty analysis has been performed on porosity and saturation measurement at the voxel level. Pini et al (2012) propose a methodology based on error propagation and standard deviation, to characterize the uncertainty due to random error of CT numbers for a given pixel (σ_{pix}) during acquisition and reconstruction of scan images.

$$\sigma_{pix} = \sqrt{n}\,\frac{\sigma_{\Delta,n}}{\sqrt{2}}$$

,where $\sigma_{\Delta,n}$ is the standard deviation of the normal distribution given by the difference of the average of N (n=N/2) scans .

The porosity ($\sigma_{\emptyset}$) and saturation (σ_S) uncertainties are here defined

$$\sigma_{\emptyset} = \frac{\sqrt{2}\,\sigma_{pix}}{1000}$$

$$\sigma_S = \frac{\sqrt{2}\,\sigma_{pix}}{CT_{wat} - CT_{CO_2/N_2}}\sqrt{1 + \left(\frac{CT_{wat} - CT_{exp}}{CT_{wat} - CT_{CO_2/N_2}}\right)^2}$$

,where CT_{exp}, CT_{wat} and CT_{CO_2/N_2} are the slice-average CT values of the inlet slice during injection of non-wetting phase, water saturated and CO_2/N_2 saturated core, respectively.

The random error can be reduced by coarsening the images and by averaging multiple series of images acquired at the same conditions (dry, water saturated, equilibrated water saturated, CO_2/N_2 saturated, experimental conditions during injection of non-wetting phase).

For the porosity and CO_2 saturation measurements of the core presented in Chapter 4, at least three series have been acquired for each condition. The images have been coarsened by a factor of 4 in the x-y plane and by a factor of 2 in the z-plane. The uncertainties calculated for the porosity ($\sigma_{\emptyset}$) is 0.008. The uncertainty calculated for the CO_2 saturation (σ_S)based on images taken when CO_2 was injected at 0.3 mL/min, is 0.18.

For the porosity and N_2 saturation measurements of the core presented in Chapter 5, at least four series have been acquired for all experimental conditions. Exceptions are represented by the case of N_2 injection at 1 mL/min and 2 mL/min, where three and two series have been acquired, respectively. The images have been coarsened by a factor of 4 in the x-y plane and by a factor of 2 in the z-plane. The uncertainties calculated for the porosity ($\sigma_{\emptyset}$) is 0.028. The uncertainty calculated for the N_2 saturation (σ_S)based on images taken when N_2 was injected at 0.3 mL/min, is 0.075.

Other sources of error can be represented by variations of the pressure values and flow measurements recorded, which are functions of the accuracy of the devices used (pressure transducers, pumps).

Derived estimation of petrophysical and multiphase properties are subjected to some approximations. Absolute permeability, capillary pressure curve and relative permeability curves are estimated through empirical relationships. Experimentally measured capillary pressure for the inlet slice is estimated assuming that steady state conditions are reached and that there is no gradient in the water pressure. This condition may be easier to reach in homogeneous rock core than heterogeneous samples. The J-Leverett function, used for correlating the capillary pressure curves of different rocks or different portions of the same rock (host rock and deformation bands in the cases of this study), relies on the assumption that the rocks or rock features have the same pore shape and wettability, but different pore size. All above mentioned assumptions made for estimating petrophysical and multiphase model input parameters, affect the match between experimental and simulation results.

The following table represents the numerical modelling performance results for the simulations of Chapters 4 and 5. The relative error on mass balance is defined as the ratio between the absolute error in mass balance divide by the total mass initially in the system. The maximum relative mass balance error has been set for all the simulation to 0.01.

Simulation	Relative error Mass balance (%)	Total running time (s)
END SB 0.3 mL/min	0.000113823	2698
END SB 20 mL/min	0.000232781	160
NO END SB 0.3 mL/min	0.000200056	2635
NO END SB 20 mL/min	5.0981e-005	113
NO LAMINAE 0.3 mL/min	0.000727408	1018
END CB 0.3 mL/min	0.00400328	3434
END CB 2 mL/min	0.0044456	3147
END CB HOLES 0.3 mL/min	0.0105537	3129
END CB HOLES 2 mL/min	0.0106102	2863

Table A3. Performance results of some numerical modelling shown in the manuscript. END= numerical modelling with capillary end effect, NO END= numerical modelling without capillary end effect, NO LAMINAE= numerical modelling without capillary end effect and laminae. SB= single bands core sample, CB= cluster of bands core sample. HOLES= numerical modelling with discontinuities in bands.

Appendix 5. Pressure behaviour during simulations

This section analyses the pressure behaviour of non-wetting phase during some simulations shown in the main manuscript.

Figure A8 represents the delta pressure of the CO_2 during simulation of injection of the non-wetting phase (CO_2) into the model representing the central portion of the core of the Chapter 4, without accounting for the capillary end effect. The delta pressure is identified as the difference between the CO_2 pressure the outlet of the model. The outlet was set to a constant pressure of 9 MPa. The difference is equal to the capillary pressure when the water pressure has no gradient, i.e. when no water is flowing in to or out of the model. When the voxel CO_2 saturation approaches zero, the output delta CO_2 pressure corresponds to the capillary entry pressure assigned to the voxel. This is why in Figure A8 a high delta CO_2 pressure is observed along the bands even when, at low flow rates, they have almost zero CO_2 saturation (Figure 4-6). The delta CO_2 pressure increases as the flow rate increases. For all the flow rates, the delta CO_2 is higher before the two fine-grained, perpendicular to the core axis, laminae. The laminae favour the increase of CO_2 pressure in the portion of the model located upstream, and act like capillary barriers. Downstream of the laminae, the compartment above the deformation bands is characterized by a higher CO_2 pressure gradient, compared to the one below. Considering that there is no variation in porosity, absolute permeability, or capillary entry pressure between the two host-rock compartments, the difference in delta CO_2 pressure is attributed to a decreasing cross sectional area towards the outlet in the compartment above the bands, and an increasing cross sectional area towards the outlet in the compartment below the bands. A similar behaviour was observed in the single phase in situ tracer experiments (Figures 4-3, 4-4).

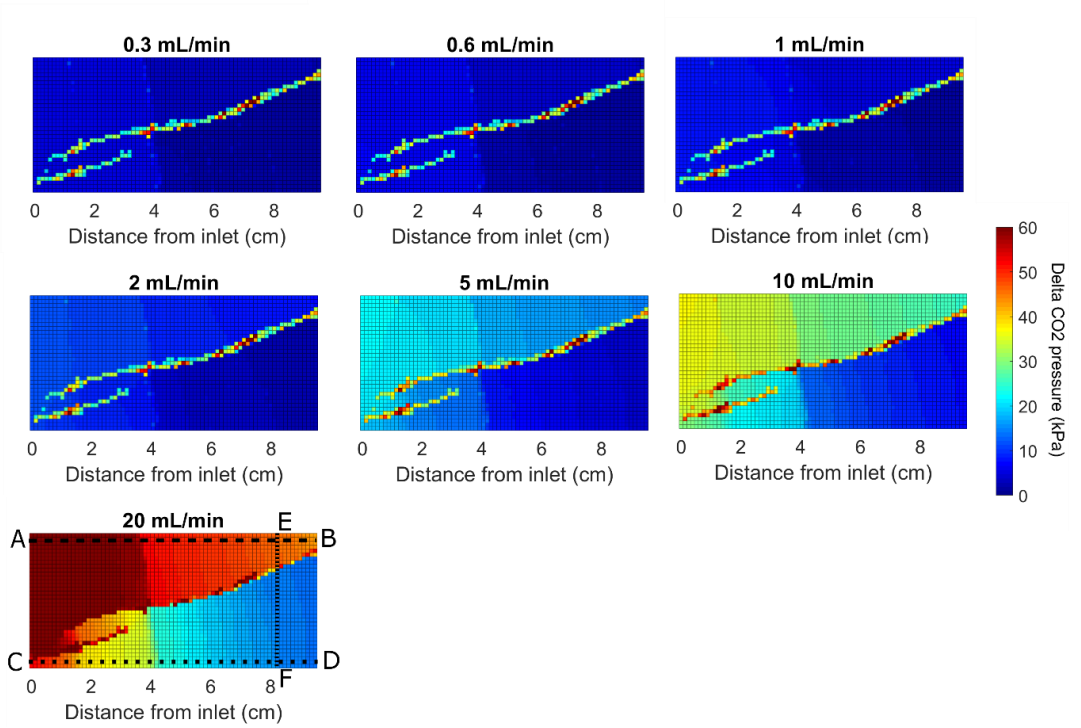

Figure A8. Delta CO_2 pressure values obtained by simulating injection at progressively higher flow rate of non-wetting phase into the model of the rock core of Chapter 4, without considering capillary end effect. AB-CD-EF profiles are marked for referencing the CO_2 delta pressure shown in Figure A9.

Figure A9 shows the CO_2 delta pressure values along two profiles located in the compartments above (AB) and below (CD) the deformation bands and one located across the bands (EF). The profiles are marked in Figure A8 (showing CO_2 delta pressure at 20 mL/min). In the compartment above the bands (Figure A9 top left), by injecting at higher flow rates, the delta CO_2 pressure increases. The two peaks in CO_2 delta pressure corresponds to voxels placed along the laminae. In these voxels, from 0.3 mL/min to 2 mL/min the values of delta CO_2 pressure are similar to the corresponding capillary entry pressure values (Figure A9 bottom left), meaning that the CO_2 saturation is zero or quasi zero. When the viscous forces overcome the capillary forces, the effect of the laminae on CO_2 pressure disappears (disappearing of the peaks); this happen at 5 mL/min for the voxel located along the first lamina, and at 2 mL/min for the voxel located along the second lamina.

Along the profile placed in the compartment below the deformation bands (Figure A9 top right), the capillary barrier effect of voxels located along the first and second laminae disappears at 0.3 mL/min and 10 mL/min, respectively.

As shown in Figure 9 (bottom left), towards the outlet the delta CO_2 pressure is higher in the compartment above the deformation bands than in the one below, for all the flow rates. Crossflow between the two compartments happens only when the CO_2 delta pressure in the compartment above the bands exceed the capillary entry pressure of the deformation band voxels placed along the profile EF; this is observed at 20 mL/min.

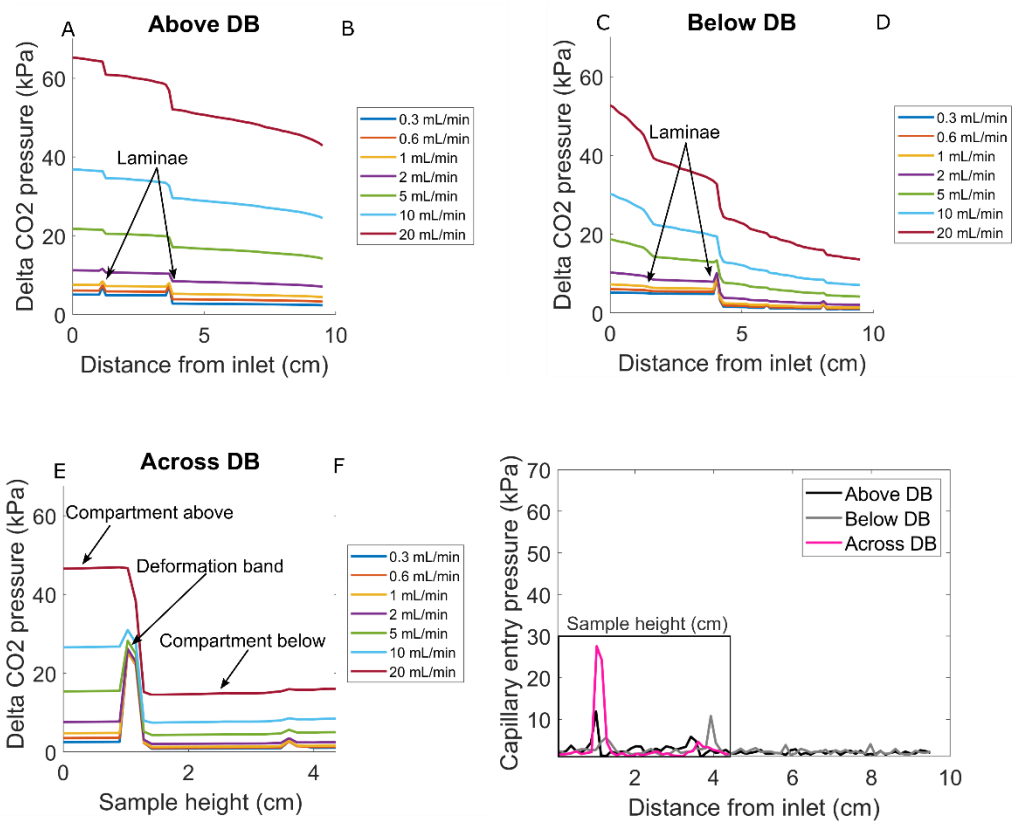

Figure A9. Delta CO_2 pressure values observed along three profiles AB-CD-EF, located respectively in the compartments above and below the bands, and across the bands. Specific locations are marked in Figure A8. Bottom left figure shows the model input capillary entry pressure values along the three profiles.

The observations made support our conclusions that in the core presented in Chapter 4, laminae influence multiphase transport properties and act like capillary barriers.

Deformation bands, for their properties and orientation, represents stronger capillary barrier than laminae.

Figure A10 shows the delta N_2 pressure during simulation of injection at 0.3 mL/min of non-wetting phase into the model presented in section 5.4.2, without considering discontinuities along the deformation bands. The model is a simplified version of the core shown in Chapter 5 and it accounts for the capillary end effect. The delta N_2 pressure is defined as the difference of the N_2 pressure and the outlet pressure (9 MPa). In this case, steady state conditions are approached only after 20 hours of injection. Hence, for all the other times the delta N_2 pressure is higher than capillary pressure, considering that there is still a gradient in the water pressure. The N_2 delta pressure immediately increases in host rock compartment 1 (for details on compartments number see Figure 5.6a of the manuscript); the capillary entry pressure of the deformation bands (220 kPa) is exceeded already after 15 min of injection and saturation with N_2 of compartments 4, 3 and 2 started at the same time, as shown in Figure 5.7. The N_2 pressure in compartment 1 starts decreasing (along with water pressure) after 1 hour of injection and steady state conditions are approached only when there is enough N_2 flowing out of the model and most of the water is displaced.

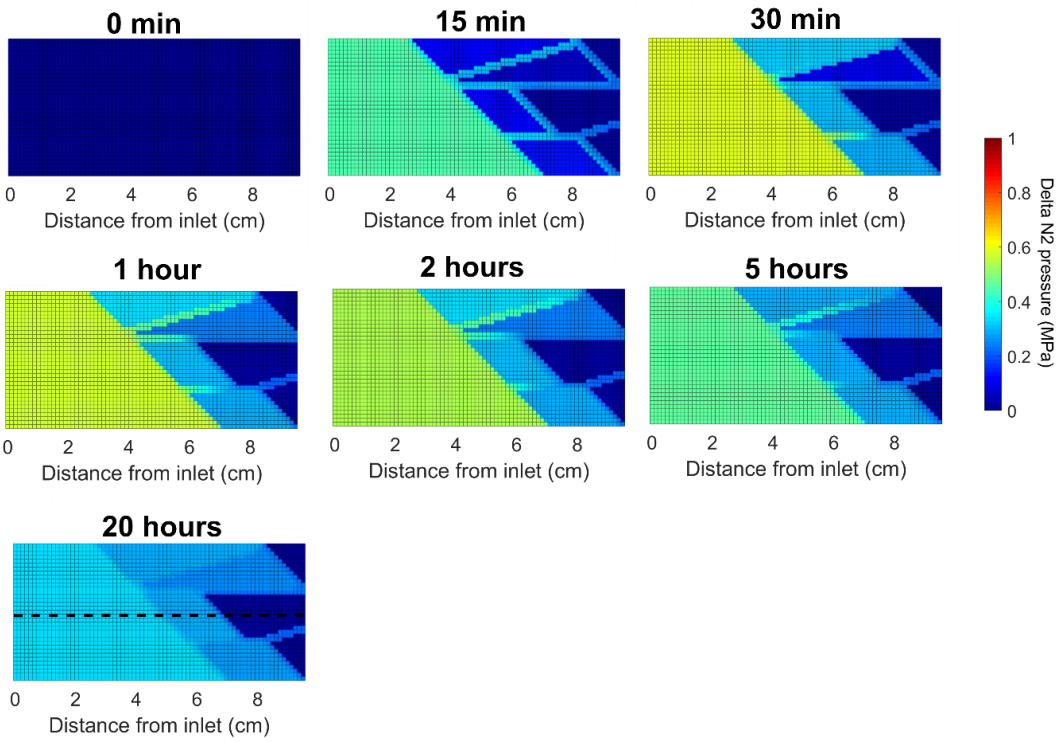

Figure A10. Delta N_2 pressure values obtained at different times by simulating injection at 0.3 mL/min of non-wetting phase into the model presented in section 5.4.2, considering capillary end effect and without discontinuities along the bands.

Figure A11 (right) shows the delta N_2 pressure values along the profile marked in Figure A10 (20 hours); compartments 1, 3 and 6 are placed along the profile. Since the bands traverses the entire sample, the only way that the non-wetting fluid has to reach the outlet, is to pass through the deformation bands. The build up in pressure in compartment 1 happens as soon the injection starts and no peak (similarly to Figure A9) related to the band placed between compartment 1 and 3 is observed. The capillary barrier effect of the band placed between compartments 3 and 6 disappears after 30 min from injection. On the left of the Figure A11 is shown in detail the delta N_2 pressure values in the last 2.5 cm of the profile: the delta N_2 pressure is not zero and the decreasing trend is due to the capillary end effect.

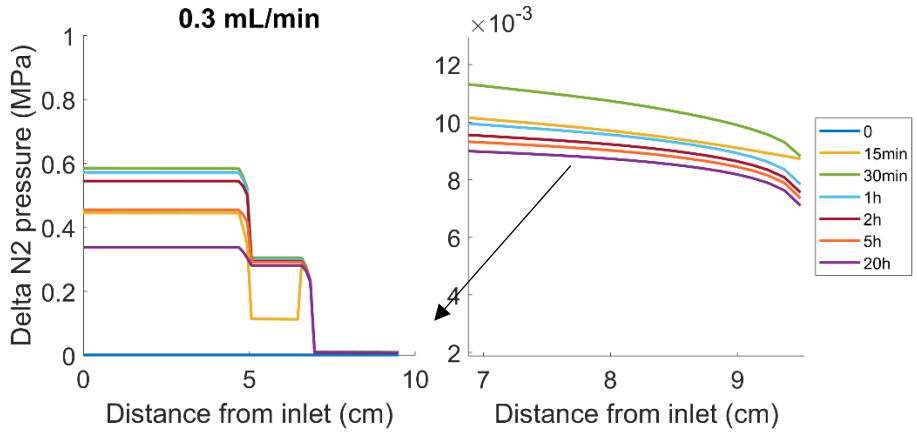

Figure A11. Delta N_2 pressure values observed along the profile marked in Figure A10 at several time from injection at 0.3 mL/min of N_2 in the model. On the left the zoom in of the last portion of the profile.

Figure A12 shows the delta N_2 pressure during simulation of injection at several flow rates of non-wetting phase into the model presented in section 5.4.2, considering discontinuities along the deformation bands and capillary end effect. The N_2 delta pressure increases as the flow rate increases and no build up of pressure is observed before the deformation bands, which are completely bypassed due to the presence of discontinuities. The delta N_2 pressure values along the bands and in host-rock compartments 3,7 and 8 corresponds to their capillary entry pressure values (220 kPa

for the bands and 7 kPa for host-rock), since the N_2 saturation is approaching zero value for all flow rates.

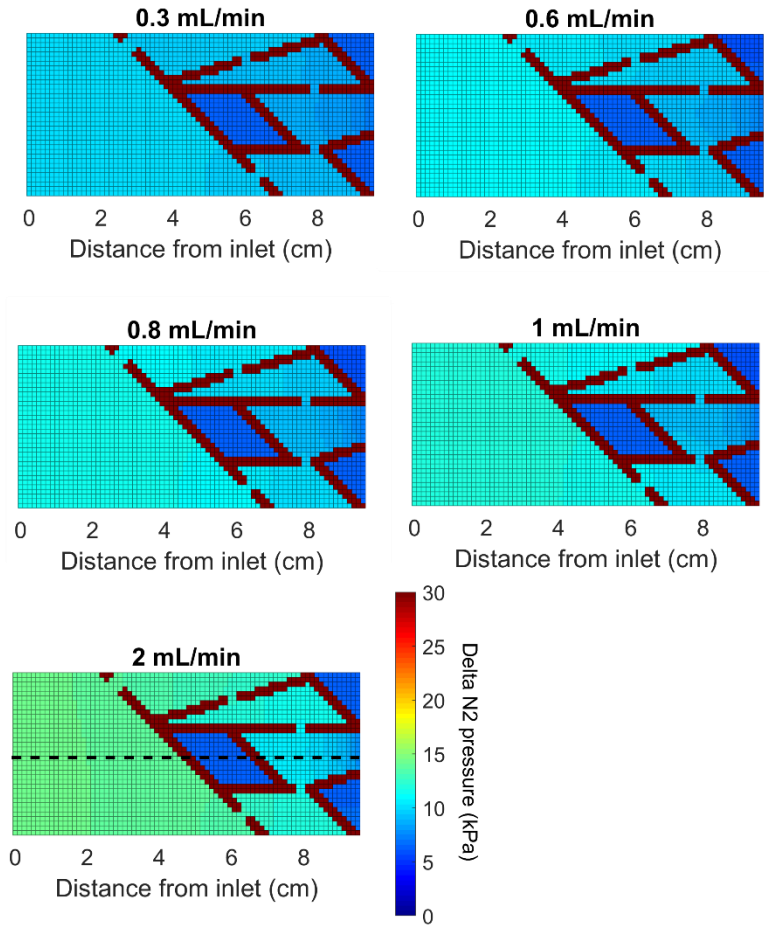

Figure A12. Delta N_2 pressure values obtained by simulating injection at progressively higher flow rate of non-wetting phase into the model presented in section 5.4.2, considering capillary end effect and discontinuities along the bands.

Figure A13 shows the delta N_2 pressure along the profile marked in Figure A12 (2 mL/min). The profile traverses compartment 1, 3 and 6. As shown in Figure 5.8, the compartments 3, enclosed in continuous bands, and deformation bands are not saturated with N_2, for all the flow rates. The capillary entry pressure of the deformation bands (220 kPa) and the compartment 3 (7 kPa) are never exceeded throughout the simulation.

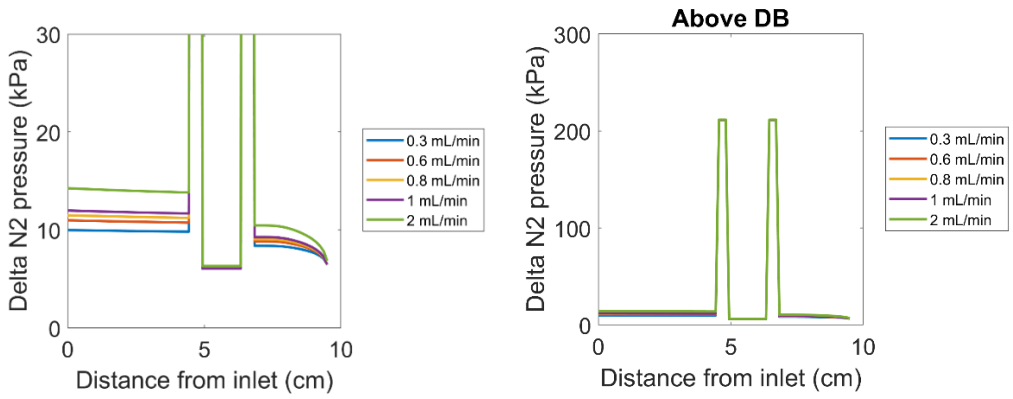

Figure A13. Delta N_2 pressure values observed along the profile marked in Figure A12 when N2 was injected in the model with discontinuities along the bands at several flow rates. On the left, y limit changed to 0-300 kPa for showing that the N_2 delta pressure along the bands never exceeds capillary entry pressure imposed (220 kPa).

The observation made support our conclusions that deformation bands can be responsible for build up in pressure during injection, especially if they traverse the entire system. Compartments enclosed in deformation bands characterized by discontinuities may never be saturated.